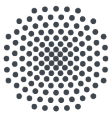

University of Stuttgart
Germany

Icing on Airborne Wind Energy

Master's Thesis

Author:	Ernsting Luz, Noel B. Sc.
Study Program:	M.Sc. Aerospace Engineering
Affiliation:	University of Stuttgart / NTNU Trondheim
Supervisors:	Dr.-Ing. Thorsten Lutz (IAG), Dr. Richard Hann (NTNU UAV Icing Lab)
Date of Submission:	6. November 2025

University of Stuttgart
Faculty of Aerospace Engineering and Geodesy
Institute of Aerodynamics and Gas Dynamics

Norwegian University of Science and Technology (NTNU)
Department of Engineering Cybernetics
UAV Icing Laboratory

Erklärung[1]

Hiermit versichere ich, dass ich diese Masterarbeit selbstständig mit Unterstützung des Betreuers / der Betreuer angefertigt und keine anderen als die angegebenen Quellen und Hilfsmittel verwendet habe.

Die Arbeit oder wesentliche Bestandteile davon sind weder an dieser noch an einer anderen Bildungseinrichtung bereits zur Erlangung eines Abschlusses eingereicht worden.

Ich erkläre weiterhin, bei der Erstellung der Arbeit die einschlägigen Bestimmungen zum Urheberschutz fremder Beiträge entsprechend den Regeln guter wissenschaftlicher Praxis[2] eingehalten zu haben. Soweit meine Arbeit fremde Beiträge (z.B. Bilder, Zeichnungen, Textpassagen etc.) enthält, habe ich diese Beiträge als solche gekennzeichnet (Zitat, Quellenangabe) und eventuell erforderlich gewordene Zustimmungen der Urheber zur Nutzung dieser Beiträge in meiner Arbeit eingeholt. Mir ist bekannt, dass ich im Falle einer schuldhaften Verletzung dieser Pflichten die daraus entstehenden Konsequenzen zu tragen habe.

RIO DE JANEIRO, 27.11.24, ...

Ort, Datum, Unterschrift

[1] In die Arbeit einzubinden – sowohl im Prüfexemplar als auch in der weiteren gedruckten und in der digitalen Fassung.

[2] Nachzulesen in den DFG-Empfehlungen zur „Sicherung guter wissenschaftlicher Praxis“ bzw. in der Satzung der Universität Stuttgart zur „Sicherung der Integrität wissenschaftlicher Praxis und zum Umgang mit Fehlverhalten in der Wissenschaft“.

Universität Stuttgart

Institut für Aerodynamik und Gasdynamik
Direktor: Prof. Dr.-Ing. Ewald Krämer

IAG

Masterarbeit
für Herrn Noel Ernsting Luz
(durchgeführt an der NTNU, Norwegen)

Icing on airborne wind energy

Airborne wind energy (AWE) harnesses wind power by using tethered flying devices, such as kites or drones. These operate at higher altitudes where winds are stronger and more consistent compared to traditional wind energy. Also, AWE systems require substantially less infrastructure and materials. One of the significant challenges for AWE systems is in-flight icing, where ice formation on the devices can disrupt aerodynamics, reduce efficiency, and increase the risk of equipment failure. The NTNU UAV Icing Lab (www.uavicinglab) is offering a master thesis on the topic of simulating icing on an AWE system.

The main objective of this project is to conduct icing simulations on an AWE drone (airframe wing, rotor, propeller) and tether using icing computational fluid dynamics (CFD) methods. Simulations will be conducted in 2D and 3D ANSYS FENSAP-ICE. Mesh generation will be done in Pointwise, based on generic geometries that will need to be developed. The simulations will estimate ice accretion and the icing effects on aerodynamic performance. The outcome of the thesis will be used to assess the sensitivity of AWE systems to icing and to highlight research gaps.

The thesis is to be conducted in English at the NTNU UAV Icing Lab in Trondheim.

Tasks:

- Literature study on aircraft icing, UAV icing, and AWE.
- Generate a generic and simplified 3D model of an AWE drone based on an existing platform.
- Conduct multi-shot icing CFD simulations on 2D cross-sections of the wing and rotors with FENSAP-ICE.
- Conduct single-shot icing CFD simulation in 3D of the tether and airframe with FENSAP-ICE.
- Validate the results experimental data as far as possible.
- Critical discussion of results.

Die Arbeit wird an der NTNU in Trondheim (Norwegen) durchgeführt.

Betreuer seitens NTNU:	Dr. Richard Hann
Betreuer seitens des IAGs:	Dr.-Ing. Thorsten Lutz
Ausgabetermin:	7.4.2025
Spätester Abgabetermin:	6.10.2025

Dr.-Ing. Thorsten Lutz

Abstract

Over the past twenty years, Airborne Wind Energy (AWE) has developed into an approach for harnessing high-altitude wind energy [1, 2]. Instead of being fixed on tall towers like conventional wind turbines, these systems operate at altitudes between 300 m to 500 m, where stronger and more continuous winds are found [3, 2]. The reduced structural mass of the airborne components offers a potential reduction in energy costs [1, 2], but operation in this altitude range also exposes the system to lower temperatures and variable humidity, which favours supercooled liquid water [3, 4]. In-flight icing changes the geometry, increases mass, degrades aerodynamics and has led to incidents in manned and unmanned aviation [4]. Since Airborne Wind Energy Systemss (AWESs) operate at similar altitudes to Unmanned Aerial Vehicles (UAVs), they are subject to comparable icing risks [3, 2, 4].

This work quantifies how in-flight icing affects the aerodynamic performance of a rigid-wing Airborne Wind Energy (AWE) system. Three icing simulations are carried out, representing glaze, mixed and rime ice at −2 °C, −4 °C and −10 °C, respectively. The results show that icing at −4 °C causes the strongest losses, reducing aerodynamic efficiency by up to 88 %, followed by −2 °C with about 49 % and −10 °C with about 33 %, all relative to a clean airfoil configuration. The cases are defined according to the FAA Appendix C icing standard, which leads to effective icing times of more than 50 min under sustained conditions due to the static nature of the considered AWE setup [5].

The developed orchestration framework combines aerodynamic performance metrics from two-dimensional simulations with limited three-dimensional effects (2.5-D simulations) to derive key performance indicators for a AWE system. It is compatible with airfoils in Selig coordinate format and structured in modular blocks for geometry preparation, meshing, simulation and analysis, enabling application to other profiles and operating points. The results indicate that active or hybrid de-icing concepts, particularly along the leading edge, are effective levers to avoid the most severe efficiency losses and provide quantitative input for the aerodynamic and structural design of kites for cold and humid environments.

Kurzfassung

In den vergangenen zwanzig Jahren hat sich die Airborne Wind Energy (AWE) zu einem Ansatz zur Nutzung hochliegender Windressourcen entwickelt [1, 2]. Anstatt wie herkömmliche Windturbinen auf hohen Türmen installiert zu sein, operieren diese Systeme in Höhen zwischen 300 m bis 500 m, in denen stärkere und gleichmäßigere Windgeschwindigkeiten auftreten [3, 2]. Durch die geringere strukturelle Masse der fliegenden Komponenten besteht das Potenzial, die Energiekosten zu senken [1, 2]. Der Betrieb in diesen atmosphärischen Schichten führt zugleich zu niedrigeren Temperaturen und variabler Feuchtigkeit und begünstigt damit das Auftreten unterkühlten flüssigen Wassers [3, 4]. Das entstehende Eis verändert die Geometrie, erhöht die Masse, beeinflusst das Strömungsfeld und stellt seit Langem ein zentrales Problem der Luftfahrt dar, das zu Unfällen in bemannter und unbemannter Luftfahrt geführt hat [4]. Da AWESs in ähnlichen Höhen wie UAVs betrieben werden, sind sie denselben Vereisungsrisiken ausgesetzt [3, 2, 4].

Diese Arbeit untersucht den Einfluss von Vereisung auf die Leistungsfähigkeit von AWESs. Hierzu werden drei repräsentative Vereisungssimulationen durchgeführt, die Klar-, Misch- und Reifeis bei Temperaturen von $-2\,^{\circ}\mathrm{C}$, $-4\,^{\circ}\mathrm{C}$ und $-10\,^{\circ}\mathrm{C}$ abbilden. Die Ergebnisse zeigen, dass Vereisung bei $-4\,^{\circ}\mathrm{C}$ die stärksten Verluste verursacht und die aerodynamische Effizienz um bis zu 88 % reduziert, gefolgt von $-2\,^{\circ}\mathrm{C}$ mit etwa 49 % und $-10\,^{\circ}\mathrm{C}$ mit etwa 33 %. Alle Werte beziehen sich auf den Vergleich mit einer sauberen Profilkonfiguration. Für die Falldefinition wird der FAA-Vereisungsstandard (Appendix C) verwendet, der in Verbindung mit der stationären Betrachtung eines AWE-Systems zu effektiven Vereisungszeiten von über 50 min führen kann [5].

Das entwickelte Framework kombiniert aerodynamische Kennwerte aus zweidimensionalen Simulationen mit begrenzten dreidimensionalen Effekten (2.5D-Simulationen), um die für ein AWE-System relevanten Leistungskennzahlen abzuleiten. Es ist mit Profilen im Selig-Koordinatenformat kompatibel und modular in Geometrieaufbereitung, Vernetzung, Simulation und Auswertung gegliedert, sodass weitere Profile und Betriebsfälle effizient untersucht werden können. Die Ergebnisse zeigen, dass die Integration aktiver oder hybrider Enteisungskonzepte, insbesondere entlang der Nasenkante, die kritischsten Effizienzverluste vermeiden kann und liefern quantitative Grundlagen für die aerodynamische und strukturelle Auslegung von Fluggeräten, die in kalten und feuchten Umgebungen betrieben werden sollen.

Contents

List of Figures

List of Tables

Acronyms

AOA Angle of Attack. 35

AWE Airborne Wind Energy. iii, 1–3, 5, 7–9, 24, 29

AWEC Airborne Wind Energy Consortium. 2

AWES Airborne Wind Energy Systems. iii, viii, 5, 52

BL Boundary Layer. 22, 23

CFD Computational Fluid Dynamics. 14

CFL Courant Friedrich Lev. 24

CM Continuous Maximum. 12

DNS Direct Numerical Simulation. 14

FG Flying Generation. 8, 9

GCI Grid Convergence Index. 28

GG Ground Generation. 5, 8, 9

HAWT Horizontal Axis Wind Turbine. 1, 2, 5, 7

IM Intermittent Maximum. 12

LE Leading Edge. ix, 21, 22, 31, 35–37, 43

LWC Liquid Water Content. 11, 12, 24, 29, 38

MVD Median Volumetric Diameter. 11, 24, 29

PDE Partial Differential Equations. 23

RANS Reynolds Averaged Navier Stokes. 24

SLD Superlarge Droplets. 10, 24

TE Trailing Edge. ix, 21, 22, 31, 35, 37, 43

UAV Unmanned Aerial Vehicle. iii, 3

1. Introduction

1.1. Global Energy Demand

Over the last decades, power demand and consumption have experienced rapid growth and continue to accelerate due to a variety of socio-economic drivers . The rising numbers of the global population, the industrial development and the electrification of our infrastructure, especially regarding the future development of artificial intelligence workloads require a solid and reliable power infrastructure. Meeting these requirements is part of greatest concerns of the 21st century, as it is expected for the global energy demand to rise from about 29000 to 30000 TW h in 2023 to 50000 TW h by 2050 (scenario for ambitious electrification) [6, 7].

Energy sources can roughly be categorized into conventional and renewable ones. Conventional sources exploit the energy density of a fuel, by burning the fuel to power turbines. These methods provide advantages like availability and maturity and have been thoroughly researched. Given the fact enough fuel is provided, said power plants can run at any time and provide a highly controllable and continuous stream of power. In contrast to that, their disadvantages are significant. Fossil fuels are unevenly distributed across the globe. Therefore they can be vulnerable against geopolitical tensions and disruptions in the supply chain. The most important point regarding future development is the environmental strain. Combustibles produce carbon-dioxide as a byproduct and nuclear waste is still an unresolved matter (although heavily researched) [6, 8, 9].

In contrast to that, renewable energies like solar, wind, hydroelectric, geothermal and biomass systems, offer a decentralized and sustainable approach. Renewable energies are geographically speaking widespread and can be deployed in a modular manner. Besides hydroenergy, wind and solar energy have emerged to be one of the most scalable technologies with the theoretical potential to power the world by themselves respectively. They come with their limitations as well. Solar energy is limited by efficiency and cloud coverage. And wind energy - particularly Horizontal Axis Wind Turbine (HAWT)'s - require unobstructed and steady winds to operate efficiently. That is why they are typically found in offshore or coastal regions [10, 7].

These limitations highlight the need for technological diversification within the renewable sector. Finding suitable technologies that satisfy according requirements like low cost, high scalability, and an according energy yield, stand in need for innovation. One approach is the field of AWE, which has promising results exploiting high-altitude winds by the use of crosswind power [11, 12].

1.2. Limitations of Conventional Renewable Systems

Despite the advantages using renewable systems like HAWTs and photovoltaic systems, they are limited by their effectiveness and scalability. We can distinguish between extrinsic factors and intrinsic factors. Extrinsic factors for HAWTs are of environmental nature for example discontinuous winds, rain, ice, and variable air density [11, 13].

While solar power is sensitive to changes in solar radiance, which moreover fluctuates based on time of day, it is generally limited by weather conditions and seasonal cycles. Regions with high cloud coverage, high humidity or more extreme latitudes like polar regions with long periods of darkness have a reduced

power output. Furthermore photovoltaic power plants need a large aerial coverage, which competes with the agricultural sector, urban development and natural habitats [7, 13].

Similar to that HAWTs have their environmental limitations as well. Best case operation requires steady winds with high mean velocities. These conditions are found in offshore sites, which come with their disadvantages as well. Materials have to be well selected due to the corrosive nature of salt water and power lines underlie the difficulty of having to be laid underwater. HAWT systems on land on the other hand can face their challenges being accepted by the population. Visual and acoustic impact of said systems lead to public resistance [14, 13].

Lastly, HAWTs are limited by their structural size. Higher altitude winds however are more consistent, and most importantly have higher velocities. Accessing higher altitude wind power brings several benefits. A significant reduction in system mass can be seen as well as a higher harvesting factor by using cross wind technology. Over the past few decades AWE Systems have emerged and have the potential use to attain a new energy sector if not being a successor to conventional HAWTs [13].

1.3. Emergence of Airborne Wind Energy

1980 Loyd proposed the use of crosswind kite power and laid the foundation with this patented technology. For about 20 years this technology did not experience much change until 2005. That year, a high altitude wind power conference was held in California and three years later, the Airborne Wind Energy Consortium (AWEC) has emerged. By that time less than 20 institutions performed active development on AWE. In 2013 there were already fifty institutions. From that time on, different AWE technologies have emerged. SkySails has successfully demonstrated their traction power technology onboard a cargo ship and Makani successfully developed a first commercial system showing the potential market for this kind of technology [12, 13].

Moreover there a three key aspects, why people are actively investing in AWE. Like solar, wind power is one of the few renewable energy resources with the potential to satisfy the global energy demand. Second, AWE devices are able to reach higher altitudes, exploiting said high, continuous winds. And last, those systems have a significant reduction in material investment, which shows promising results for large scale deployment at relatively low costs [2, 12].

A concrete example of such a system is the KM1 platform developed by Kitemill in Norway. KM1 is a rigid-wing, ground-generation AWE system with VTOL capability and a wingspan of about 7.4 m [15]. It is operated from the coastal test site at Lista, where Kitemill has demonstrated repeated autonomous flights and power-production cycles under maritime boundary-layer conditions . KM1 currently serves as the technology pathfinder for the larger 100 kW KM2 system that is being prepared for commercialisation [16]. Because KM1 flies in the 300–500 m altitude band above a cold and humid coastal site, it represents a realistic AWE configuration for analysing icing-related performance penalties [16, 4].

1.4. Motivation

Current research towards AWE systems shows several studies that estimate the size of the systems and their power output. These studies usually look at fixed-wing systems with ground-based generation and place them mostly between 0.1 and 2 MW, with many examples near 0.5 MW and annual capacity factors of about 0.35 to 0.55 [17, 18]. For comparison, recent assessments report capacity factors of about 0.17–0.22 for utility-scale solar PV, 0.25–0.40 for onshore wind and 0.45–0.60 for offshore wind [6, 19]. AWE therefore falls between good onshore sites and the lower offshore range while using a lighter airborne structure. In almost all cases the calculations are done with clean airfoil data [17].

Within the scope of this thesis it is investigated which kind of performance penalties derive from icing conditions. Icing research on UAVs itself is a fairly new research field; it has long been recognized that ice accretion leads to aerodynamic degradation and, in manned aviation, has contributed to accidents, which makes it a relevant hazard for small and medium unmanned aircraft as well [4, 20].

Since current AWE demonstrators operate typically below about 500 m above ground level, they operate in the same conditions as many UAVs and are thus exposed to similar combinations of temperature and humidity. At the same time, existing AWE simulators and power-production tools usually neglect icing, so there is no ready-to-use source of iced polars for AWE-relevant airfoils in the literature [13, 20].

This thesis therefore provides a numerical framework that generates iced aerodynamic polars for representative conditions for direct use in scalability and dimensioning frameworks. In doing so, it complements current AWE sizing and scalability studies, which assume clean aerodynamics, by supplying the missing performance degradation for airfoils.

2. Background

2.1. Airborne Wind Energy

AWE replaces the tower-based architecture of HAWTs with a tethered aircraft and a ground station. At 300 m to 600 m the winds are typically stronger and more consistent than at 100 m to 200 m. Replacing the tower by a lightweight tether also reduces material demand and reductions on the order of about 80% are reported [13, 2]. Figure 2.1 compares both concepts. The left side sketches the vertical wind profile. The middle part labels the HAWT components (rotor, hub, generator, tower). The right side shows a Ground Generation (GG) AWES with a tethered rigid-wing aircraft and a ground station.

This thesis investigates rigid-wing, systems. The KM1 platform serves as a representative example for investigation of aerodynamic degradation under icing. A GG cycle alternates between power-producing reel-out (crosswind flight) and low-power reel-in. The total power therefore depends on the reeling factor f, the overall efficiency η, and the duty cycle which will be introduced in section 2.1.1. To evaluate degradation, two metrics are used. The Loyd factor $\Lambda = C_L^3/C_D^2$ summarizes the aerodynamic power potential. The harvesting factor ζ links this to system operation and depends on f and η. Ice accretion shifts C_L, C_D and C_m in an disadvantageous way. Therefore Λ decreases in otherwise identical settings. The resulting losses are shown in chapter 4 and discussed in chapter 5. The relevant key metrics are introduced next in section 2.1.1.

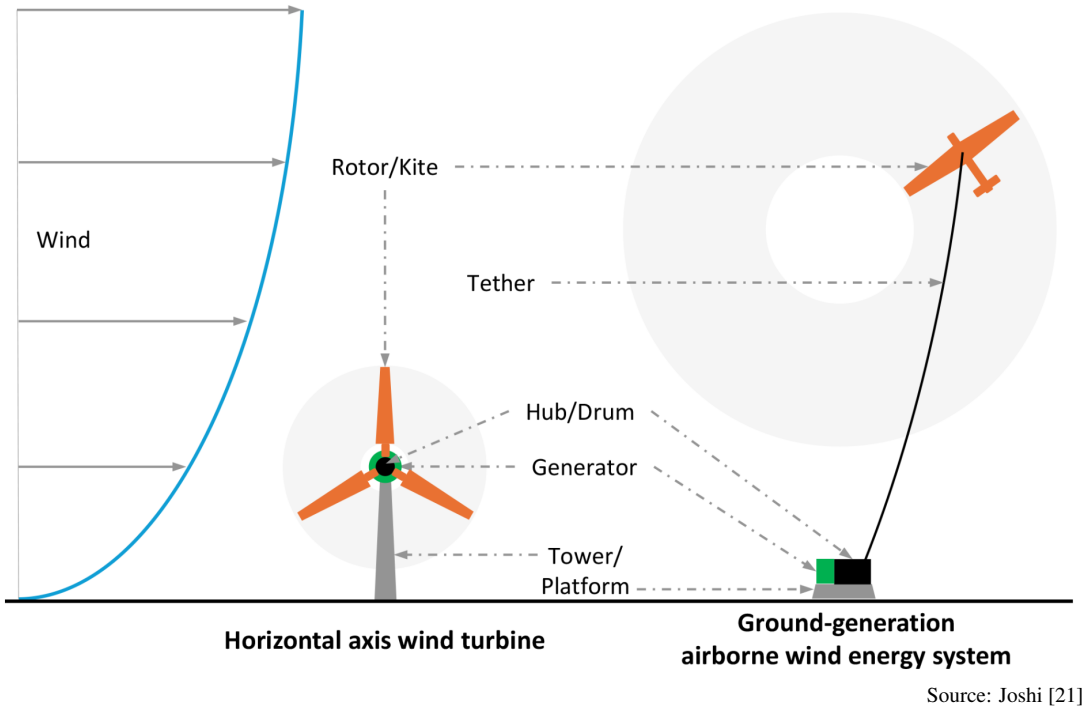

Source: Joshi [21]

Figure 2.1.: Schematic comparison of HAWT (left) and ground-generation AWE (right)

For rigid-wing GG systems, crosswind operation is the main source of power. In this regime the wing flies orthogonal through the wind field and amplifies the apparent airspeed. Loyd showed that an ideal

crosswind turbine extracts power that scales with the cube of the apparent wind speed and with the ratio of lift and drag coefficients [12]. In this thesis the aerodynamic contribution is condensed into the Loyd factor $\Lambda = C_L^3/C_D^2$, which measures the ideal power potential of a given polar, and a harvesting factor ζ that collects system-level reductions such as tether drag, reeling losses and conversion efficiency. Ice accretion modifies C_L, C_D and the stall behavior and therefore changes Λ at fixed operating conditions.

2.1.1. Crosswind Kite Power

This subsection introduces crosswind mechanics and the metrics used for targeted investigation of icing. The variables to describe the core mechanism of crosswind flight are the wind vector $\vec{v}_w$ and the body-fixed velocity $\vec{v}_k$ of the kite. The apparent wind v_a at the wing is the relative flow between wind velocity $\vec{v}_w$ and wing velocity $\vec{v}_k$:

$$\vec{v}_a = \vec{v}_w - \vec{v}_k \qquad v_a = \|\vec{v}_a\| \tag{2.1}$$

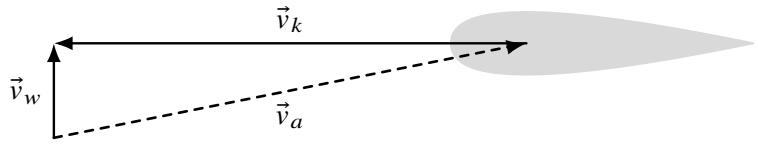

Source: Adapted from [2, p. 16]

Figure 2.2.: Simplified representation of apparent airspeed amplification (sideview crosswind flightpath)

In crosswind operation, the kite moves orthogonal through the wind field and converts lift into mechanical work. The apparent airspeed v_a increases with the crosswind velocity v_k and can reach 5–10 times the wind speed. Because dynamic pressure scales with v_a^2, the available aerodynamic power scales with v_a^3. This mechanism enables AWESs to exceed the power density of conventional HAWTs [12, 2].

Lift and drag (equation (2.2)) are calculated from the dynamic pressure of the apparent wind $q = \frac{1}{2}\rho v_a^2$ where ρ is air density, and A the wing platform area [2]. With lift and drag coefficients C_L and C_D, the forces are

$$F_L = q\,A\,C_L \qquad F_D = q\,A\,C_D \tag{2.2}$$

and the glide ratio is defined as:

$$G = \frac{F_L}{F_D} = \frac{C_L}{C_D} \tag{2.3}$$

For AWES performance, the relevant part is power over the pumping cycle. This requires a link from forces at the wing to mechanical output at the drum and therefore to electrical energy. The transition proceeds in two steps. First, the wind resource sets the available scale through its cube dependence on the wind speed (equation (2.4)). Second, crosswind operation connects the aerodynamic coefficients to mechanical power via the ideal scaling (equation (2.5)), so that lift and drag are accounted for through their ratio, rather than as separate forces [2, 12].

To interpret results and to isolate icing effects, the aerodynamic potential is separated from power evaluation. The aerodynamic part is condensed into a single metric that follows directly from the polars and appears in the ideal scaling. This Loyd factor Λ is introduced below in equation (2.9). The power evaluation part collects further reductions such as cosine loss, tether drag, conversion efficiency, reeling dynamics and duty cycle into a dimensionless harvesting factor ζ. With Λ representing what the wing can deliver and ζ

representing how the system harvests it, the following equations establish the necessary interface used throughout the icing analysis [2, 12].

Starting with the wind power, it is shown in equation (2.4), that v_w enters the power in a cubic manner and therefore shows significant sensitivity towards wind speed.

$$P_{\text{wind}} = \tfrac{1}{2}\rho A_{\text{ref}} v_w^3 \tag{2.4}$$

therefore small changes in v_w have a strong effect on power [2]. Under Loyd's crosswind assumptions of continuous operation, optimal reel-out and no tether effects, the mechanical power can be found as

$$P_{\text{Loyd}} = \frac{2}{27}\rho A v_w^3 C_L \left(\frac{C_L}{C_D}\right)^2 \tag{2.5}$$

This adds the gliding ratio G, more specifically the cubic relation of C_L as an additional key sensitivity. The fraction $\frac{2}{27}$ originates from the analytical optimization of the reeling velocity v_r by Loyd. Within this thesis the optimum reeling factor f_{opt} is treated as $f = \frac{1}{3}$ [12]. The elevation angle γ between tether and wind velocity v_w reduces power extraction by a factor known as cosine loss: $\cos(\gamma)$. If tether drag is considered, it lowers the effective glide ratio. Splitting wing and tether contributions [2]:

$$G_e = \frac{C_L}{C_{D,\text{wing}} + C_{D,\text{tether}}} \tag{2.6}$$

A first estimate for tether drag treats the tether as a slender cylinder with effective diameter d_{eff} and length ℓ_{tether}:

$$D_{\text{tether}} \approx \tfrac{1}{2}\rho C_{D,\text{tether}} d_{\text{eff}}\, \ell_{\text{tether}}\, v_w^2 \tag{2.7}$$

This leads to the assumption, that thicker or longer tethers reduce G_e. Combining the crosswind kite power with cosine loss and the effective glide ratio yields the total idealized power output:

$$P_{\text{AWE}} \approx \frac{2}{27}\rho A v_w^3 C_L G_e^2 \cos\gamma \tag{2.8}$$

This connects C_L, C_D and elevation γ. Within this scope γ is considered to be zero, therefore no cosine loss will be accounted for as it only scales the output in an idealized scenario (γ=const.). Dividing and normalizing the systems power by the wind power yields the harvesting factor ζ, a scaled form of the loyd factor Λ . It is a direct indicator for the systems power output and will be evaluated as key result:

$$\zeta = \frac{4}{27}\Lambda \qquad\qquad \Lambda = \frac{C_L^3}{C_D^2} \tag{2.9}$$

2.1.2. System Components

This section gives an overview of the four subsystems and how they react to the metrics used in this thesis. The wing sets the aerodynamic potential through its polars and the derived Loyd factor $\Lambda = C_L^3/C_D^2$. The tether and flight geometry reduce usable glide via G_e and $\cos\gamma$. The ground station and the navigation–and–control unit determine how much of that potential is harvested over a cycle and are collected in the factor ζ. The reference system is a rigid-wing, ground-generation, crosswind setup (KM1). Unless noted otherwise, the reeling factor is fixed at $f_{\text{opt}} = 1/3$, the cosine loss is neglected as mentioned before ($\gamma = 0$), and η is held constant. Under these assumptions, relative power differences between cases trace back to changes in Λ [2].

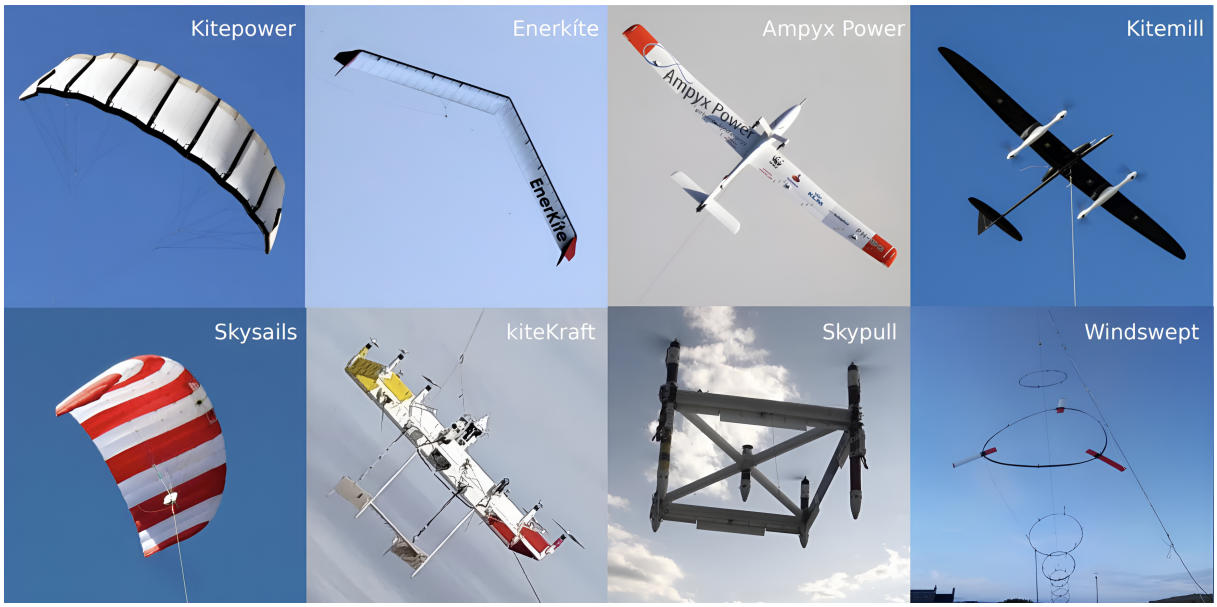

Source: Adapted from `https://airbornewindeurope.org/archivos/7312`

Figure 2.3.: Comparison photo of eight representative kites and their manufacturing companies

Kite

The kite translates the apparent wind velocity into lift and transmits this force onto the tether. The glide ratio G and the Loyd factor Λ were introduced in section 2.1.1 and follow directly from the aerodynamic polars. Rigid wings usually reach higher G and a predictable C_m polar, but also come with higher structural mass [2, 22]. The wing should deliver high C_L at operating α and keep C_D low across the crosswind range [2]. Stall position sets the usable α range [23], and the slope of the C_m polar supports a stable α during reel–rate changes [24, 23]. Aspect ratio as well as planform set induced drag and are noted here for completeness [23]. Crosswind flight is characterized by $v_a \gg v_w$, so the wing should maintain a high C_L/C_D while staying within structural and control limits. In this thesis this appears in the simulated polars and is summarized by Λ. Icing is treated later in section 2.2 the focus is on the clean aerodynamic potential expressed by Λ under fixed operating assumptions. For evaluation an idealized rigid wing section is assumed with a rectangular planform.

Tether

The tether transfers the aerodynamic force from the wing to the ground station. Its diameter, length and surface condition set its aerodynamic drag and added mass; for AWE tethers the drag is commonly modeled as that of a slender circular cylinder, so larger diameter or longer length increases the load and lowers usable crosswind speed [2]. Weight and sag change the elevation angle and the catenary, which limits the reachable flight window and reduces power. Research and estimations for these effects exist (i.e. [25]). Stiffness and damping govern tether dynamics and controllability, affecting the systems response and the handling of gusts [26]. In this thesis the tether geometry and surface condition are kept constant and no tether ice is modeled. Relative differences between cases therefore reflect changes in the section polars of the model.

Ground station

The ground station anchors the system and converts mechanical work at the drum into electrical power during pumping operation. It consists of drum, winch or drive, gearbox, generator, power electronics, and safety devices such as brakes or clutches. In operation it must withstand peak line tensions, regulate the reeling rate, and manage the transition throughout the reeling cycles. Losses arise in the mechanical drive and in the electrical conversion chain. In this thesis these settings are held constant across all cases, so the ground station acts as a fixed interface that maps aerodynamic input to grid output [2, 27].

Navigation and control

The navigation-and-control unit stabilizes and regulates the crosswind flight path. It controls the actuators, and manages the reeling rate and path tracking in pumping operation. Some of the existing architectures regulate line tension and airspeed while guiding the wing in looped trajectories They handle the reeling cycle with dedicated controllers [2]. For rigid-wing AWE, recent work investigates loop-tracking, winch coordination, constraint handling under realistic limits [28]. For degraded aerodynamics, reduced C_L/C_D and shifts in $C_m(\alpha)$ are expected and shrink operating window. In this thesis, controls and limits are held constant across cases, thus observed differences like other components rather then the kite, originate from the wing polars summarized by Λ.

2.1.3. Operating Modes

Airborne wind systems are realized as GG or Flying Generation (FG). This section relates the results of this thesis regarding that context and states which mode the analysis assumes. This section is included to orient the reader. As mentioned before, the assumed operation is rigid-wing crosswind with constant settings. Mode-specific optimizations are out of scope. The change in Λ leads to a proportional change in harvested output for the fixed GG operating point.

Ground-Generation (GG)

In GG the wing flies crosswind while the tether is reeled out and in at the ground station. During reel-out the line tension translates the tether force with the positional change to power at the drum. During reel-in the system is depowered to reduce energy use. The ground station controls the winch, performs power conversion and manages the transitions between the two phases. GG is the standard choice for rigid-wing platforms such as the KM1. Within the fixed settings defined in section 2.1.1 changes in the wing polars and in the Loyd factor Λ translate into proportional changes in harvested output [2, 29].

Fly-Generation (FG)

In FG the generators are onboard the wing and electrical power is sent through the tether. Output is continuous rather than cyclic. In addition FG demands strict limits on airborne mass, cooling and reliability. The aerodynamic trends in this thesis still apply, since the conversion chain and constraints differ. Because the reference system is rigid-wing GG and external settings are held fixed, FG is not analyzed further [2].

2.1.4. Classification of AWE Systems

As introduced in section 2.1.2 and shown in figure 2.4, AWES can be grouped by where electricity is produced and by how the wing flies. GG places the drum and generator on the ground and operates the

wing in pumping cycles. FG places generators on the wing and sends electrical power down the tether. Crosswind flight uses lateral motion to increase apparent airspeed. Tether-aligned flight produces traction without crosswind loops. This thesis uses a rigid-wing, GG, crosswind configuration as the reference because the conversion chain is on the ground and it matches the KM1 demonstrator introduced in the Introduction. Other variants in figure 2.4 are shown for orientation only and are not analyzed further since icing results are evaluated through airfoil polars and the Loyd factor Λ for the GG crosswind case.

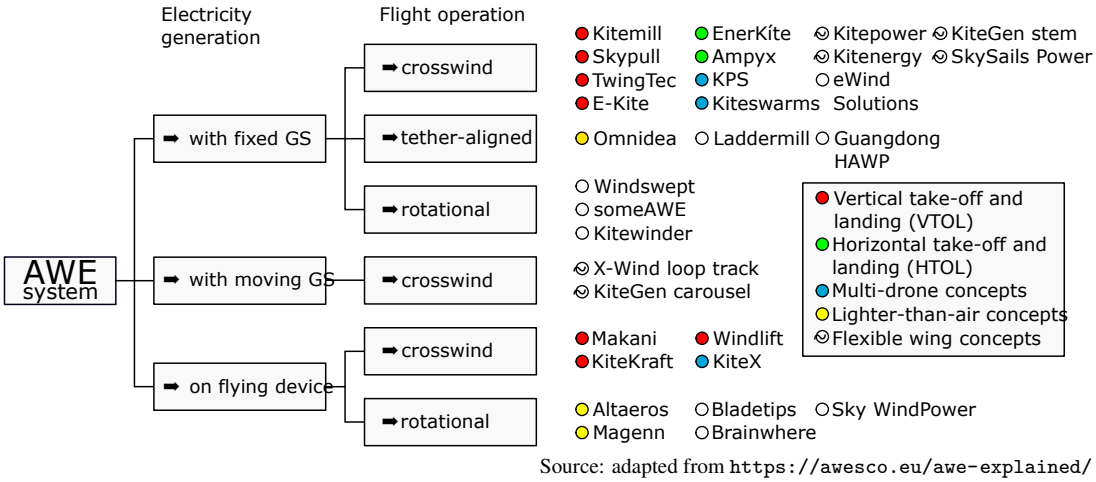

Source: adapted from `https://awesco.eu/awe-explained/`

Figure 2.4.: Classification of AWE systems by electricity generation and flight operation

2.2. In-flight Icing

In-flight icing refers to the accretion of ice on aircraft surfaces when flying through supercooled liquid water (SLW) or Superlarge Droplets (SLD). These conditions can occur globally and at any time of the year. While not necessarily leading to aircraft loss, ice accumulation strongly degrades aerodynamic performance and poses a major hazard to flight safety [30, 4].

2.2.1. Classification of Ice Types

Glaze, mixed, and rime form under different thermodynamic conditions and show distinct LE morphologies. At temperatures near 0 °C, a liquid film forms and refreezes. This produces clear, smooth ice that can grow into asymmetric horns (glaze). At intermediate conditions, partial freezing and a coexisting film lead to rough, irregular ice with elements of both processes (mixed). At lower temperatures, droplets freeze on impact without a film. enclosed air pockets make the deposit opaque and comparatively conformal to the nose (rime). These observations and terms follow standard usage in the icing literature (See [4]). A short overview of icing morphology and their typical operational implications is given:

- **Glaze ice** Seen left in figure 2.5 and found at a representative temperature of $T = -2\,°\text{C}$. Gradual freezing with runback water. Transparent appearance, horn formation at the LE. Strong aerodynamic penalties and high sensitivity to small changes in conditions [4].
- **Mixed ice** Seen in the center in figure 2.5 and found at a representative temperature of $T = -4\,°\text{C}$. Combination of rapid freezing like rime ice and film effects such as in glaze. Rough, irregular ice with possible horn formations. Significant aerodynamic penalties with high variability [4].
- **Rime ice** Seen right in figure 2.5 and found at a representative temperature of $T = -10\,°\text{C}$. Immediate freezing on impact. Opaque, porous surface with small feather-like features. Comparatively streamlined shape and moderate penalties unless accretion is thick or prolonged [4].

Source: Photography by Richard Hann Source: Photography by Richard Hann Source: Photography by Richard Hann

Figure 2.5.: Representative icing morphologies used in this thesis

Figure 2.6 shows three typically seen ice shapes on an airfoil. Horn ice forms at the LE when a liquid film and runback freeze near the stagnation point. It is typical for conditions near the freezing point. The distinct horns introduce large aerodynamic penalties [31, 4]. Streamwise ice appears when water freezes upon impact, building elongated shapes that follow the flow direction [31]. Spanwise-ridge ice arises when freezing concentrates along to the flow, for example due to runback freezing or splashing effects of large droplets. It creates a ridge that can trigger turbulent transition and even early stall [31, 4]. In addition to these shapes, an initial roughness layer forms when small supercooled droplets freeze on impact. It increases the surface roughness from microns toward millimetres, which can lead to early boundary-layer transition, and seeds later horn or ridge-wise ice growth [31, 4].

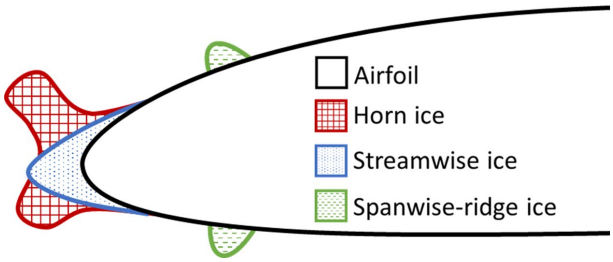

Source: Image by Richard Hann

Figure 2.6.: Typical ice morphologies on an airfoil

2.2.2. Meteorological Icing Conditions (Appendix C)

Icing on aircraft has led to several incidents and therefore to the definition of standardized test conditions. Appendix C of CS/FAR-25 is based on measurements in supercooled clouds and provides design envelopes that manufacturers and researchers can use to test and compare against icing exposure [5, 4]. Within this work, the focus is set on the two meteorological variables that most directly control ice accretion on the airborne platform. The Liquid Water Content (LWC) and the Median Volumetric Diameter (MVD). The LWC (in g/m^3) specifies how much liquid water is available per unit volume of air. It sets the potential water flux that can reach the surface. This variable enters the icing model directly as a source term in the mass- and energy balance (see section 2.3). The MVD (in µm) characterizes the droplet size distribution by the diameter at which half of the total liquid water volume is contained in smaller droplets and half in larger ones. Larger MVD generally implies higher droplet inertia and thus a higher tendency to impact the surface rather than follow the flow around it. Together, LWC and MVD provide a practical description of the cloud conditions relevant for accretion modelling. [5, 4]

Table 2.1.: Appendix C *Continuous Maximum* LWC vs. MVD at selected temperatures at 17.4 nmi

MVD	**0°C**	**−2°C**	**−4°C**	**−10°C**	**−20°C**	**−30°C**
15	0.800	0.758	0.716	0.590	0.300	0.200
20	0.635	0.591	0.547	0.415	0.210	0.140
25	0.500	0.460	0.420	0.300	0.150	0.100
30	0.375	0.344	0.313	0.220	0.110	0.070
35	0.260	0.238	0.216	0.150	0.080	0.050
40	0.155	0.144	0.133	0.100	0.060	0.040

Source: Appendix C of CS/FAR-25 [5]

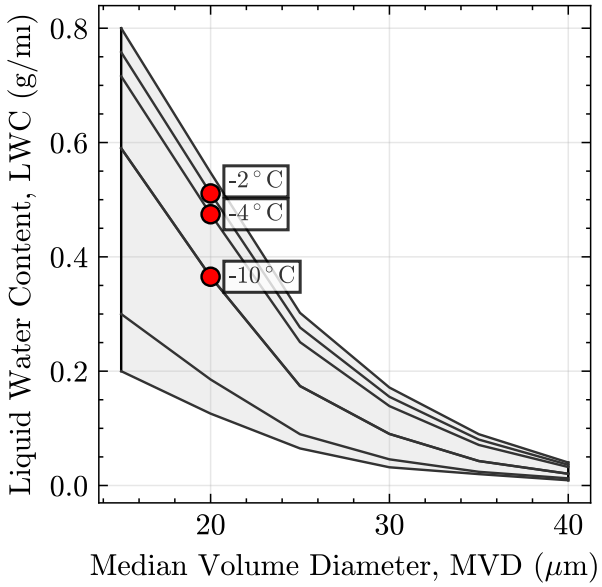

Source: Own visualization of Appendix C of CS/FAR-25 [5]

Figure 2.7.: *Continuous Maximum* Icing envelope from 0°C (top) to -30°C (bottom)

Appendix C offers several envelopes. In this thesis the Continuous Maximum (CM) envelope is used as a conservative reference, because it represents continuous exposure over a longer cloud extent. All simulations use CM values for LWC at specified temperatures and MVD. Intermittent maximum is mentioned explicitly as an important envelope but not used for the analysis. The Appendix C inputs are applied as boundary conditions to the droplet and icing modules in the solver described in section 2.3. This approach abstracts meteorology to a controlled set of parameters while remaining consistent with certification practice [5, 4]. Figure 2.7 visualizes the Appendix C data of table 2.1 for LWC and MVD. Each contour corresponds to a temperature, with the shaded region indicating the continuous icing conditions at a cloud extent of 17.4 nmi. The red markers highlight the three cases used in the simulations, chosen for the selected glaze, mixed, and rime icing regimes.

2.2.3. Aerodynamic Consequences

Icing degrades airfoil aerodynamics through two mechanisms: added surface roughness that can lead to earlier laminar–turbulent transition with higher skin friction, and geometry changes such as horn-ice that can trigger LE separation. The combined effect lowers the lift coefficient C_L, shifts stall to smaller α, and increases the drag coefficient C_D. The effects and different icing morphologies have been thoroughly researched on a wide range of chord lengths and icing conditions [31, 4]. For UAV-relevant (therefore

relevant to AWES) Reynolds numbers, wind-tunnel and numerical studies report performance penalties up to lift reductions of about 35%, stall angle decreases of about 33%, and drag increases up to 400% in the linear region [4]. These trends are consistent with the polar comparisons between clean and iced configurations (see figure 2.8 for a qualitative visualization of these effects).

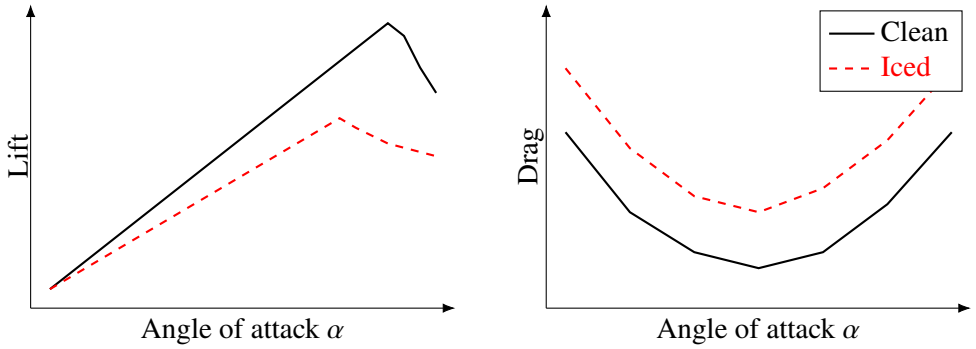

Source: Adaptated from [4]

Figure 2.8.: Lift and drag behavior of clean and iced airfoils.

Icing alters the geometry around the LE and increases surface roughness. The suction peak moves upstream and pressure recovery. At the same time C_L decreases while C_D increases and stall occurs at smaller α. Glaze and mixed ice cause the strongest changes with characteristical horn-ice development while rime shows less impact. Windtunnel experiments and numerical studies at report lift reductions of about 35%, stall-angle decreases of about 33%, and drag increases up to 400% for UAV related scenarios [4]. On a system level, $\Lambda = C_L^3/C_D^2$ indicates how aerodynamic changes show up in power output (equation (2.5)). When C_L/C_D decreases, Λ decreases as well. Their results are reported in detail in chapter 4.

2.3. Fundamentals of CFD

A compressible formulation with the full energy equation is used to obtain accurate wall heat fluxes for icing predictions. The air is modeled as a Newtonian fluid with an ideal-gas equation of state. Heat conduction follows Fourier's law. Transport properties are temperature dependent and follow Sutherland's law for viscosity with a consistent evaluation of thermal conductivity. These are the initial equations to derive the used Reynolds averaged Navier Stokes (RANS) equations The complete section is adapted and condensed from previous work from Hann, Fajt and Henzler [20, 32, 33] and shall give an overview of the underlying physics used by the used solvers in the FENSAP ice module [34]. Additional information has been gathered by the broad compendium of Andersons *Fundamentals of aerodynamics* [23].

The instantaneous, compressible Navier–Stokes equations are

$$\text{Continuity:} \qquad \frac{\partial \rho}{\partial t} + \nabla \cdot (\rho \boldsymbol{u}) = 0, \tag{2.10}$$

$$\text{Momentum:} \qquad \frac{\partial (\rho \boldsymbol{u})}{\partial t} + \nabla \cdot (\rho \boldsymbol{u}\boldsymbol{u}) = -\nabla p + \nabla \cdot \boldsymbol{\tau}, \tag{2.11}$$

$$\text{Energy:} \qquad \frac{\partial (\rho E)}{\partial t} + \nabla \cdot [(\rho E + p)\,\boldsymbol{u}] = \nabla \cdot (\boldsymbol{u}\,\boldsymbol{\tau}) - \nabla \cdot \boldsymbol{q}^m. \tag{2.12}$$

Whereas ρ denotes the density, $\boldsymbol{u}$ the velocity vector, p the static pressure and $E = e + \frac{1}{2}\|\boldsymbol{u}\|^2$ the overall specific energy with e being the state of internal energy. The continuity equation ensures conservation of mass, the momentum equation balances inertia with pressure and viscous forces, and the energy equation links the kinetic and internal energy of the flow through viscous work and heat transfer. Ending up at a total

amount of five equations in the three dimensional form. With the six unknown variables (ρ, u, v, w, p, T) and five equations an additional equation is required to close this system. Defining the equation of state for the medium, the systems closure is achieved. For an ideal gas this relation is given by:

$$p = \rho R T \qquad R \approx 287\,\mathrm{J/(kg\,K)} \tag{2.13}$$

Where as R depicts the specific gas constant - with the value given for air. The two remaining variables; the stress tensor τ and the molecular heat flux $\boldsymbol{q}^m$ are given by:

$$\boldsymbol{\tau} = \mu\left[\nabla \boldsymbol{u} + (\nabla \boldsymbol{u})^\top - \tfrac{2}{3}(\nabla \cdot \boldsymbol{u})\,\boldsymbol{I}\right] \qquad \boldsymbol{q}^m = -\kappa\,\nabla T$$

To model the additional physical properties like viscosity and heat coefficient of a specific medium, empirical models can be used. These derive from experiments or by solving the Boltzmann equation, which requires a significant amount of computational power. In this work, the empirical Sutherland formula for the airs viscosity is given by:

$$\mu(T) = \mu_\infty \left(\frac{T}{T_\infty}\right)^{3/2} \frac{T_\infty + S}{T + S} \tag{2.14}$$

with $S \approx 110\,\mathrm{K}$ for air and taking T_∞, μ_∞ as freestream values. Last, the relation between viscosity, heat capacity and thermal conductivity is given by

$$\mathrm{Pr} = \frac{\mu c_p}{\kappa} \iff \kappa = \frac{\mu c_p}{\mathrm{Pr}} \tag{2.15}$$

The latter equations system can now directly be solved. Solving this system with Computational Fluid Dynamics (CFD) is called a Direct Numerical Simulation (DNS). Solving these equations directly requires an enormous amount of computational power, as the smallest spatial and temporal resolutions of the turbulence have to be resolved to capture the smallest dissipative scales.

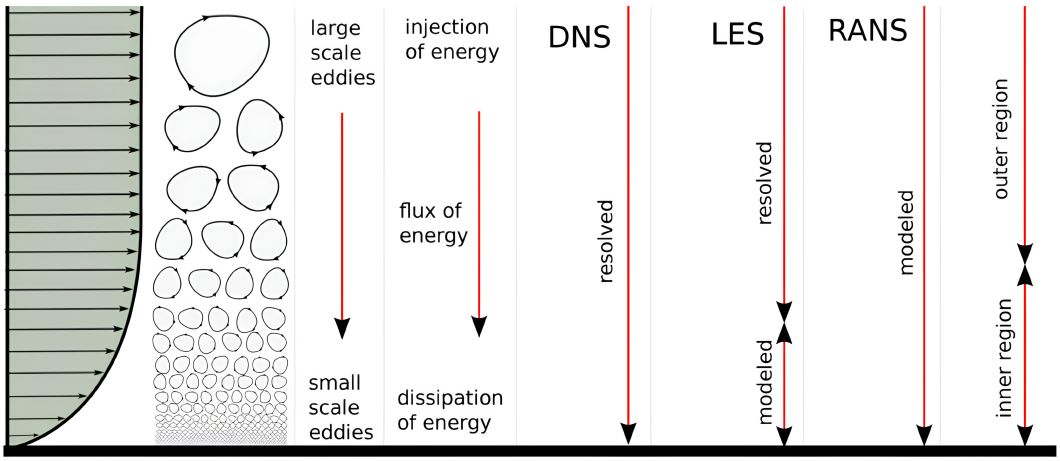

Source: https://www.cfdsupport.com/openfoam-training-by-cfd-support/node346/

Figure 2.9.: Represenation of different turbulence modeling methods in the boundary layer region

As shown in figure 2.9, the figure places turbulence models within the turbulence dissipation (see Kolmogorov cascade) and the near-wall context. For the present simulations, RANS is used. DNS and LES

are not relevant. Instead of resolving these smallest scales, the turbulence can be modeled as well. The main idea is to split any flow variable into their mean value plus an instantaneous fluctuation. This is called Reynolds averaging, however this lies under the assumption of incompressible flows. For compressible flows, the density fluctuations produce additional correlation terms which can not be easily modeled. The general approach of Reynolds averaging is to decompose a variable into

$$\phi = \overline{\phi} + \phi'' \qquad \overline{\phi'} = 0$$

Thereby any flow variable ϕ can be written as

$$\phi = \widetilde{\phi} + \phi'' \qquad \widetilde{\phi} = \frac{\overline{\rho\phi}}{\overline{\rho}} \qquad \overline{\rho\phi''} = 0 \tag{2.16}$$

Here, $\overline{(\cdot)}$ denotes the Reynolds average, $\widetilde{(\cdot)}$ the density-weighted Favre average, and $(\cdot)''$ the Favre fluctuation. This results in the favre-averaged navier stokes equations:

Continuity:
$$\frac{\partial\overline{\rho}}{\partial t} + \nabla\cdot(\overline{\rho}\,\widetilde{\boldsymbol{u}}) = 0 \tag{2.17}$$

Momentum:
$$\frac{\partial(\overline{\rho}\,\widetilde{\boldsymbol{u}})}{\partial t} + \nabla\cdot(\overline{\rho}\,\widetilde{\boldsymbol{u}}\widetilde{\boldsymbol{u}}) = -\nabla\overline{p} + \nabla\cdot\widetilde{\boldsymbol{\tau}} \; - \nabla\cdot\boldsymbol{R} \tag{2.18}$$

Energy:
$$\frac{\partial(\overline{\rho}\,\widetilde{E})}{\partial t} + \nabla\cdot\left[(\overline{\rho}\,\widetilde{E} + \overline{p})\,\widetilde{\boldsymbol{u}}\right] = \nabla\cdot(\widetilde{\boldsymbol{u}}\,\widetilde{\boldsymbol{\tau}}) - \nabla\cdot\boldsymbol{q}^{m} \; - \nabla\cdot(\boldsymbol{R}\cdot\widetilde{\boldsymbol{u}}) - \nabla\cdot\boldsymbol{q}^{t} \tag{2.19}$$

The boussinesq hypothesis is used to model the reynolds stress denoted in (2.20)

$$\widetilde{\boldsymbol{\tau}} = \mu\left[\nabla\widetilde{\boldsymbol{u}} + (\nabla\widetilde{\boldsymbol{u}})^{\top} - \tfrac{2}{3}(\nabla\cdot\widetilde{\boldsymbol{u}})\,\boldsymbol{I}\right] \tag{2.20}$$

The molecular heat flux $\boldsymbol{q}^{m}$ and the turbulent heat flux $\boldsymbol{q}^{t}$ are given by (2.21) whereas the turbulent heat flux can be closed by the Prandtl correlation.

$$\boldsymbol{q}^{m} = -\kappa\,\nabla\widetilde{T} \qquad \boldsymbol{q}^{t} = -\overline{\rho}\,\widetilde{h''\boldsymbol{u}''} \;\approx\; -\frac{\mu_t\,c_p}{\mathrm{Pr}_t}\,\nabla\widetilde{T} \tag{2.21}$$

The additional Reynolds stresses $\boldsymbol{R}$, the mean strain-rate tensor $S_{ij}^{\sim}$ are not closed. Using the Boussinesq hypothesis:

$$R_{ij} = -\overline{\rho}\,\widetilde{u_i''u_j''} = 2\,\mu_t\,S_{ij}^{\sim} - \tfrac{2}{3}\,\overline{\rho}\,k\,\delta_{ij} \qquad S_{ij}^{\sim} = \tfrac{1}{2}\left(\partial_i\widetilde{u}_j + \partial_j\widetilde{u}_i\right) - \tfrac{1}{3}\,\delta_{ij}\,\partial_k\widetilde{u}_k \qquad k = \tfrac{1}{2}\,\widetilde{u_i''u_i''} \tag{2.22}$$

where δ_{ij} is the Kronecker delta ($\delta_{ij} = 1$ for $i = j$, and $\delta_{ij} = 0$ otherwise). The turbulent eddy viscosity (commonly turbulent viscosity) μ_t is introduced. This variable is now ready to be modeled by a set of different approaches, so called turbulence models.

Turbulence Models

The introduction of the eddy viscosity μ_t provides a convenient way to model the effect of turbulence on the mean flow. However, μ_t is not known and must be obtained from a turbulence model. Such models aim to describe the transport and dissipation of turbulent kinetic energy to close the RANS system [35]. Table 2.2 summarizes the models used in FENSAP, their strengths, and limitations.

One-equation models such as Spalart–Allmaras (SA) directly transport a working variable related to μ_t and were developed specifically for external aerodynamic flows [36]. Two-equation models like k–ε or k–ω introduce transport equations for the turbulent kinetic energy k and an additional scale-determining variable

(dissipation rate ε or specific dissipation ω) [37, 38]. The SST k–ω model combines the advantages of both approaches and is widely used for separated external flows [39, 40]. At the highest fidelity, Direct Numerical Simulation (DNS) resolves all turbulent scales without any turbulence model, but is computationally infeasible for engineering flows [35]. FENSAP provides several of these models, in particular the Spalart–Allmaras model, which balances robustness and efficiency for external aerodynamic flows and provides the turbulent viscosity μ_t required for closure of the RANS equations.

Table 2.2.: Overview of relevant turbulence models and their main characteristics

Model	Equations	Strengths	Limitations
Spalart–Allmaras (SA)	1	Low cost, robust, good for attached external flows	Poor in separated or transitional flows
k–ε	2	Simple, widely used, stable	Weak near walls, poor in adverse pressure gradients
k–ω	2	Accurate near walls, better separation prediction	Sensitive to free-stream turbulence
SST k–ω	2	Combines k–ε and k–ω; reliable in separation	Higher computational cost, still RANS-based

Boundary Layer

The boundary layer plays an important role, as it needs to be resolved accordingly to achieve physically meaningful results [41, 42]. This near-wall region can be divided into several sublayers with distinct behaviour, ranging from a viscous regime close to the wall to a turbulence-dominated outer region. To characterize the boundary layer and guide mesh resolution, the following relations are used [42]:

$$y^+ = \frac{u_\tau \, s}{\nu(T_\infty)} \qquad u_\tau = U_\infty \sqrt{\frac{C_f}{2}}. \tag{2.23}$$

Here, y^+ is the dimensionless wall coordinate, s the distance from the wall, ν the kinematic viscosity, and u_τ the friction velocity derived from the skin-friction coefficient C_f. Depending on the value of y^+, the following sublayers can be distinguished [41]:

- $y^+ \lesssim 5$: viscous sublayer, where velocity varies linearly with y and viscous effects dominate.
- $5 \lesssim y^+ \lesssim 30$: buffer layer, where both viscous and turbulent effects are important.
- $y^+ \gtrsim 30$: logarithmic layer, where turbulence is the governing mechanism.

For wall-resolved RANS simulations, the first grid cell should be placed inside the viscous sublayer, i.e. $y^+ \approx 1$. If wall functions are employed instead, the first cell can be placed higher in the logarithmic region, typically at $y^+ \approx 30$–100 [42].

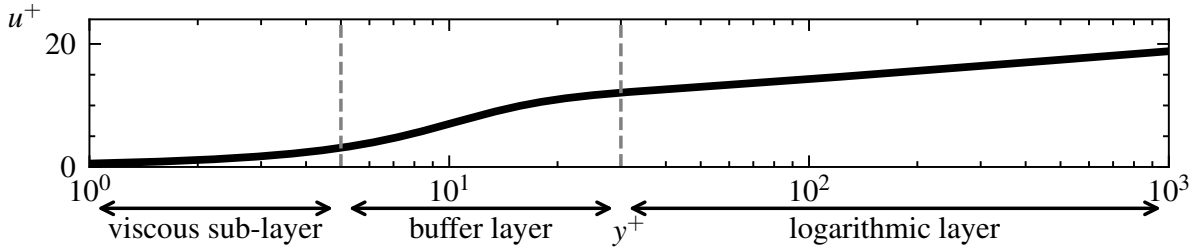

Source: Adapted from `https://doc.cfd.direct/notes/cfd-general-principles/turbulent-boundary-layers`

Figure 2.10.: Schematic of the individual sublayers in the boundary layer region

The kinematic viscosity at the freestream temperature is taken from tabulated values using linear interpolation:

$$\nu(T_\infty) = \nu_1 + \frac{\nu_2 - \nu_1}{T_2 - T_1}\left(T_\infty - T_1\right). \tag{2.24}$$

The Reynolds number based on a reference length l is

$$Re = \frac{U_\infty\, l}{\nu(T_\infty)} = \frac{\rho_\infty\, U_\infty\, l}{\mu(T_\infty)} \qquad \mu(T_\infty) = \rho_\infty\, \nu(T_\infty). \tag{2.25}$$

A flat-plate estimate is used for the skin-friction coefficient,

$$C_f = 0.026\, Re^{-1/7}, \tag{2.26}$$

which is commonly employed for turbulent boundary layers on smooth flat plates [41, 42]. Combining the latter equations gives a closed form for the first-cell height s for a target y^+. This approach has been developed programmatically by Hann [20] and was migrated and adapted to Python within this work:

$$s \;=\; \frac{y^+\,\nu(T_\infty)}{u_\tau} \;=\; \frac{y^+\,\nu(T_\infty)}{U_\infty\sqrt{0.013}}\left(\frac{U_\infty\, l}{\nu(T_\infty)}\right)^{1/14}. \tag{2.27}$$

Droplet Impingement (Drop3D)

In FENSAP the module Drop3D computes the transport and deposition of supercooled water droplets. Two different formulations exist: a Lagrangian tracking of individual particles, and an Eulerian formulation, where the droplets are modeled as a continuum. The latter is generally used for icing prediction, as it integrates naturally with the flow solver.

In the Eulerian approach, the droplet concentration α and droplet velocity $\boldsymbol{V}_d$ are solved from a two-fluid system of continuity and momentum equations:

$$\frac{\partial \alpha}{\partial t} + \nabla\cdot(\alpha \boldsymbol{V}_d) = 0 \tag{2.28}$$

$$\frac{\partial(\alpha \boldsymbol{V}_d)}{\partial t} + \nabla\cdot(\alpha \boldsymbol{V}_d \otimes \boldsymbol{V}_d) = -\frac{C_D Re_d}{24K}\,\alpha(\boldsymbol{V}_d - \boldsymbol{V}_a) + \alpha\left(1 - \frac{\rho_a}{\rho_d}\right)\frac{1}{Fr^2} \tag{2.29}$$

Here ρ_a and ρ_d are the densities of air and water droplets, $\boldsymbol{V}_a$ is the air velocity, and C_D is the drag coefficient depending on the droplet Reynolds number

$$Re_d = \frac{\rho_a\, d\, \|\boldsymbol{V}_a - \boldsymbol{V}_d\|}{\mu_a}$$

The inertial parameter K and the local Froude number Fr are given by

$$K = \frac{\rho_d\, d^2 V_{a,\infty}}{18\mu_a} \qquad Fr = \frac{\|V_{a,\infty}\|}{\sqrt{L_\infty g_\infty}}$$

From the solution of these equations, the surface mass flux of impinging droplets $\dot{m}_{\text{imp}}$ and the collection efficiency $\eta(\boldsymbol{x}_w)$ are obtained, which form the input to the subsequent ice accretion module. The aerodynamic drag on the droplets enters through the drag coefficient C_D, which depends on the droplet Reynolds number Re_d. In FENSAP–ICE the Water–default model is used, based on an empirical correlation for spherical droplets:

$$C_D = \frac{24}{Re_d}\left(1 + 0.15\, Re_d^{0.687}\right) \qquad Re_d \le 1300 \tag{2.30}$$

$$C_D = 0.4 \qquad Re_d > 1300 \tag{2.31}$$

This correlation is widely used for dispersed liquid droplets and provides a smooth transition from the Stokes regime at very low Re_d to the inertial regime at higher values. Although the validity range is not formally limited by Re_d, droplet deformation is generally observed above $Re_d \approx 250$, so that the assumption of perfectly spherical droplets becomes less accurate.

Ice Accretion (Ice3D)

On a solid surface exposed to supercooled droplets, ICE3D models the formation of a thin liquid film with thickness $h_f(x, y, t)$. The film is driven downstream by wall shear stress, centrifugal forces and gravity, and may either freeze, evaporate/sublimate, or remain liquid and run back. To describe these processes, ICE3D solves two coupled conservation equations for all solid surfaces.

The liquid film formed by impinging droplets is driven mainly by the aerodynamic wall shear stress $\boldsymbol{\tau}_{q,\text{wall}}$ acting along the surface. Assuming a very thin film ($h_f \lesssim 10\ \mu$m, typical in icing/anti-icing conditions), a linear velocity profile across the film thickness is a reasonable approximation. With no-slip at the wall ($\boldsymbol{u}_f = 0$ at $y = 0$), the local velocity distribution reads

$$\boldsymbol{u}_f(\boldsymbol{x}, y) = \frac{y}{\mu_f}\,\boldsymbol{\tau}_{q,\text{wall}}(\boldsymbol{x}) \tag{2.32}$$

where μ_f is the dynamic viscosity of the liquid film. Averaging this profile over the thickness h_f yields the mean film velocity:

$$\overline{\boldsymbol{u}}_f(\boldsymbol{x}) = \frac{1}{h_f}\int_0^{h_f} \boldsymbol{u}_f(\boldsymbol{x}, y)\,dy = \frac{h_f}{2\mu_f}\,\boldsymbol{\tau}_{q,\text{wall}}(\boldsymbol{x}) \tag{2.33}$$

This velocity serves as the advective transport term in the subsequent mass and energy balances for the film.

The first equation expresses conservation of film mass:

$$\rho_f\left[\frac{\partial h_f}{\partial t} + \nabla\cdot\left(\overline{\boldsymbol{u}}_f h_f\right)\right] = V_\infty LWC\,\beta - \dot{m}_{\text{evap}} - \dot{m}_{\text{ice}} \tag{2.34}$$

Here, the source term is given by droplet impingement ($V_\infty LWC\,\beta$), while sinks of mass are evaporation/-sublimation ($\dot{m}_{\text{evap}}$) and ice accretion ($\dot{m}_{\text{ice}}$).

The second equation describes conservation of film energy:

$$\begin{aligned}\rho_f\left[\frac{\partial h_f c_f T_f}{\partial t} + \nabla\cdot\left(\overline{\boldsymbol{u}}_f h_f c_f T_f\right)\right] &= \left(e_d + \tfrac{1}{2}V_d^2\right)V_\infty LWC\,\beta - \dot{m}_{\text{evap}}L_{\text{evap}} \\ &\quad + \dot{m}_{\text{ice}}\left(L_{\text{fus}} - c_{\text{ice}}(T_f - T_{\text{ice}})\right) - c_h(T_f - T_{\text{rec}}) \\ &\quad + \sigma\epsilon\left(T_\infty^4 - T_f^4\right) + Q_{\text{anti-icing}}\end{aligned} \tag{2.35}$$

Equations equations (2.34) and (2.35) follow the classical description of an unheated surface in supercooled icing conditions as introduced by Messinger [43]. The control volume is the thin water film that covers the surface. Mass enters through droplet impingement and leaves through evaporation or freezing into ice. The energy balance collects the kinetic and thermal energy of the arriving droplets, latent heat release or removal during phase change, convective heat transfer with the air, radiative heat exchange, and possible input from an anti-icing system. In FENSAP–ICE this balance is implemented as such: the film thickness and temperature are updated on each icing step using the aerodynamic inputs from Drop3D and Fensap and the ice thickness is advanced accordingly. The present work uses this formulation without anti-icing input and neglects radiative terms, so that convection and phase change are the dominant contributions.

This balance accounts for:

- kinetic and thermal energy of impinging droplets
- latent heat loss by evaporation/sublimation
- latent heat release by freezing of a film fraction
- convective heat exchange with the flow (c_h)
- radiative heat exchange ($\sigma\epsilon$)
- and possible input from an anti-icing system ($Q_{\text{anti-icing}}$)

The film velocity $\overline{\boldsymbol{u}}_f$ is approximated from wall shear stress by assuming a linear velocity profile across the film thickness. Since typical icing films are thinner than 10 μm, this assumption is sufficiently accurate and avoids resolving the full Navier–Stokes equations within the film. The aerodynamic quantities LWC, β, V_d and e_d are supplied by the Drop3D calculation. The evaporative flux $\dot{m}_{\text{evap}}$ is parameterized via a heat transfer coefficient (htc).

Atmospheric Model

The flow regime used in the following chapter is in the lower subsonic region. The Mach number is introduced as a nondimensional reference speed ratio.

$$M = \frac{U}{a} \tag{2.36}$$

Speed of sound follows

$$a = \sqrt{\gamma R T} \tag{2.37}$$

Standard values use the International Standard Atmosphere at sea level [**ISO2533**]. With $T = 288.15\,\text{K}$, $\gamma = 1.4$ and $R = 287.05\,\text{J}\,\text{kg}^{-1}\,\text{K}^{-1}$ this gives $a = 340.29\,\text{m}\,\text{s}^{-1}$. An operating speed of $U = 50\,\text{m}\,\text{s}^{-1}$ thereby corresponds to $M = 0.147$ by (2.36).

Altitude affects temperature, density, and the speed of sound. In the ISA troposphere,

$$T(h) = T_0 - Lh, \qquad p(h) = p_0 \left(\frac{T(h)}{T_0}\right)^{g_0/(LR)} \qquad \rho(h) = \frac{p(h)}{R\,T(h)} \tag{2.38}$$

3. Simulation Methodology

This chapter gives an overview of the used methods and their connecting interfaces. Starting with the preprocessing. The refinement of the CAD-model, the key geometries will be extracted. These geometries are then being refined in xfoil to increase their resolution for the meshing procedure. The used meshing procedure and the used mesh layout is portrayed to have an idea of the different key characteristics of the used mesh. For the simulation campaign a 2.5D approach is selected based on literature [20, 33, 32]. For the actual solver this mesh is processed with the standalone Ansys FENSAP module. Three submodules are available in this module, covering flow, droplet and ice solution. This solution needs to be repeated and requires a remeshing between the steps which is covered after the solver sections. Concluding, this chapter shows the used orchestration pipeline in python used for reproducing the results as well as finallizing the solutions with a postprocessing unit. The solver principle is shown in figure 3.1 for clarification.

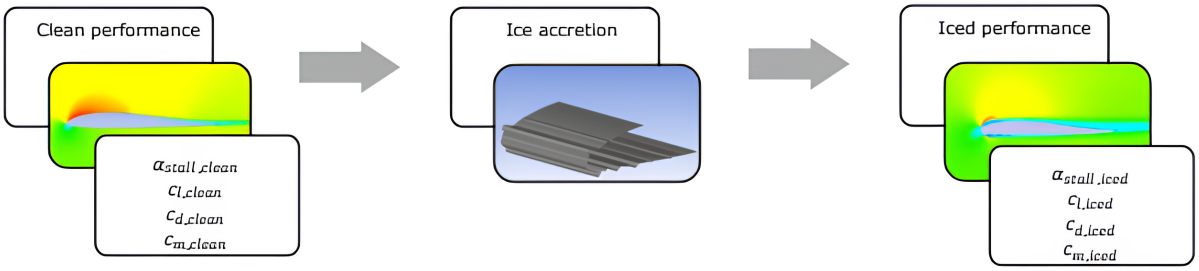

Source: Adapted from Hann [20]

Figure 3.1.: Solving principle in an icing simulation

i **3D model** Preparation and simplification of the 3D model. Extraction of the airfoil geometries

ii **XFoil** Refinement of the geometries, preanalysis of the geometry

iii **Pointwise** Meshing procedure and variables for the meshing scripts.

iv **FENSAP** Used configurations for the flow solver module and the other droplet and icing modules.

v **DROP3D** Used configurations for the flow solver module and the other droplet and icing modules.

vi **ICE3D** Used configurations for the flow solver module and the other droplet and icing modules.

vii **glacium** custom python package to orchestrate the solver pipeline

3.1. Geometry and CAD Preparation

Kitemill kindly provided a closed STL model of the KM1 platform for this thesis. A non-disclosure agreement applies, so the original airfoil geometry is not published. Instead of slicing many sections from the STL, an anonymized airfoil is used that preserves characteristics. The mean aerodynamic chord is taken from the KM1 dataset, $\bar{c} = 0.431\,\text{m}$, and a span width of 7.4 m has been taken (published by kitemill). Further information is not deemed relevant, but listed in table 3.1 for completeness.

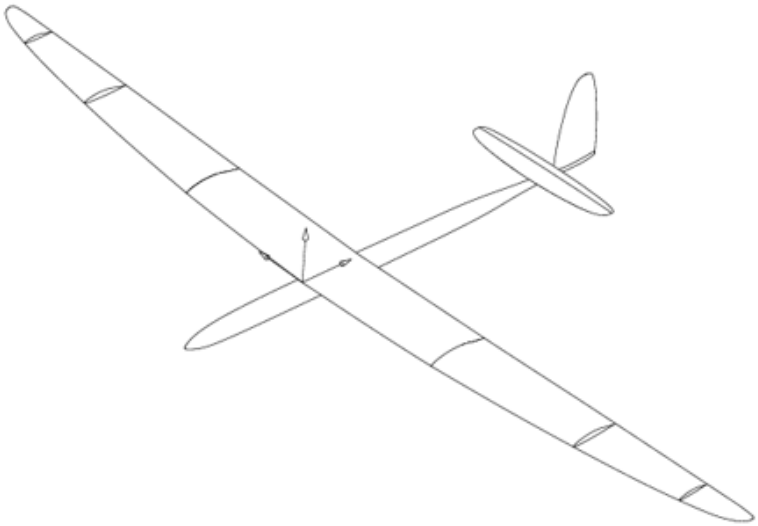

Figure 3.2.: Schematic of the simplified KM1

The STL-file is imported and cleaned to an extent required for airfoil extraction. All non-relevant components suchs as rotors, fuselage, horizontal and vertical stabilizers have been removed. Smoothing has been performed on the wing area to prepare the geometry for a sectional cut. The resulting partial xy-projection from the cut is then taken as a base for point generation. The coordinates of were extracted and the extracted partial airfoil compared visually against similar airfoils. These airfoils have then been revised against comparable operating ranges. The chosen airfoil for the wing section is AH63K127, which is designed to be used with flaps. A public airfoil AH 63-K-127/24 is used and matched to thickness, camber and LE radius and results are given as relative icing changes at $Re \approx 1.7\dot{1}0^6$.

Table 3.1.: Geometry data for the airfoil

Airfoil	AH 63-K-127/24
Mean chord $\bar{c}$	0.431 m
Spanwidth b	7.4 m
Max thickness	12.7% c at $x/c = 0.40$
Max camber	3.8% c at $x/c = 0.44$
Mach range	0.15 to 0.20

3.2. Airfoil Refinement with XFOIL

XFOIL is used as a tool to resample the baseline airfoil for meshing [44]. The process loads the baseline coordinates, regenerates the panel distribution, and applies a Trailing Edge (TE) gap with smooth blending. Point order and orientation are kept. The output is a coordinate file used directly for meshing. The key settings are listed in table 3.2.

1. Re-paneling: load baseline, set the target number of panels, rebuild the surface panels, write an intermediate coordinate file.
2. Optional TE gap: load the intermediate file, set gap size and blending, execute the edit, re-panel, write the final coordinate file.

Table 3.2.: XFOIL resampling parameters

Item	**Value**
Target panel count N	400
TE gap	$g_{\mathrm{TE}} = \dfrac{1\,\mathrm{mm}}{c}$
Gap blending factor	0.6
Chord length c	0.431

Table 3.2 lists the settings used in the XFOIL resampling step. The surface is re-paneled with a target count of $N = 400$ to obtain stable spacing for meshing. The TE gap follows the chord-scaled rule $g_{\mathrm{TE}} = \frac{1\,\mathrm{mm}}{c}$. A blending factor of 0.6 smooths the TE-geometrical transition. The chord reference used here is the mean chord length of the KM1 described before.

3.3. Mesh Generation with Pointwise

Mesh generation follows a 2.5D assumption. A hybrid grid is used with TRex prism layers at the wall and an unstructured farfield. Geometry comes from the XFOIL-processed airfoil and is read by an automated and parameterized Pointwise script within the processing pipeline. The intent is a reproducible setup for clean-airfoil simulations and the according icing runs. The meshing procedures of previous work have been automated and thereby a closer investigation of vertical and horizontal spacing along the airfoils wall is given.

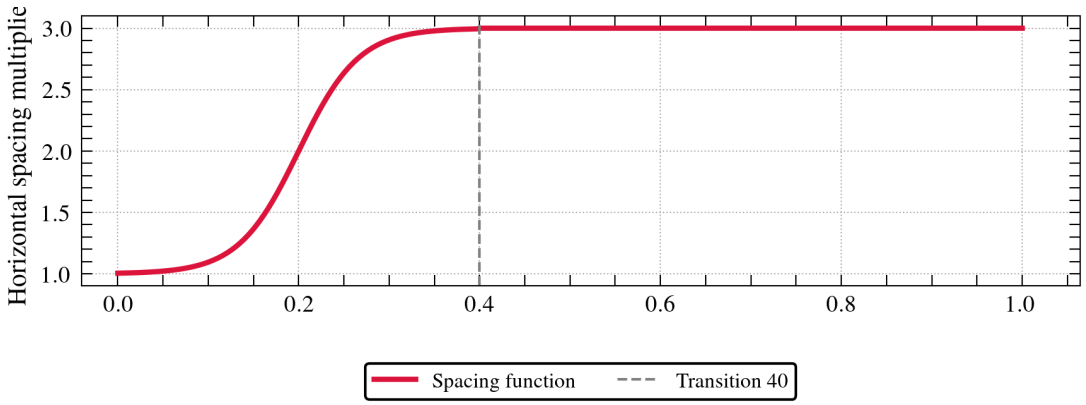

Source: Author

Figure 3.3.: Horizontal spacing function over the airfoil arc-length

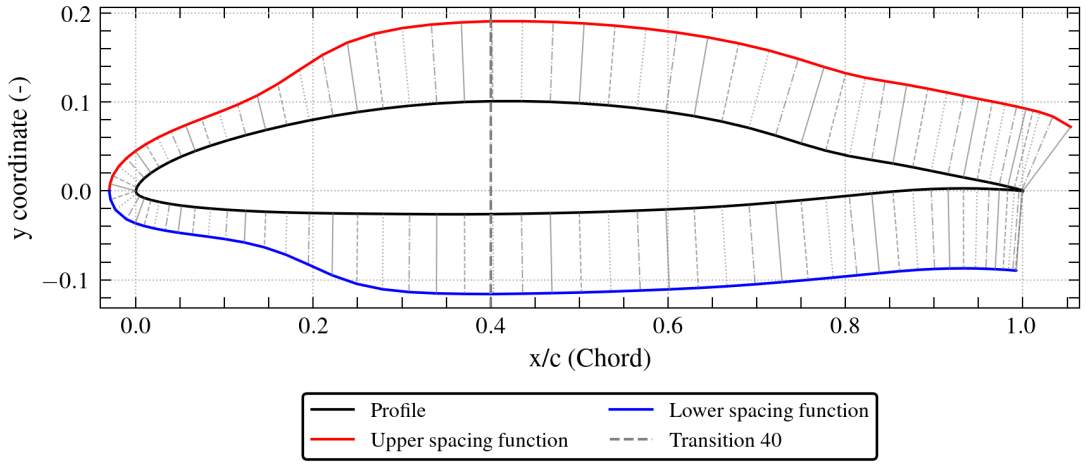

Source: Also author

Figure 3.4.: Horizontal spacing multiplier over the airfoil arc-length

The farfield is a circle of radius $20c$ centered at the airfoils LE. This limits feedback during operating conditions throughout the ice accretion. The section is extruded by a single cell with span $0.1c$ in z to create the 2.5D mesh. Two arc-length spacings control the arcwise surface resolution. A finer LE spacing s_1 and a coarser TE spacing s_2 with ratio $s_2/s_1 = 3$. The default Pointwise spacing function tanh blend transitions from s_1 to s_2. The transition is set to be at $x/c = 0.4$ as as in previous work by Henzler [33]. After the transition the spacing is kept constant at s_2. This distribution has proven robust for icing, since most accretion occurs on the forward part of the airfoil. The function is displayed in figure 3.3. The x-scale depict the nondimensional arclength s over the airfoils upper and lower wall where zero corresponds to the LE and one to the TE. For clarification purposes this spacing has been projected onto the airfoils wall in figure 3.4 indicating higher values for coarse regions and lower for finer regions. Parameterizing the

horizontal spacing like this makes it convenient for the subsequent grid convergence studies conducted in chapter 4 as the function can be scaled by an additional variable. This single variable is directly linked to the mean horizontal step size used in the grid convergence study in chapter 4.

Table 3.3.: Pointwise setup (key parameters).

Variable	Value
Chord length c	0.431 m
Farfield radius	$20c$
Farfield points	600
Extrusion span z	$(0.1c)$
Surface spacing s_1 (LE)	8.0×10^{-5} m
Surface spacing s_2 (TE)	2.4×10^{-4} m
Spacing blend	tanh, transition at $x/c = 0.4$
First prism height	from equation (2.27)
TRex growth	1.15
TRex full layers (min)	10
TRex layers (max)	500
Trailing-edge points	4

The first-layer height is set from a target y^+ and is set to a constant value of 1/3. This provides a sufficient vertical resolution in order to capture Boundary Layer (BL) effects up to the viscous sublayer using the closed form in equation (2.27). TRex grows the layers with a factor of 1.15. At least 10 full layers are enforced and up to 500 layers are allowed. This balances wall resolution and smooth transition to the unstructured farfield. The airfoil is split into a front and a back part to isolate the icing-relevant region. The number of points is determined by the set arcwise spacing function. The circular farfield uses 600 points. These counts provide a smooth hybrid grid transition. After meshing the two dimensional region, the mesh is extruded in spanwise z-direction by $(0.1c)$. All mentioned values are summarized in table 3.3. The generated script writes a Fluent mesh for FENSAP and sets the according boundary conditions. Further reference for the scripts is found in appendix A.

3.4. Solver Configuration

The icing simulations are carried out with FENSAP [45]. The software couples a compressible RANS flow solver (FENSAP) with a droplet impingement module (DROP3D) and an ice accretion module (ICE3D). In the present work these modules are used in a multshot sequence: for each icing time step the flow field is solved first, followed by the droplet transport, and finally by the ice accretion and remeshing of the surface. The resulting iced geometry is then used as input for the next flow solution, as illustrated in figure 3.5. The underlying models and governing equations are summarized in section 2.3.

The following subsections describe the numerical setup for each module and highlight the main modelling decisions. Detailed parameter values are listed in tables 3.4 to 3.6.

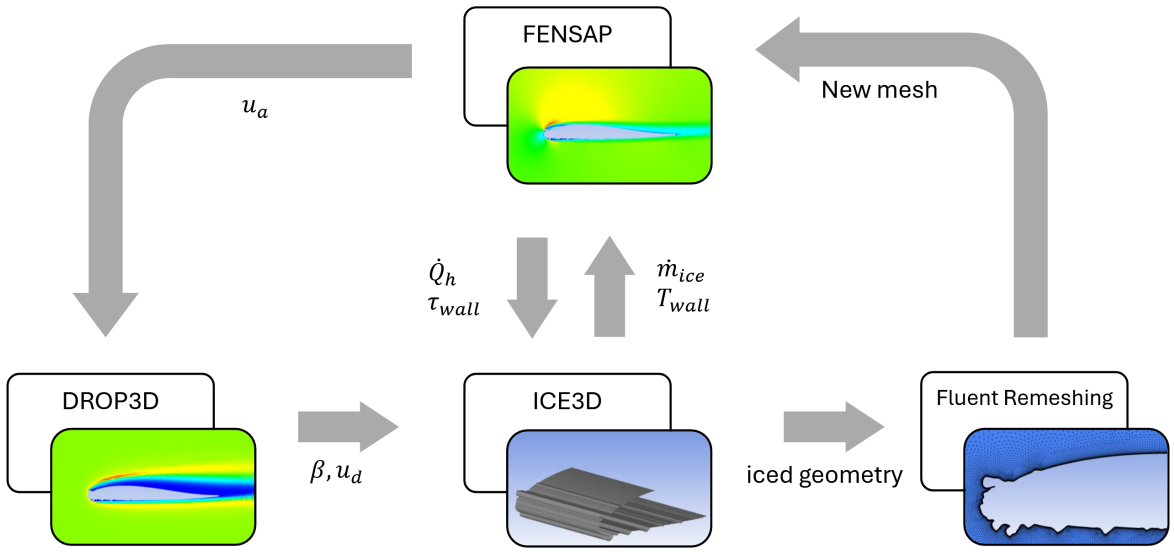

Source: Adapted from Hann [20]

Figure 3.5.: Solving principle in an icing simulation

3.4.1. FENSAP

FENSAP computes the compressible RANS flow field around the 2.5D airfoil geometry. It solves the compressible, Favre-averaged Navier–Stokes equations with energy coupling as introduced in section 2.3. Turbulence is modelled with the Spalart–Allmaras (SA) one-equation model, which has shown robust behaviour for external aerodynamics with icing on UAV and AWE configurations. Only the air phase is solved in this module; the droplet equations are handled separately in DROP3D. To account for temperature changes due to icing, the full energy equation is activated. In the clean reference configuration the wall is treated as a smooth surface. For the first icing shot a specified sand-grain roughness with height $k_s = 0.004\,\text{mm}$ is applied, as listed in table 3.4. The boundary layer is fully resolved with a target first-cell height of $y^+ \approx 1$ according to equation (2.27), and the transition is treated as free, thusno explicit transition model is used.

The reference flow quantities (pressure, temperature, velocity magnitude and angle of attack) are prescribed in the farfield according to the case definition in section 4.1. The characteristic length is the airfoil chord, which is also used for the definition of the reference area. The 2.5D domain is extruded in spanwise direction with zero yaw angle, such that the inflow is aligned with the x-axis. Boundary conditions are inherited from the mesh generation in POINTWISE: the airfoil surface is treated as a no-slip wall with

prescribed wall temperature $T_w = 274.394\,\mathrm{K}$ and zero imposed heat flux, the outer circular boundary as a farfield condition, and the spanwise planes as symmetry boundaries. The wall temperature is set slightly above the adiabatic stagnation temperature to avoid non-physical freezing at the stagnation point and to maintain numerical stability. A steady RANS solution is computed. The time integration mode is set to *steady* with a Courant–Friedrichs–Lewy (CFL) number of 300, reduced only if the solution fails to converge. A maximum of 700 pseudo-time steps per case is used. Variable relaxation is enabled with the default settings. Convective terms are stabilized with the streamline-upwind artificial viscosity scheme with cross-wind dissipation of 1×10^{-7} and first-order artificial viscosity, as summarized in table 3.4.

Table 3.4.: FENSAP solver configuration for the clean configuration
Source: Author, layout adapted from Henzler [33]

Model	
Physical model	Air
Momentum equations	Navier–Stokes
Energy equation	Full PDE
Turbulence model	Spalart–Allmaras (ice accretion) / k-ω SST (clean)
Eddy/laminar viscosity ratio	1×10^{-5}
Relaxation factor	1
Number of iterations per step	1
Surface roughness (Shot 1)	Specified sand-grain roughness, height = 0.004 mm, No roughness (clean)
Transition	No transition (fully turbulent)
Body forces	None
Boundaries	
Wall: Surface type	No-slip wall
Wall: Temperature	274.394 K
Wall: Heat flux	$q_w = 0$
Wall: Rotation	Disabled
Solver	
Time integration mode	Steady Reynolds Averaged Navier Stokes (RANS)
CFL number	300
Max. number of time steps	700
Variable relaxation	On
Artificial viscosity scheme	Streamline upwind
Cross-wind dissipation	1×10^{-7}
Artificial viscosity order	First order
Accuracy setting	100% (default)
Output	
Final solution	Written at end of run
Write y^+ to solution	Enabled

3.4.2. Drop3D

DROP3D computes the impingement of supercooled water droplets using the Eulerian two-fluid formulation described in section 2.3. In this approach the droplet field is treated as a continuum with volume fraction α and droplet velocity $\boldsymbol{V}_d$, which satisfy a continuity and a momentum equation coupled to the air velocity $\boldsymbol{V}_a$. The solution provides the collection efficiency β and the impact mass flux $\dot{m}_{\text{imp}}$ on the airfoil surface, which serve as input to the ice accretion model in ICE3D. In the present setup only the droplet equations are solved in DROP3D. The air solution from FENSAP is taken as frozen. Droplets are assumed spherical and monodisperse, with a median volume diameter (MVD) specified by the case definition in section 4.1. The empirical *Water–default* drag correlation is used for the droplet drag coefficient C_D, consistent with the formulation in section 2.3. No feedback of the droplets on the air phase is considered, which is justified by the low liquid water contents and volume fractions in the Appendix C icing envelope. Evaporation and vapor transport are neglected in DROP3D; thermal effects are handled solely in ICE3D. Super-large droplets (SLD) are disabled. Only gravity is retained as a body force on the droplets, and particle reinjection is disabled.

Table 3.5.: Numerical setup of the droplet impingement model DROP3D.
Source: Author, layout adapted from Henzler [33]

Model	
Physical model	Droplets
Particle type	Droplets
Droplet drag model	Water–default
SLD option	Disabled
Conditions	
LWC	Case Definition in section 4.1
MVD	20 μm
Water density	$\rho_d = 1000\,\text{kg m}^{-3}$
Droplet distribution	Monodisperse
Solver	
CFL number	20
Max. number of time steps	120

The environmental conditions (pressure, temperature, freestream velocity) are kept consistent with the FENSAP setup. The liquid water content (LWC), water density, and MVD are specified according to the meteorological cases in **??**. Eulerian two-fluid approach avoids statistical noise from particle tracking and is recommended for dilute droplet fields in the FENSAP documentation. It has also been used successfully for similar Reynolds numbers and Appendix C conditions in previous icing studies on UAVs and small aircraft, so that the present setup follows an established modelling path. A summary of the DROP3D settings is given in table 3.5.

3.4.3. Ice3D

ICE3D computes ice accretion and runback on the airfoil surface. The module implements an equilibrium film model derived from the Messinger formulation, as outlined in section 2.3. A thin water film with thickness h_f and mean velocity $\bar{u}_f$ is resolved on the surface. Mass and energy conservation in the film

balance the incoming droplet flux, latent heat terms for freezing, evaporation and sublimation, radiative exchange, and convective heat transfer. The driving quantities for the film model are the wall shear stress and heat flux from FENSAP and the collection efficiency and impact flux from DROP3D.

For the present work the *glaze – advanced* ice model is used, which accounts for runback and refreezing of water and is appropriate for the mixed and glaze icing conditions of interest. Beading is activated to represent the increased roughness of the ice surface. The ice density is kept at the default value of $917\,\mathrm{kg\,m^{-3}}$. A concavity fix is applied above a surface angle of 70° to avoid non-physical overhangs in highly curved leading-edge regions.

Only the front part of the airfoil, as defined in the meshing step, is enabled for icing. The aft portion of the chord is kept ice-free, since previous tests have shown negligible ice accretion in this region and a higher risk of remeshing errors if the entire surface is allowed to grow ice. After each icing time step a new surface mesh is generated on the updated geometry and passed back to FENSAP for the next flow solution.

The environmental conditions (pressure, temperature, velocity, LWC, MVD) are identical to the DROP3D and FENSAP setups. The total icing time and the distribution into multishot steps are specified in the simulation campaign in chapter 4. The main ICE3D parameters are summarized in table 3.6.

Table 3.6.: Ice3D configuration: film model, thermodynamics, and coupling.
Source: Author, layout adapted from Henzler [33]

Model	
Ice–water model	*Glaze – advanced*
Beading	Enabled
SLD	Disabled
Conditions	
Ice density	$\rho_{\mathrm{ice}} = 917\,\mathrm{kg\,m^{-3}}$
Boundaries	
Airfoil wall (LE)	Icing enabled
Airfoil wall (TE)	Icing disabled
Solver	
Total icing time	Determined by multishot sequence in chapter 4
Remeshing	Ansys remeshing

The glaze–advanced option is chosen because the investigated Appendix C conditions are dominated by mixed and glaze icing at subzero temperatures typical for coastal AWE operation. Restricting icing to the leading-edge wall patch reflects the observation that most accretion occurs in this region and reduces the risk of remeshing failures on the aft part of the airfoil. This configuration follows the practice in recent numerical icing studies and provides a robust basis for the multishot simulations in chapter 4.

3.5. Numerical Validation Techniques

Numerical results must be sufficiently independent of spatial and temporal resolution. Since each refinement step increases the computational cost, a balance between accuracy and runtime is required. In this work the sensitivity of the solution is assessed by varying the spatial and temporal step size while keeping all other parameters fixed as proposed by Roache [46] and Celik [47]. As quantities of interest the lift and

drag coefficients are monitored. The procedures below are followed for all reference and icing cases. The corresponding results are discussed in chapter 4.

3.5.1. Grid Dependency Study

For the spatial study three systematically refined grids are used. An initial step size h_1 is defined and multiplied by a constant refinement ratio r (typically $r = 2$ or $r = \sqrt{2}$) to obtain $h_2 = r\,h_1$ and $h_3 = r^2 h_1$. The resulting grids are denoted as fine (F, $i = 1$), medium (M, $i = 2$) and coarse (C, $i = 3$).

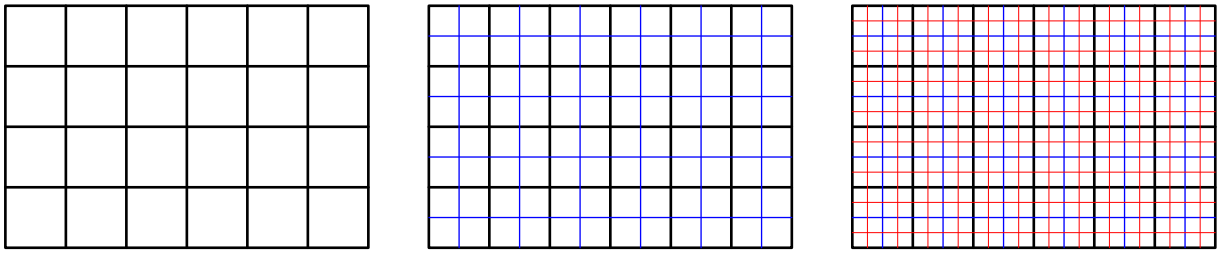

h_3 h_2 h_1

Source: Carefully crafted by Author

Figure 3.6.: Schematic representation of the different grid sizes for coarse, medium and fine resolution.

On each grid the same simulation is performed and a scalar quantity of interest ϕ (e.g. lift or drag coefficient) is extracted. The observed order of convergence p is then estimated from the three solutions using

$$p = \frac{\ln\left(\dfrac{\phi_3 - \phi_2}{\phi_2 - \phi_1}\right)}{\ln(r)} \tag{3.1}$$

where r denotes the refinement ratio and ϕ_i the result on grid i. With p known, a Richardson extrapolation provides an approximation ϕ_{RE} for a fully resolved grid:

$$\phi_{\mathrm{RE}} = \phi_1 + \frac{\phi_1 - \phi_2}{r^p - 1} \tag{3.2}$$

To quantify the discretisation error between two grids the Grid Convergence Index (GCI) is used,

$$GCI_{i,i+1} = \frac{|\phi_{i+1} - \phi_i|}{\phi_i\,(r^p - 1)} \tag{3.3}$$

and, for the specific triplet (F,M,C),

$$GCI_{21} = \frac{|\phi_2 - \phi_1|}{\phi_1\,(r^p - 1)} \qquad GCI_{32} = \frac{|\phi_3 - \phi_2|}{\phi_2\,(r^p - 1)} \tag{3.4}$$

In this work the grids are considered sufficiently resolved when the GCI is small compared to a set tolerance and when $\phi_2/\phi_1 \approx 1$.

3.5.2. Time Step Study

For multishot icing simulations the geometry changes after each icing step and a pure spatial study would require a separate verification for every remeshed grid. Instead, the temporal resolution is assessed by

varying the icing time step while keeping the spatial discretisation fixed. The initial conditions are identical for all runs, and the quantity of interest is again the resulting lift coefficient after the complete icing sequence.

The same idea as in the grid study can be applied by treating the icing time step Δt_{ice} as a one-dimensional grid spacing and using the relations from equations (3.1), (3.3) and (3.4) in time. In practice the selected time steps are chosen such that

$$\frac{\phi_{\Delta t_2}}{\phi_{\Delta t_1}} \approx 1 \tag{3.5}$$

for the two finest temporal resolutions. The selected values of Δt_{ice} and the corresponding results of the time step study are discussed in detail in the simulation campaign in chapter 4.

3.6. Orchestration Pipeline with *glacium*

Due to the large amount of parameter value combinations, the simulation setup has shown to be highly error prone due to human error. To counter these issues, an automated orchestration pipeline for the previously desvribed methods has been developed. This not only rules out configuration mistakes, but also makes the pipeline fully reproducable. By using the command line interfaces and scripts for these methods, the parameters can be reduced to the environmental conditions and the selected airfoil geometry. This pipeline works as a wrapper interface for the selected software tools and provides the user with an application programming interface (API). The API then preprocesses all the different variables and allows the setup and execution of the whole campaign. Within this thesis, the *glacium* framework is used primarily as an enabling tool to generate the simulation data in a consistent way rather than as a research object in its own. Accordingly, only a concise overview of the workflow is given here, while implementation details remain in the underlying Python infrastructure.

4. Simulation Campaign

The simulation campaign summarizes the core results for the impact of in-flight icing on the aerodynamic performance of the selected airfoil and on the power potential of an airborne wind energy (AWE) system. The simulations build directly on the numerical framework introduced in chapter 3: geometry preparation, meshing, solver configuration, and the verification procedures for spatial and temporal discretization.

The campaign proceeds in three steps. First, the operating conditions are defined in terms of Appendix C icing parameters and typical AWE flight settings (section 4.1). Second, the mesh sensitivity of the reference cases is explored using the grid dependency and time step studies from section 3.5, with the corresponding results reported here for the mixed-ice reference case (sections 4.2 and 4.3). Third, the verified setup is used to compute multishot ice accretion and the resulting clean and iced polars for glaze, mixed and rime icing (sections 4.4 and 4.5). All aerodynamic metrics in this chapter are extracted from the two-dimensional 2.5D simulations. They provide the input for the loyd factor Λ and efficiency measures discussed later in chapter 5.

4.1. Case Definition

To evaluate icing penalties for the AWE reference system, three Appendix C conditions are selected: glaze, mixed, and rime at near-freezing and colder ambient temperatures. All cases lie within the Continuous Maximum envelope for a cloud extent of 17.4 nmi and use a monodisperse droplet size with MVD = 20 µm, in line with previous UAV and AWE studies [20, 32]. The liquid water contents are taken from table 2.1 and summarized in table 4.1.

The wing reference geometry uses a mean chord of $c = 0.431$ m and a span of $b = 7.4$ m. A representative ground wind of $U_\infty = 10\,\mathrm{m/s}$ is assumed for exposure; a glide ratio of 5 yields an apparent inflow of $U_{\mathrm{app}} = 5\,U_\infty = 50\,\mathrm{m/s}$ for the aerodynamic scaling. The resulting chord-based Reynolds number is

$$\mathrm{Re} = \frac{U_{\mathrm{app}}\,c}{\nu} \approx \frac{50 \cdot 0.431}{1.4 \times 10^{-5}} \approx 1.54 \times 10^{6},$$

with $\nu \approx 1.4{\times}10^{-5}\ \mathrm{m^2/s}$ at near-freezing conditions. The icing exposure time follows from the Appendix C cloud extent:

$$t_{\mathrm{ice}} = \frac{17.4\ \mathrm{nmi} \times 1852\ \mathrm{m/nmi}}{U_\infty} = \frac{32224.8\ \mathrm{m}}{10\ \mathrm{m/s}} = 3222.5\ \mathrm{s}.$$

Table 4.1.: Meteorological icing cases for the simulation campaign (Continuous Maximum Appendix C, MVD = 20 µm).

Case	Icing regime	T_∞ [°C]	LWC [g/m^3]
C1	glaze	−2	0.591
C2	mixed	−4	0.547
C3	rime	−10	0.415

4.2. Grid Dependency Study

The spatial grid sensitivity is evaluated for the mixed-ice reference case C2 at $T_\infty = -4\,°\mathrm{C}$ using the procedure from section 3.5.1. All other icing cases use the same refinement pattern.

In the 2.5D mesh the surface spacing is controlled by a global scaling factor of the arcwise spacing function defined in section 3.3. The mean wall spacing h is computed as the average chordwise distance between neighbouring wall nodes. The three grid levels, together with the resulting aerodynamic coefficients and execution times, are summarised in table 4.2. The refinement ratio between successive levels is $r \approx 2$. Deviations derive from using the specified spacing function.

Table 4.2.: Grid levels and resulting aerodynamic coefficients for the mixed-ice case C2.

Level	h [–]	C_L [–]	C_D [–]	Runtime [s]
Fine	4.0×10^{-4}	0.3648	0.01887	813
Medium	8.0×10^{-4}	0.3677	0.01886	528
Coarse	1.6×10^{-3}	0.3701	0.01888	359

The lift coefficient increases slightly with grid spacing; the relative change between the fine and coarse grid is about 1.5 %. The drag coefficient remains almost constant and varies by less than 0.1 % across the three levels. The trends are shown in figures 4.1a and 4.1b. The markers indicate the discrete simulation results ϕ_i, while the red dashed line marks the formally extrapolated value ϕ_{ext} obtained from the triad analysis.

A formal Richardson extrapolation does not yield a robust estimate: the lift coefficients do not exhibit a clear asymptotic range and the drag sequence is nearly flat with slight non-monotonicity. For this reason the GCI is not interpreted quantitatively here. Instead, the grid sensitivity is assessed based on the relative changes between the three levels.

From fine to coarse, C_L changes by about 1.5 %, while C_D varies by less than 0.1 %. These differences are small compared to the expected modelling uncertainties from turbulence closure and icing physics. At the same time, the medium grid reduces the runtime to roughly 65 % of the fine grid, whereas further coarsening yields only a moderate additional speed-up. The medium grid is therefore used for all subsequent clean and iced simulations as a compromise between numerical accuracy and computational cost.

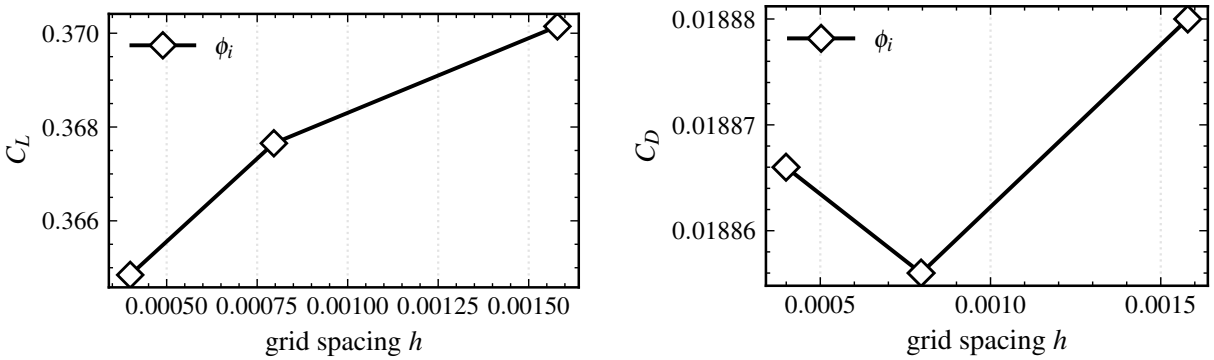

(a) C_L over mean wall spacing h.

(b) C_D over mean wall spacing h.

Figure 4.1.: Grid convergence study for the mixed-ice reference case at $T_\infty = -4°\mathrm{C}$.

The effect of the refinement on the local mesh resolution is illustrated in figure 4.2. The plots show the clean leading-edge region of the 2.5D mesh for the fine, medium and coarse grids. The prism layers and the O-grid structure are preserved. Only the chordwise spacing is coarsened from F to C.

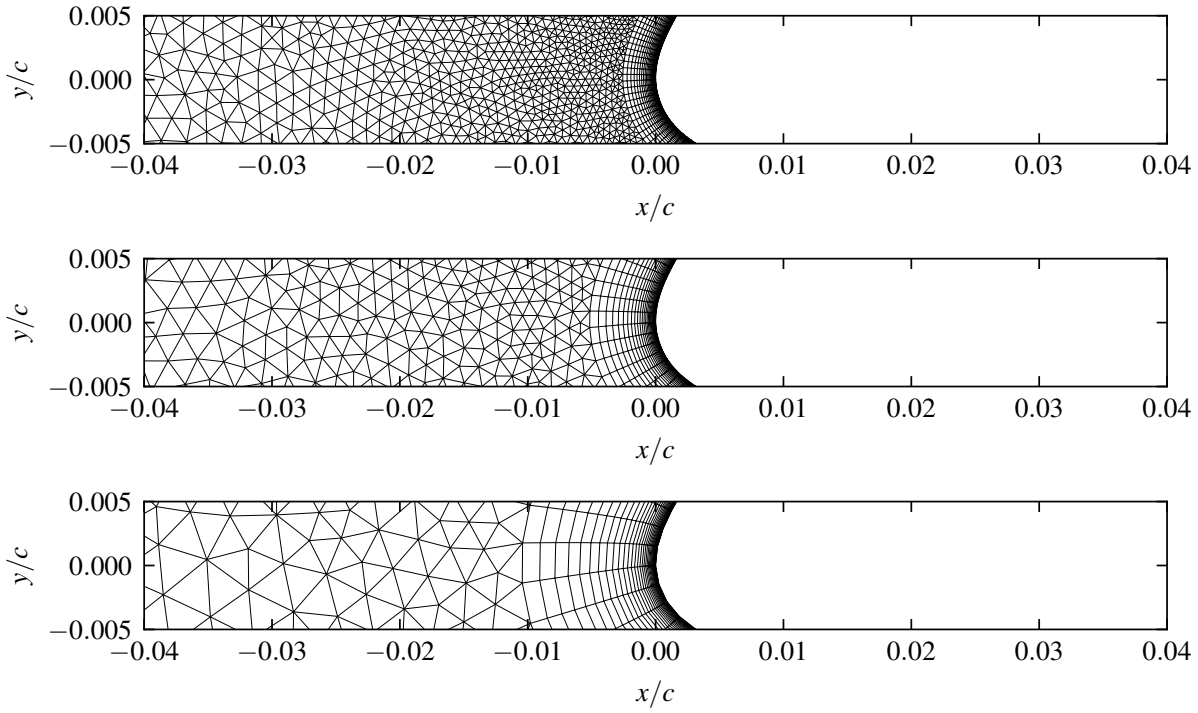

Figure 4.2.: LE-detail for selected grid refinements. Top to bottom: Fine (F), Medium (M), Coarse (C)

4.3. Time Step Study

In addition to the grid dependency study, a time step study is performed to verify that the multishot icing results are sufficiently independent of the temporal discretisation. The analysis follows the procedure outlined for the temporal convergence assessment, using lift and drag coefficients after a fixed total icing time as quantities of interest.

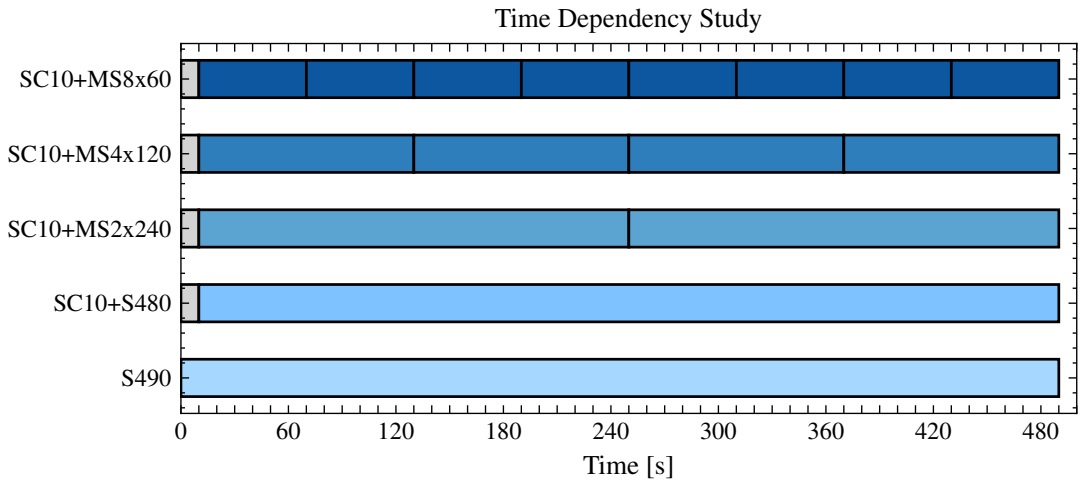

Figure 4.3.: Shot sequences for glaze (C1) Grey segments: surface-conditioning shot (SC), blue segments: icing shots (MS)

Figure 4.3 summarises the shot sequences investigated for the glaze-ice reference case C1. All configurations share the same total icing time of 490 s, but differ in the number and duration of the individual icing shots. Following the approach of Hann, Fajt and Henzler [20, 32, 33], a short initial burst is used to improve the early-stage ice accretion. In the present work this burst is implemented as a 10 s surface-conditioning (SC) shot, followed by one or several main shots (MS). For example, the notation `SC10+MS4x120` denotes one 10 s conditioning shot and four main shots of 120 s each.

Starting from a single continuous shot of 490 s (`S490`), the study first compares this baseline to a conditioned case with one main shot (`SC10+S480`) and, finally, to three refined multishot discretisations: `SC10+MS2x240`, `SC10+MS4x120` and `SC10+MS8x60`. For the temporal convergence analysis, the three finest schemes (`SC10+MS2x240`, `SC10+MS4x120`, `SC10+MS8x60`) form the time-step triplet.

Table 4.3.: Simulation results from the time step study (glaze-ice case C1).

Setup	Δt [s]	C_L	C_D
SC10+MS8x60	60	0.40210	0.01535
SC10+MS4x120	120	0.40070	0.01502
SC10+MS2x240	240	0.40219	0.01428

The resulting lift and drag coefficients are listed in Table 4.3. Each value is obtained by averaging the last 15 samples of the respective shot to suppress residual oscillations. Across the three finest time steps the lift coefficient varies by less than 0.4 %, while the drag coefficient decreases by about 2 % between $\Delta t = 60$ s and $\Delta t = 120$ s. The full trend is shown in Figure 4.4, where the coefficients are plotted as a function of the icing time step Δt on a linear scale.

Table 4.4.: Temporal convergence study for the drag coefficient C_D.

Quantity	p	$C_{D,\text{ext}}$	GCI_{21} [%]	GCI_{32} [%]
C_L	n/a	n/a	n/a	n/a
C_D	1.165	0.015616	1.730	3.965

Using the three-level refinement with a ratio of $A = 2$, a modified grid convergence analysis in time is carried out. Because the lift coefficient does not converge monotonically, the Richardson extrapolation is applied only to the drag coefficient. The extrapolated value and the corresponding temporal GCIs are summarised in Table 4.4. The observed order of convergence is $p \approx 1.17$, with an extrapolated drag coefficient of $C_{D,\text{ext}} = 0.01562$. The GCIs amount to $\text{GCI}_{21} \approx 1.7\,\%$ and $\text{GCI}_{32} \approx 4.0\,\%$, which is small compared to the expected modelling uncertainties from turbulence closure and icing physics.

The impact of the time step on the geometry is illustrated in Figure 4.5. The contour overlay in Figure 4.5 shows that the ice shapes for $\Delta t = 120\,\text{s}$ and $\Delta t = 60\,\text{s}$ are almost indistinguishable, while the solution at $\Delta t = 240\,\text{s}$ exhibits only minor deviations near the horn region.

Based on these observations, `SC10+MS4x120` is selected as the reference temporal discretisation for the subsequent multishot icing simulations. It offers a balance between numerical accuracy and computational cost and keeps the temporal discretisation error in the drag coefficient at the level of a few percent.

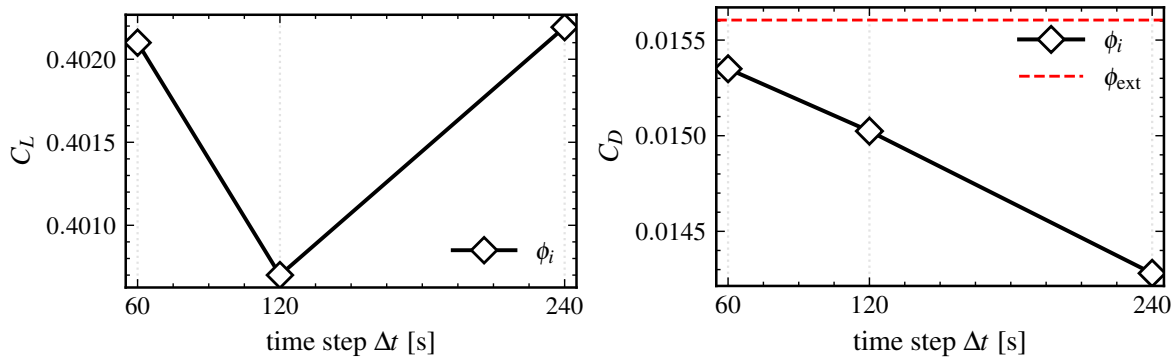

Figure 4.4.: Adapted grid-convergence study in time for the glaze-ice reference case C1: lift (left) and drag (right) coefficient as a function of icing time step Δt.

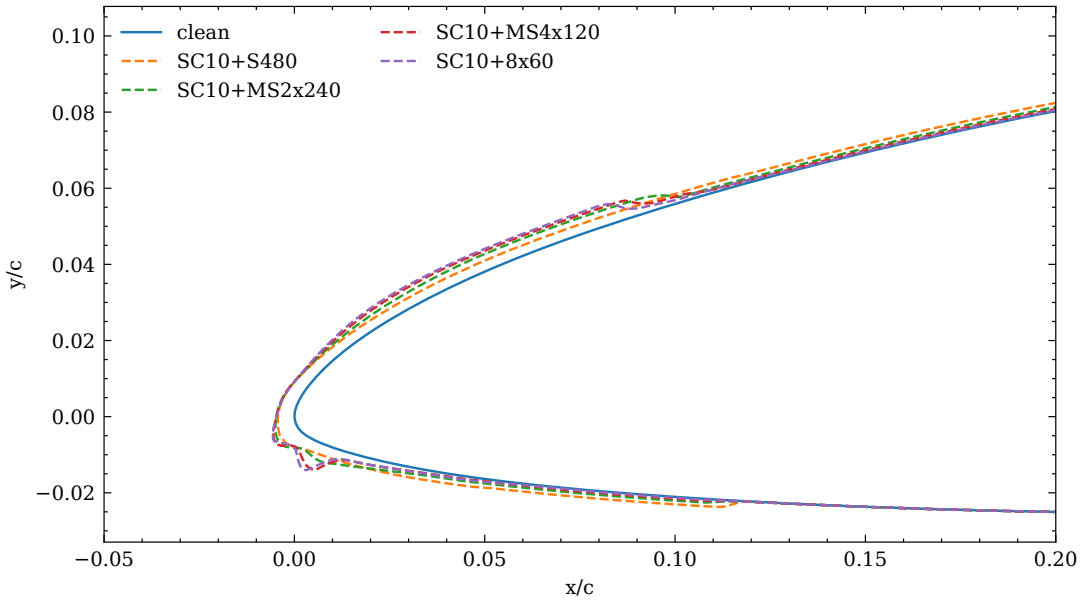

Figure 4.5.: Overlay of the final ice shapes for the different time-step discretisations (glaze-ice case C1).

4.4. Ice accretion

This section presents the resulting ice growth for the selected icing scenarios calculated with the multishot setup. The ice accretion has been post-processed for the individual steps, so that the evolution and impact of ice growth over time can be portrayed. These results include an overlay of the different icing geometries, their corresponding distribution over the arc-wise parameterization of the airfoil, their pressure coefficient distribution, their lift- and drag coefficients. Starting with the glaze ice shape displayed in figure 4.6. As seen, the ice shape starts developing horns at roughly a third of the simulation time. For this simulation a shot size of 128.5 s and a surface conditioning shot of about 10s. The uneven time step has been selected to not exceed the shot number of 25, to ensure The resulting icing time matches the targeted continuous maximum icing scenario with about 3222.5 s. The multishot simulations were performed at an AOA of $\alpha = 0\,\text{deg}$.

4.4.1. Glaze Ice

All length scales are normalized by the clean chord $c = 0.431\,\text{m}$. Figure 4.6 summarizes the multishot evolution: two horn-like protrusions form at the leading edge, with a dominant lower horn and a secondary upper horn. The horizontal reach is approximately $x/c \approx -0.05$ (lower) and $x/c \approx -0.02$ (upper). The overall glaze footprint extends to about $x/c \approx 0.10$ on the upper surface and $x/c \approx 0.05$ on the lower surface. Cumulative growth across shots is nearly linear.

The thickness distribution $t_{\text{ice}}(s/c)$ exhibits two main peaks located with the horn positions and minor bulges in between (figures 4.7 and 4.8). In the final shot, the maximum normal thickness reaches 27.18 mm at $x/c \approx 0.0001$ (lower horn), while the upper horn attains 21.32 mm at $x/c \approx 0.0226$. Integration along the surface yields a cross-section area of $1.734 \times 10^{-3}\,\text{m}^2/\text{m}$ per meter span, corresponding to about 0.159 kg over the 0.1 m extrusion (ice density $917\,\text{kg}/\text{m}^3$). Approximately 92 % of this area resides in the near-LE region ($x/c \leq 0.1$), consistent with horn-dominated accretion.

For diagnostics, the droplet-collection efficiency β limits the near-LE impingement to $x/c \in [0.000,\ 0.038]$ (threshold $\beta > 10^{-3}$), while the freezing fraction χ in this band remains small (median 0.037, mean 0.054; 97.4 % with $\chi < 0.2$), which is characteristic for glaze with runback. Detailed β/χ curves and numerical artifacts are documented in the Appendix to avoid over-interpretation in the main text.

The observed geometry explains the aerodynamic trends discussed later: the horns thicken the LE, shift the suction peak forward, and flatten pressure recovery. These effects lower C_L at moderate angles (earlier separation) and increase C_D, reducing the power-oriented proxy $\Lambda = C_L^3/C_D^2$. Quantitative aerodynamic impacts follow in section 4.5 and are interpreted at system level in chapter 5.

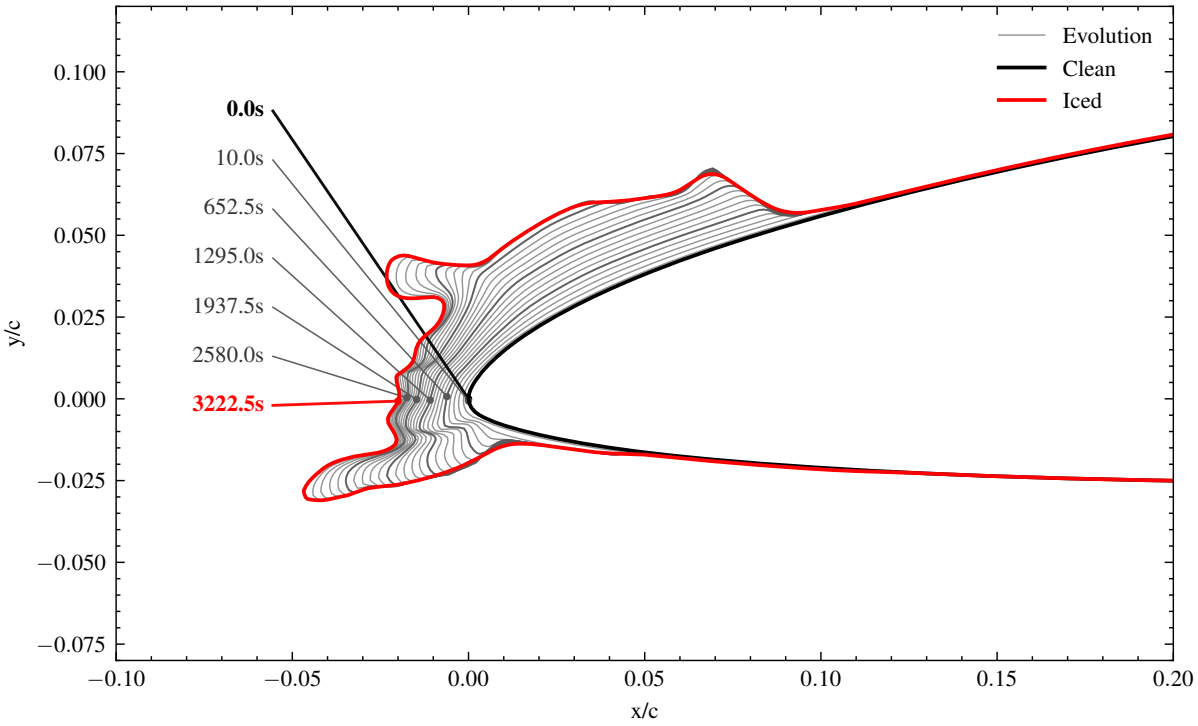

Figure 4.6.: Glaze accretion: multishot shape evolution (overlay of contours).

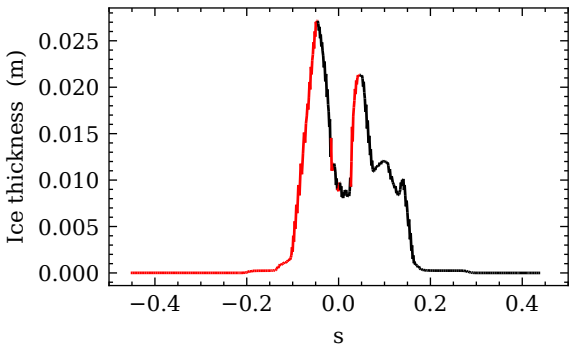

Figure 4.7.: Glaze ice thickness t_{ice} over s/c (full viewport).

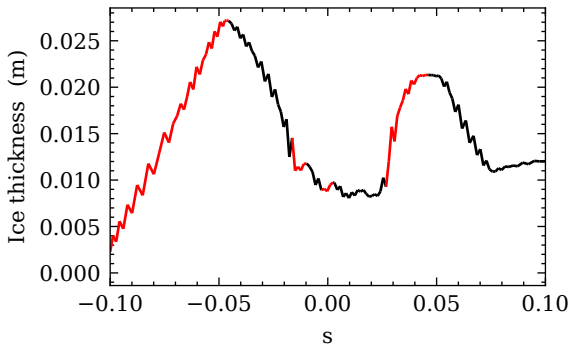

Figure 4.8.: Glaze ice thickness t_{ice} over s/c (zoom near LE).

The signed wall–shear–stress map in figure 4.9 serves as a separation indicator. Negative values are hatched and mark separated flow along the iced leading edge and grow with accretion, first appearing locally near the lower horn and later extending into the upper-side footprint. The spacetime pattern is consistent with the horn-induced forward shift of the suction peak and the flattened pressure recovery discussed for the iced polars. Mach and Pressure field can be found in figure A.15 and figure A.16 for further inspection of the separation bubbles.

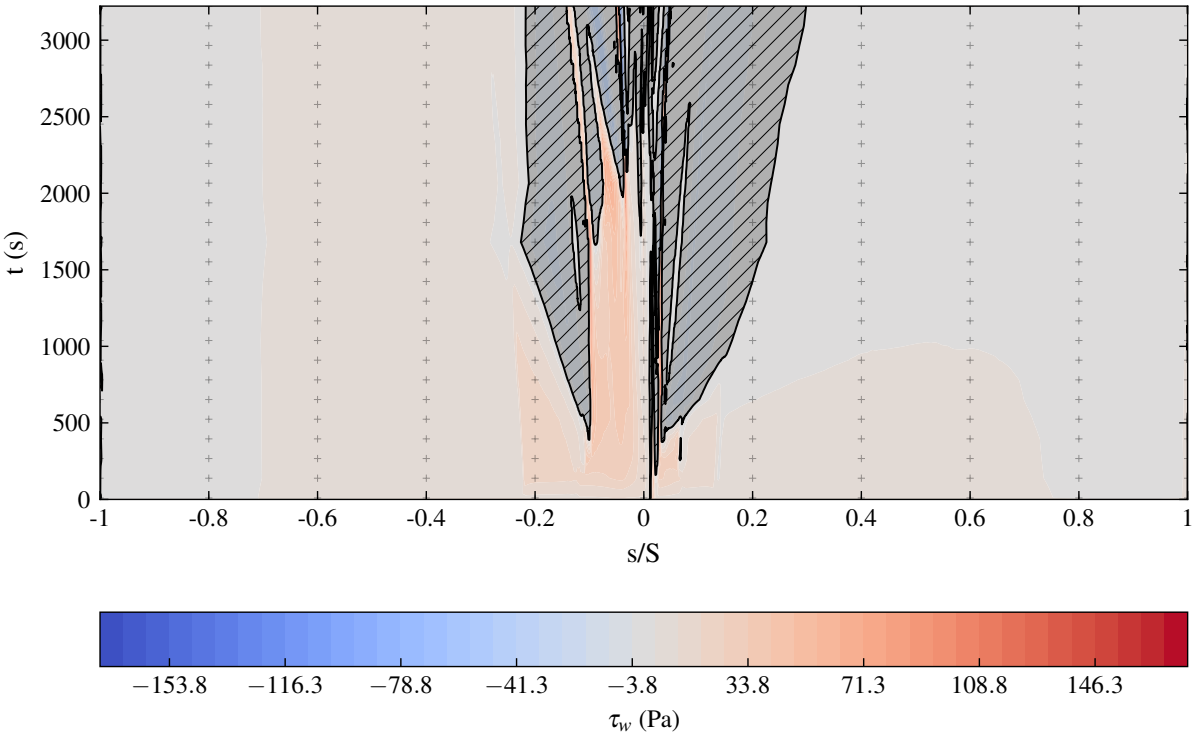

Figure 4.9.: Signed wall shear stress over s/c and time; negative regions indicate separation.

4.4.2. Mixed Ice

All length scales are normalized by the clean chord $c = 0.431$ m. Figure 4.10 shows the multishot evolution: two pronounced leading–edge horns form with a broader footprint than in the glaze case. The cumulative accretion grows super-linearly over the shots.

The thickness distribution $t_{\text{ice}}(s/c)$ features a clear double–peak with a narrow valley in between (see figures 4.11 and 4.12). In the final shot, the maximum normal thickness reaches 48.06 mm at $x/c \approx -0.09$ (upper horn), while the lower horn attains 42.44 mm at $x/c \approx -0.09$. Integrating t_{ice} along the surface yields a cross-section area of $4.535 \times 10^{-3}\,\text{m}^2/\text{m}$ per meter span, corresponding to about 0.416 kg over the 0.1 m extrusion (ice density $917\,\text{kg/m}^3$). Approximately 99.3 % of this area lies within $x/c \leq 0.1$, confirming the strongly LE-dominated character.

For diagnostics, the droplet-collection efficiency $\beta(s)$ confines the near-LE impingement to $x/c \in [0.000, 0.0639]$ (threshold $\beta > 10^{-3}$). The freezing fraction $\chi(s)$ in this band is higher than for glaze (median 0.061, mean 0.138), yet 82.3 % of samples remain below $\chi < 0.2$, i.e., mixed behavior with partial runback. In all line plots, a color change indicates a reversal of the marching direction of x/c along the s-parametrized contour (clockwise vs. counterclockwise traversal).

The geometry explains the aerodynamic trends: the larger horns thicken the leading edge, shift the suction peak forward and flatten the pressure recovery more strongly than in glaze. This promotes earlier separation and increases profile drag, thereby reducing the Loyd factor $\Lambda = C_L^3/C_D^2$. The quantitative aerodynamic impact follows in section 4.5 and the system interpretation in chapter 5.

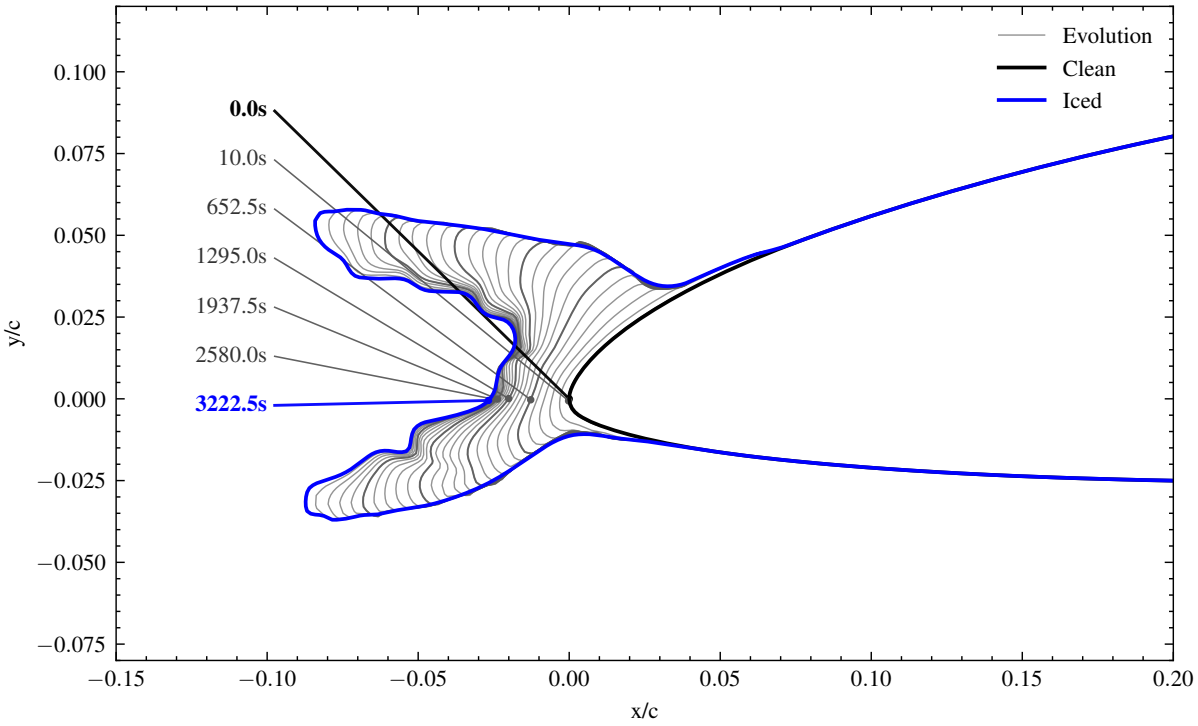

Figure 4.10.: Glaze ice shape evolution for SC10+MS25x128.5

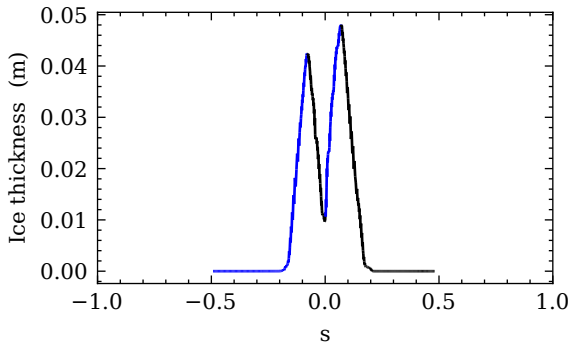

Figure 4.11.: Mixed ice — ice thickness

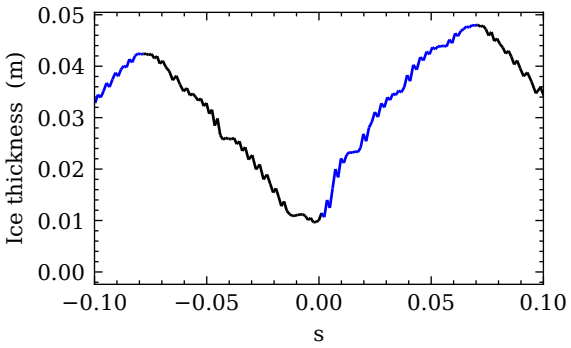

Figure 4.12.: Mixed ice — ice thickness

The signed wall–shear–stress map in figure 4.13 is used as a compact separation indicator. Hatched regions mark $\tau_w < 0$ and thus separated flow along the iced leading edge. Separation appears shortly after the initial shots and expands with ongoing accretion. The separated band widens primarily within the near-LE zone and follows the growth of the two horn structures: on the lower surface the expansion slows once the dominant horn is established, whereas on the upper surface the separated region continues to spread further into the footprint. The spacetime pattern is consistent with the forward shift of the suction peak and the flattened pressure recovery observed for mixed ice in the thickness and performance results.

Note that s is sectionally normalized by the contour length of the iced geometry. As the surface grows, the absolute s-position of the leading edge is not fixed; trends should therefore be interpreted via s/c and the extent of the negative-τ_w bands rather than by an absolute s location. Mach and Pressure field can be found in figure A.17 and figure A.18 for further inspection of the separation bubbles.

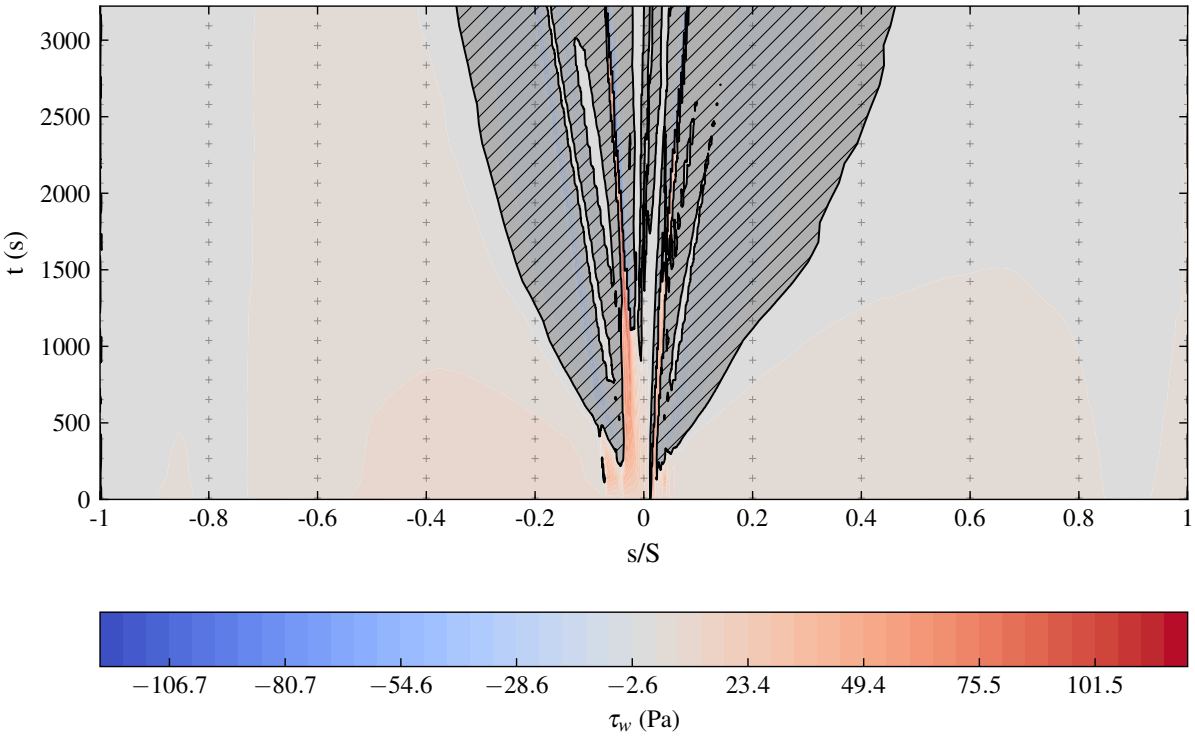

Figure 4.13.: Mixed ice — signed wall shear stress over s/S and time; hatched regions indicate $\tau_w < 0$ (separation).

4.4.3. Rime Ice

All length scales are normalized by the clean chord $c = 0.431$ m. Figure 4.14 shows the multishot evolution for rime ice. A leading–edge dominated accretion develops with one *dominant* horn at the LE and a *shorter outgrowth* on the opposite side. The growth over the shots is super-linear and remains concentrated near the leading edge.

The thickness distribution $t_{\text{ice}}(s/c)$ reflects this morphology with a pronounced peak at the dominant horn and a narrower shoulder corresponding to the outgrowth (see figures 4.15 and 4.16). In the final shot, the maximum normal thickness reaches 45.69 mm at $x/c \approx -0.1$ (dominant horn), while the upper-side outgrowth attains 31.48 mm at $x/c \approx -0.025$ but with much smaller lateral extent. Integrating t_{ice} along the surface yields a cross-section area of $3.711 \times 10^{-3}\,\text{m}^2/\text{m}$ per meter span, corresponding to about 0.340 kg over the extrusion (ice density $917\,\text{kg/m}^3$). Approximately 96.2 % of this area lies within $x/c \leq 0.1$, confirming the LE-dominated character seen in figure 4.14.

For diagnostics, the droplet-collection efficiency β confines the near-LE impingement to $x/c \in [0.000,\ 0.0502]$ (threshold $\beta > 10^{-3}$). The freezing fraction $\chi(s)$ in this band is close to unity (median 1.000, mean 0.952), i.e., nearly fully freezing, rime-typical. In all line plots, a color change indicates a reversal of the marching direction of x/c along the s-parametrized contour (clockwise vs. counterclockwise traversal). Detailed β/χ curves and numerical artifacts are collected in the Appendix.

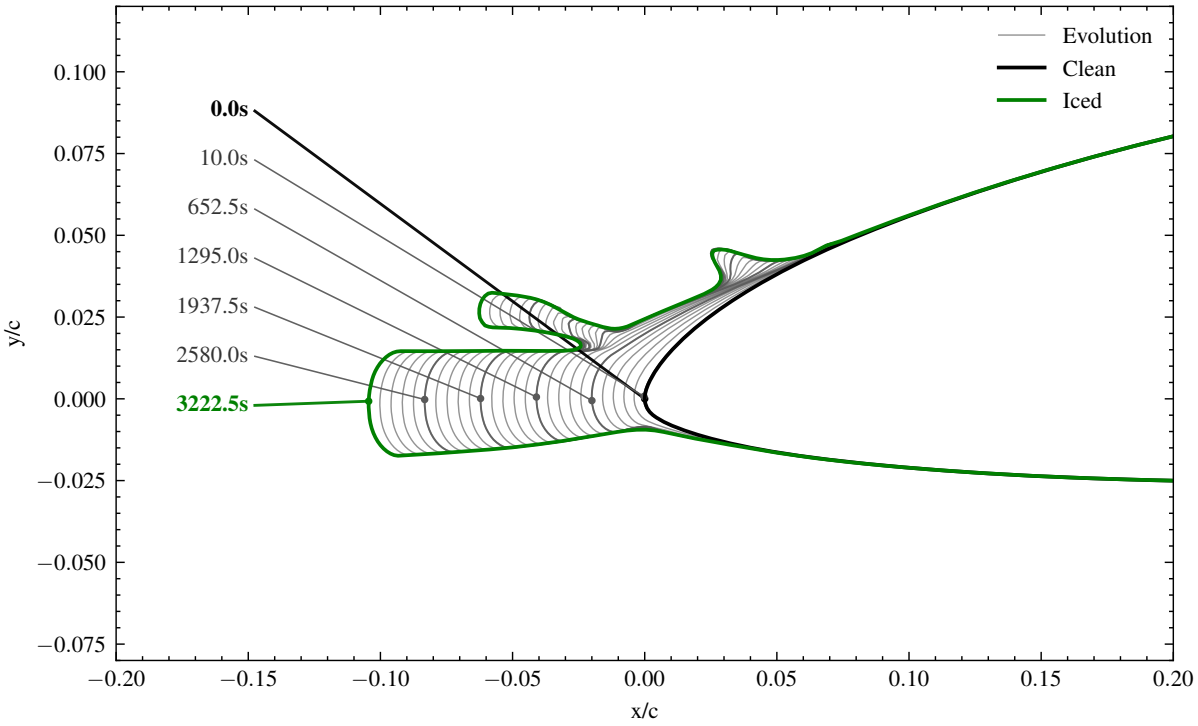

Figure 4.14.: Rime accretion: multishot shape evolution (overlay of contours).

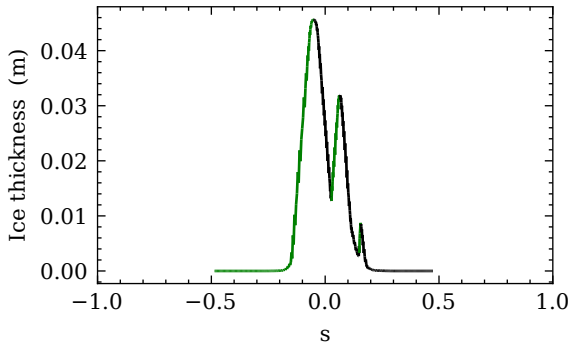

Figure 4.15.: Rime ice thickness t_{ice} over s/c (full viewport).

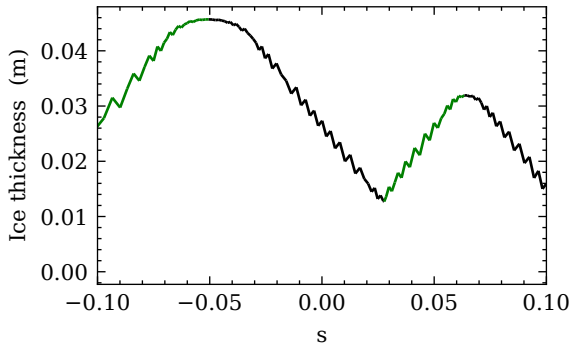

Figure 4.16.: Rime ice thickness t_{ice} over s/c (zoom near LE).

The signed wall–shear–stress map in figure 4.17 is used as a separation indicator; hatched regions mark $\tau_w < 0$. Separation emerges early in the near-LE zone and remains around $s/c \approx 0$, tracking the central horn and its shorter outgrowth. The separated band widens during the first part of the sequence and then saturates; thin unhatched streaks within the hatched area indicate intermittent reattachment. Compared with glaze and mixed, the negative-τ_w footprint is shorter in s/c and less persistent downstream, consistent with the more compact geometry seen in figure 4.14 and the thickness maps in figures 4.15 and 4.16. Mach and Pressure field can be found in figure A.19 and figure A.20 for further inspection of the separation bubbles.

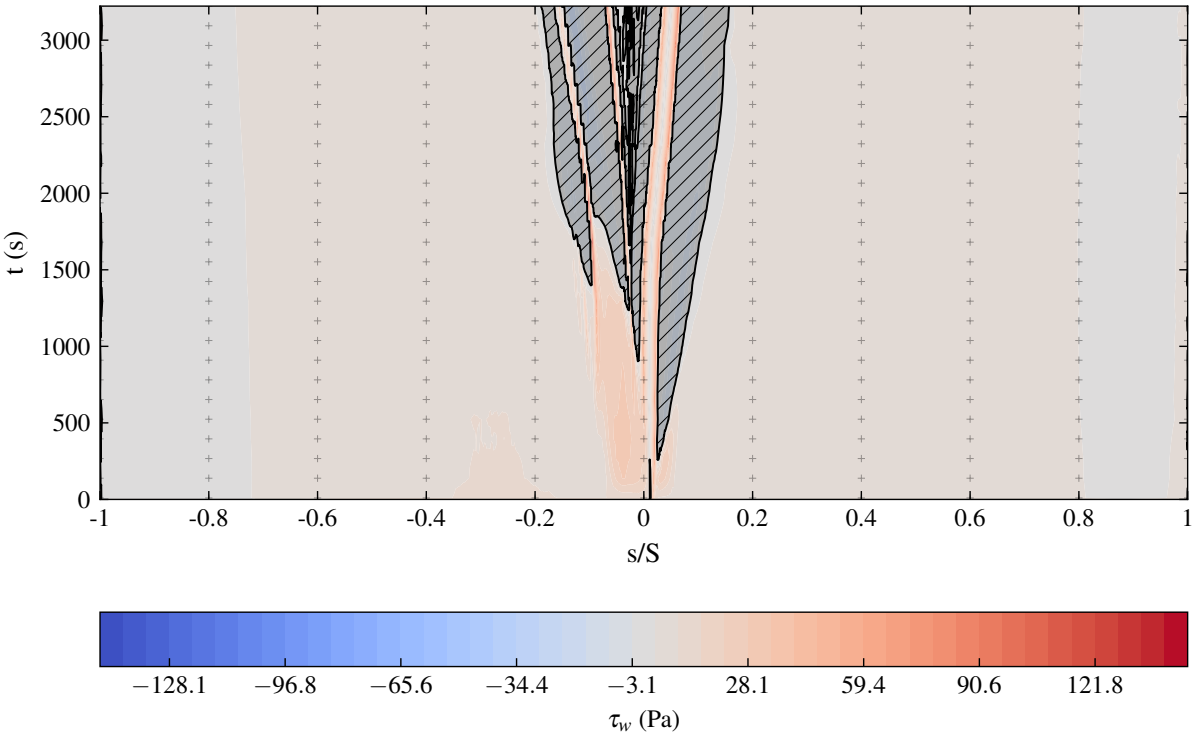

Figure 4.17.: Rime ice — signed wall shear stress over s/S and time; hatched regions indicate $\tau_w < 0$ (separation).

4.5. Aerodynamic Performance

4.5.1. Suction curve

Inspection of the pressure coefficient distribution for all icing cases shows clear changes in the suction-side loading compared to the clean reference. figure 4.18 presents the final chordwise pressure coefficient C_p along the normalized contour coordinate s/c for the clean airfoil (black) and for the glaze, mixed and rime configurations (red, blue and green). The leading edge of the clean geometry is located at $s/c = 0$.

For the clean configuration, the global suction minimum is approximately $C_{p,\text{min,global}} \approx -0.70$ at $s/c \approx 0.38$ on the upper surface. A similar value is reached in the immediate leading-edge region, which forms a smooth suction peak near $s/c = 0$. Downstream of the minimum, the clean curve shows a gradual and almost monotonic pressure recovery towards the trailing edge.

All iced configurations exhibit a stronger and forward-shifted suction minimum near the leading edge. For rime ice, the minimum reaches $C_{p,\text{min,LE}} \approx -1.04$ at $s/c \approx -0.10$. Glaze ice attains the deepest suction level with $C_{p,\text{min,LE}} \approx -1.65$ at $s/c \approx -0.02$, while mixed ice forms an intermediate case with $C_{p,\text{min,LE}} \approx -1.34$ at $s/c \approx -0.08$. In all three cases, the suction peak is located slightly upstream of the clean leading-edge position when expressed in the normalized coordinate.

Downstream of the leading-edge region, the iced curves differ in the rate and smoothness of pressure recovery. For $s/c \geq 0.3$, the clean reference shows a smooth approach towards near-zero pressure at the trailing edge. In contrast, the iced configurations recover more slowly from their amplified leading-edge minima. Mixed ice retains the lowest pressure levels over the longest chordwise extent, followed by glaze ice, whereas rime ice approaches the clean distribution again after about $s/c \approx 0.2$. All iced curves show small oscillations of C_p near the trailing edge.

These pressure distributions form the local basis for the integrated lift, drag and pitching-moment coefficients used in the aerodynamic polars and in the AWE performance metrics presented in the following sections and chapters. A dimensionless form over the arclength of the airfoil can be found in figure A.14.

4.5.2. Lift-, Drag-, and Pitchpolars

Inspection of the aerodynamic polars shows the effect of icing on the lift and drag coefficients C_L and C_D over the angle of attack α. The results for the clean reference and the three icing cases (glaze, mixed, rime) are shown in figure 4.19. The clean configuration (black) serves as reference, while the iced cases are plotted in red (glaze), blue (mixed) and green (rime), following the same colour scheme as before.

For the lift coefficient C_L, the clean airfoil reaches a maximum of $C_{L,\max} = 1.27$ at $\alpha = 12°$. The rime case attains $C_{L,\max} = 1.02$ at $\alpha = 10°$. Glaze ice reduces the maximum lift to $C_{L,\max} = 0.61$ at $\alpha = 4.5°$, and mixed ice reaches $C_{L,\max} = 0.45$ at $\alpha = 3°$. In all iced cases, the slope of $C_L(\alpha)$ stays close to the clean reference at small angles, but the curves bend over earlier and the stall angle decreases. The usable linear range in α therefore becomes narrower from clean to rime, glaze and mixed ice.

The drag coefficient C_D increases for all iced configurations. The clean case shows a minimum of $C_{D,\min} = 0.0054$ near $\alpha = 0°$. With rime ice, the minimum rises to $C_{D,\min} = 0.0176$, approximately three times higher. Glaze ice yields $C_{D,\min} = 0.0349$, and mixed ice reaches $C_{D,\min} = 0.065$. Beyond the minimum, the $C_D(\alpha)$ curves of the iced cases increase more steeply than the clean reference. Over the entire investigated range, the iced configurations therefore combine reduced peak lift with increased drag.

These polar curves provide the basis for the aerodynamic efficiency and power-oriented metrics used in the following subsections. They represent the section-level input for assessing icing-induced performance changes of the airborne wind energy system.

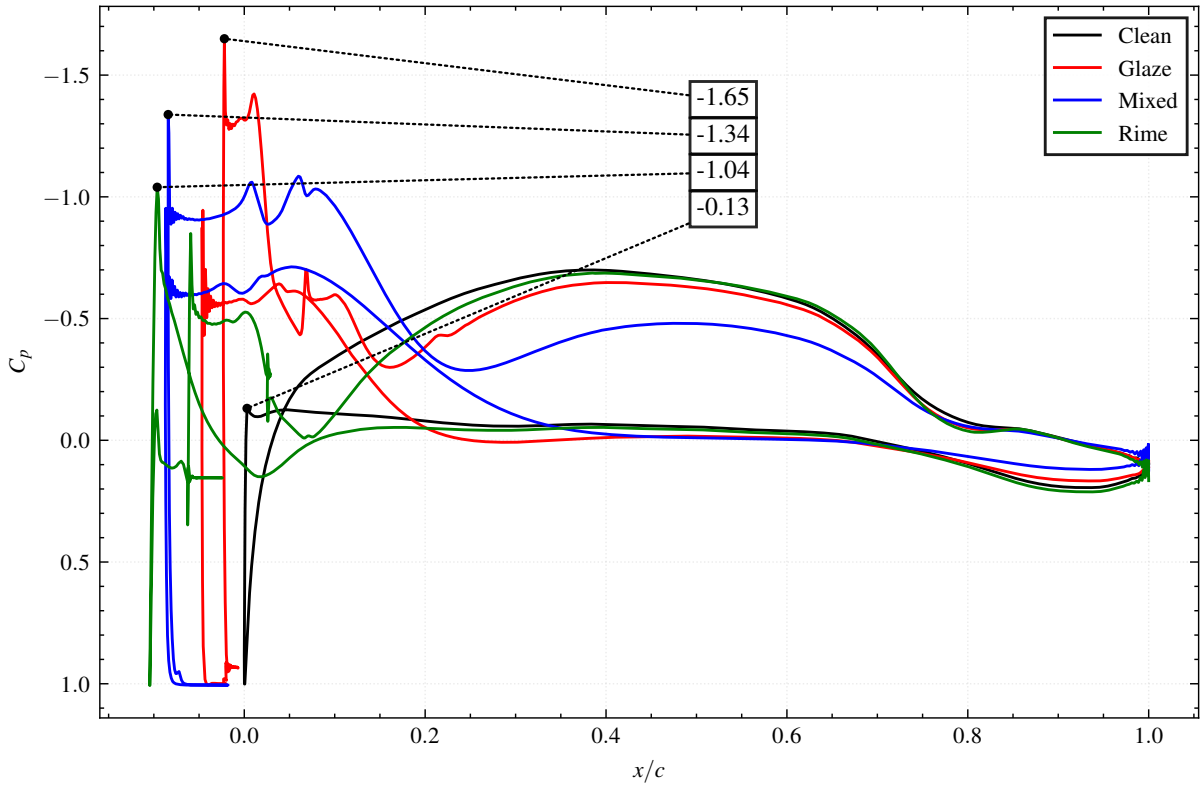

Source: Author

Figure 4.18.: Pressure Coefficient C_p over normalized chord x/c for glaze (red), mixed (blue) and rime (green) ice and the clean reference (black)

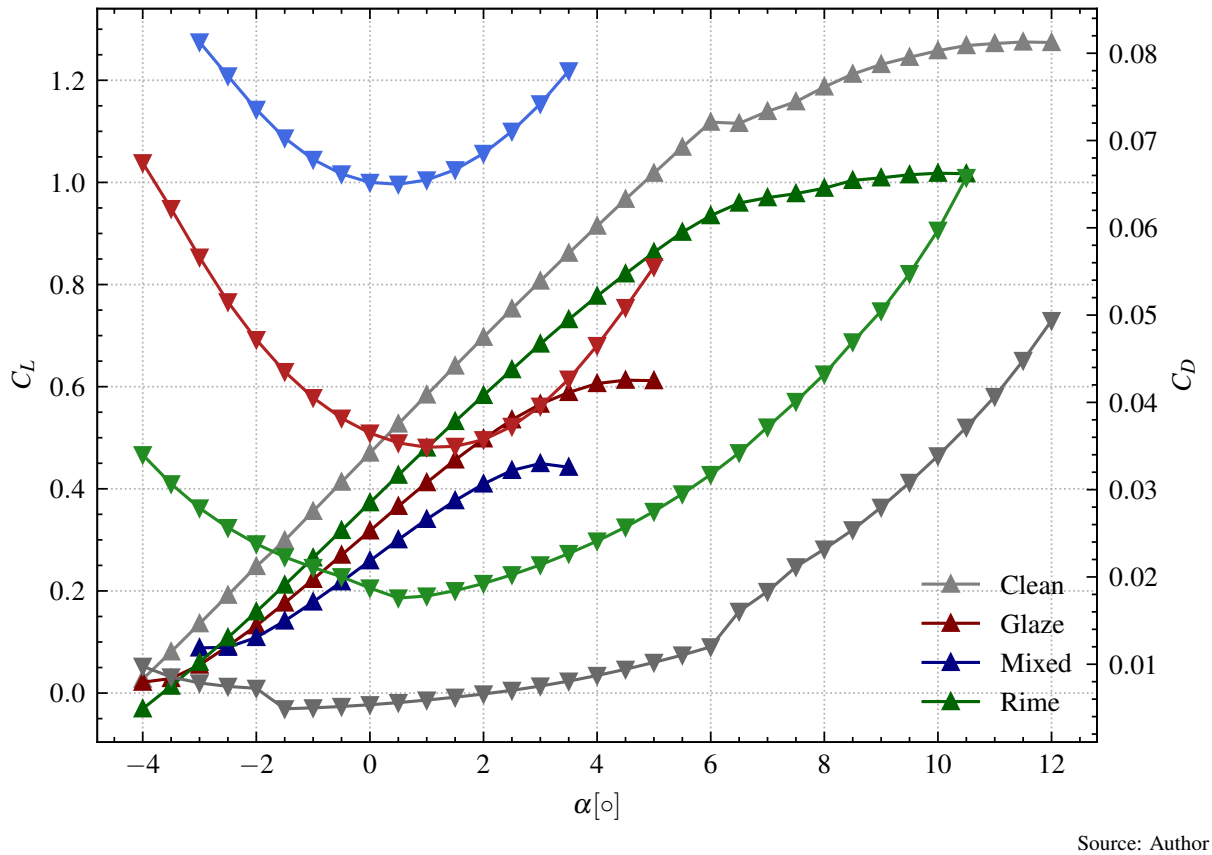

Source: Author

Figure 4.19.: Pressure Coefficient C_p over arc-length s for the normalized surface domain

The pitching-moment polars C_M are shown in figure 4.20. The horizontal axis gives the angle of attack α in degrees, and the vertical axis the nondimensional moment coefficient C_m about the fixed reference $x_{\text{ref}} = 0.25\,c$. Negative values correspond to a nose-down moment. The clean configuration is shown in black, glaze in red, mixed in blue, and rime in green.

For the clean case, the pitching moment is sampled between $\alpha = -4°$ and 12° and stays negative, with C_M between about −0.11 and −0.06. The curve shows a broad minimum near $\alpha \approx 3.5°$ and then increases slowly towards higher angles of attack.

The glaze case is evaluated from −4° to 5° and also shows only negative moments, in the range $C_M \approx [-0.088, -0.053]$. Rime ice is analysed between $\alpha = -4°$ and 10.5°; here C_m rises almost monotonically from about −0.10 to −0.04 without a zero crossing. The mixed case covers $-3° \leq \alpha \leq 3.5°$ and varies least, with C_m between roughly −0.056 and −0.038 and a very shallow minimum near $\alpha \approx -0.5°$. Overall, the pitching moment remains negative for all configurations in the investigated range, with magnitudes between about −0.11 and −0.04.

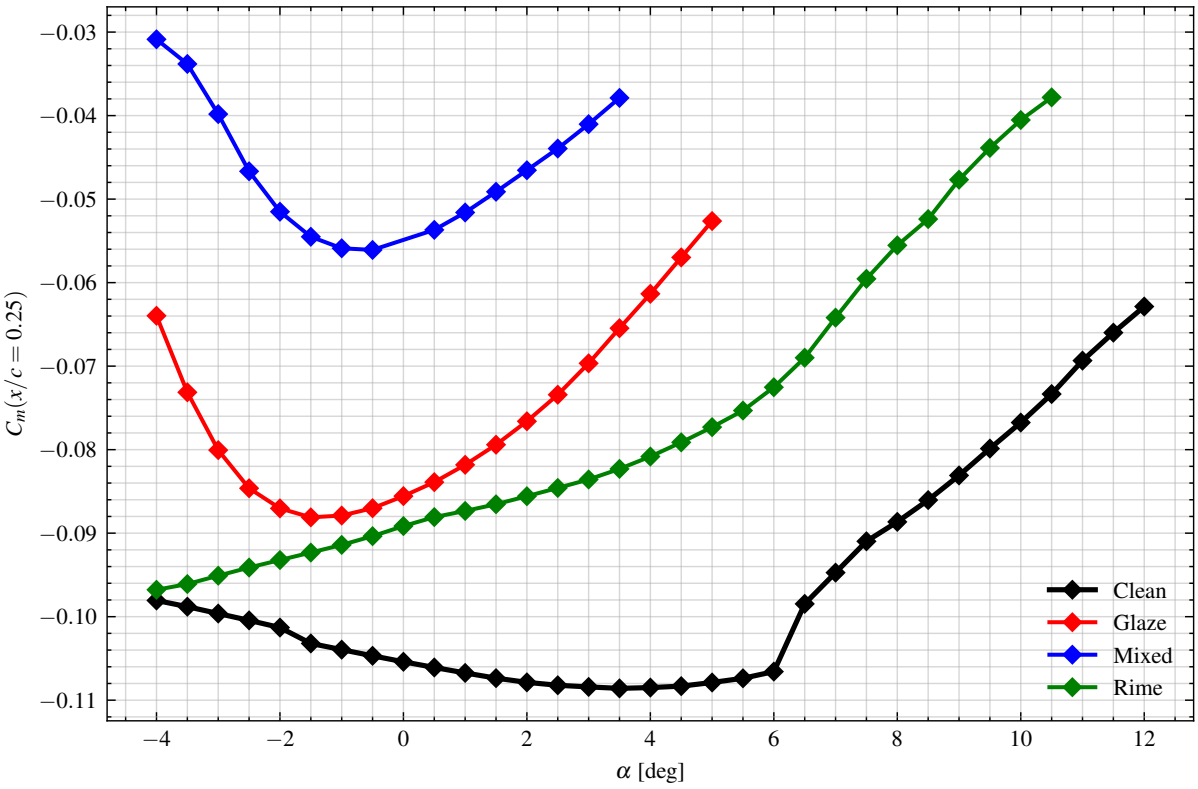

Source: Author

Figure 4.20.: Pitching-moment polars $C_m(\alpha)$ about x_{ref} for clean, glaze, mixed, and rime.

Inspection of the aerodynamic efficiency, expressed by the lift-to-drag ratio C_L/C_D, provides a direct measure of performance changes with increasing angle of attack α. The corresponding curves for the clean and iced configurations are shown in figure 4.21.

For the clean reference, the efficiency reaches a maximum of $(C_L/C_D)_{\max} = 105.7$ at $\alpha = 2°$. Among the iced cases, rime ice achieves the highest value with $(C_L/C_D)_{\max} = 32.2$ at $\alpha = 3.5°$. Glaze ice follows with $(C_L/C_D)_{\max} = 14.4$ at $\alpha = 2.5°$, while mixed ice shows the strongest reduction, reaching only $(C_L/C_D)_{\max} = 6.1$ at $\alpha = 2.5°$.

The optimal range of efficient operation therefore shifts toward smaller angles of attack for all iced configurations. In addition, the magnitude of the efficiency decreases markedly, indicating increased energy losses through drag. This trend becomes more pronounced for glaze and mixed ice, which show

both early stall behavior and a steep decline in efficiency beyond the optimum. Rime ice retains the broadest and smoothest efficiency profile, confirming its less severe aerodynamic impact compared to the other icing cases.

4.5.3. Power- and operating range

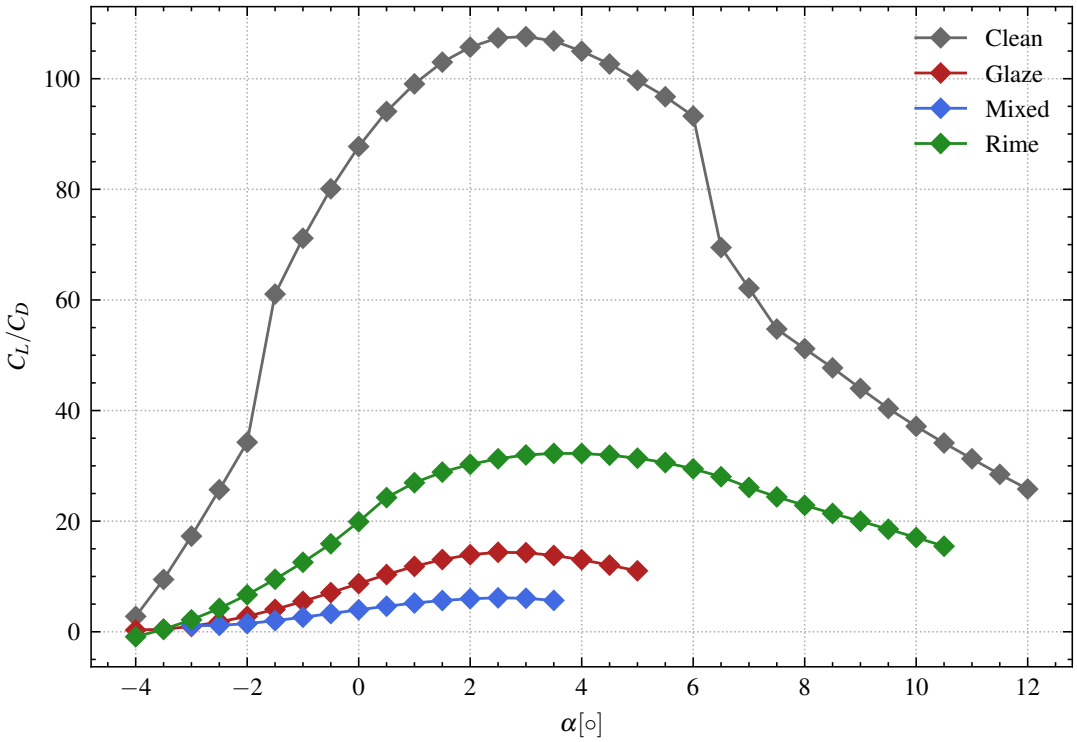

Source: Author

Figure 4.21.: C_L/C_D over AOA α

Λ extends the classical aerodynamic efficiency C_L/C_D by additionally weighting the aerodynamic lift. It is therefore not a simple amplification, but a nonlinear measure directly related to power generation potential, as both tether force and flight velocity scale with C_L. This allows a clear and direct inspection of the influence of icing on the potential power output. The gliding ratio C_L/C_D can be found in **??** in the Appendix for further reference.

For the clean configuration, the maximum value is $\Lambda_{\max} = 100.4$ at $\alpha = 4°$. Among the iced configurations, rime ice achieves $\Lambda_{\max} = 29.2$ at $\alpha = 5°$, while glaze ice reaches $\Lambda_{\max} = 10.8$ at $\alpha = 3°$, and mixed ice shows the strongest reduction with $\Lambda_{\max} = 4.1$ at $\alpha = 3°$.

Compared to the clean reference, the relative performance losses amount to approximately -71% for rime, -89% for glaze, and -96% for mixed ice. These reductions reflect the combined effect of decreased lift and increased drag caused by icing. The shift of the maximum toward smaller α indicates a narrower operational range for efficient flight conditions.

Overall, the metric Λ shows a reduction in aerodynamic efficiency for all iced configurations. The clean airfoil possesses the highest values across a wide range of angles, while glaze and mixed ice result in a sharp decrease of Λ. Rime ice shows intermediate values and less reduction.

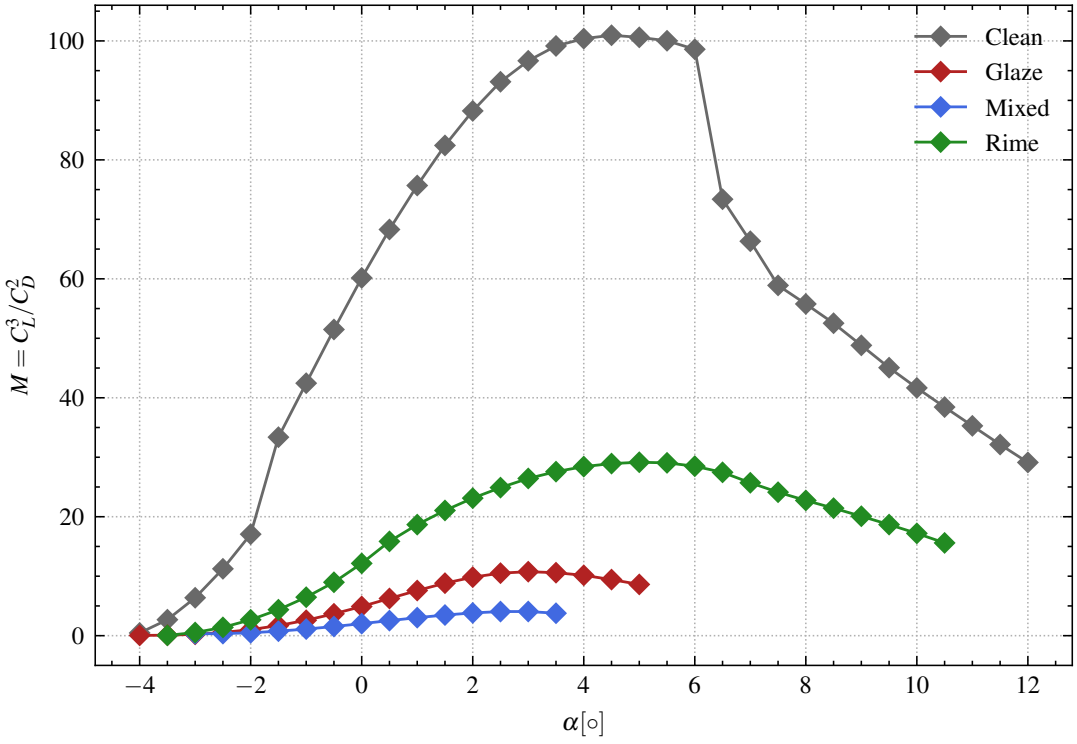

Source: Author

Figure 4.22.: Λ over α for selected icing cases: glaze (red), mixed (blue), rime(green) with clean (gray) reference

4.5.4. Temporal performance degradation

The section-level impact of icing on airborne wind energy is assessed by following the temporal evolution of the lift coefficient C_L, drag coefficient C_D, lift-to-drag ratio C_L/C_D and the Loyd factor Λ at a representative operating point. The metric Λ is defined in the background chapter in equation (2.9) and condenses the polar information into the aerodynamic input for the harvesting factor ζ introduced in section 2.1.1. Figures 4.23 and 4.24 show the corresponding time histories for the three Appendix C cases over the simulated icing duration of about 3200 s (roughly 54 min).

The first set of plots in figure 4.23 displays $C_L(t)$ and $C_D(t)$. At the beginning of the sequences, all three icing cases start from similar lift levels with $C_L \approx 0.37$. Within the first 10 s, the lift increases to about $C_L \approx 0.42$ in all configurations. Over the full exposure time, C_L stays within a relatively narrow band. For glaze ice, the values lie between roughly 0.34 and 0.42, mixed ice spans about 0.28 to 0.42, and rime ice remains in the interval $0.37 \leq C_L \leq 0.42$. In contrast, the drag coefficient increases clearly over time. The initial drag lies near $C_D \approx 0.0189$ in all three cases. The smallest values in the iced sequences are $C_D \approx 0.0105$, while the maxima reach approximately 0.0364 for glaze, 0.0653 for mixed and 0.0193 for rime ice. This corresponds to an increase by roughly a factor of 3.5 for glaze, 6.2 for mixed and 1.9 for rime relative to the lowest values in each sequence.

The combined effect on aerodynamic efficiency is visible in the C_L/C_D and Λ panels in figure 4.24. At the start of the iced runs, the lift-to-drag ratio is about $C_L/C_D \approx 19.6$ for all three configurations, which is lower than the clean reference at the same operating point. In the first time step, the efficiency improves and reaches peak values close to $C_L/C_D \approx 40$ at $t = 10$ s for glaze, mixed and rime ice. Afterwards, the curves decrease again as drag grows. At the end of the simulation, the glaze case settles at $C_L/C_D \approx 9.4$, mixed ice at about $C_L/C_D \approx 4.3$, while rime ice remains at $C_L/C_D \approx 20.5$.

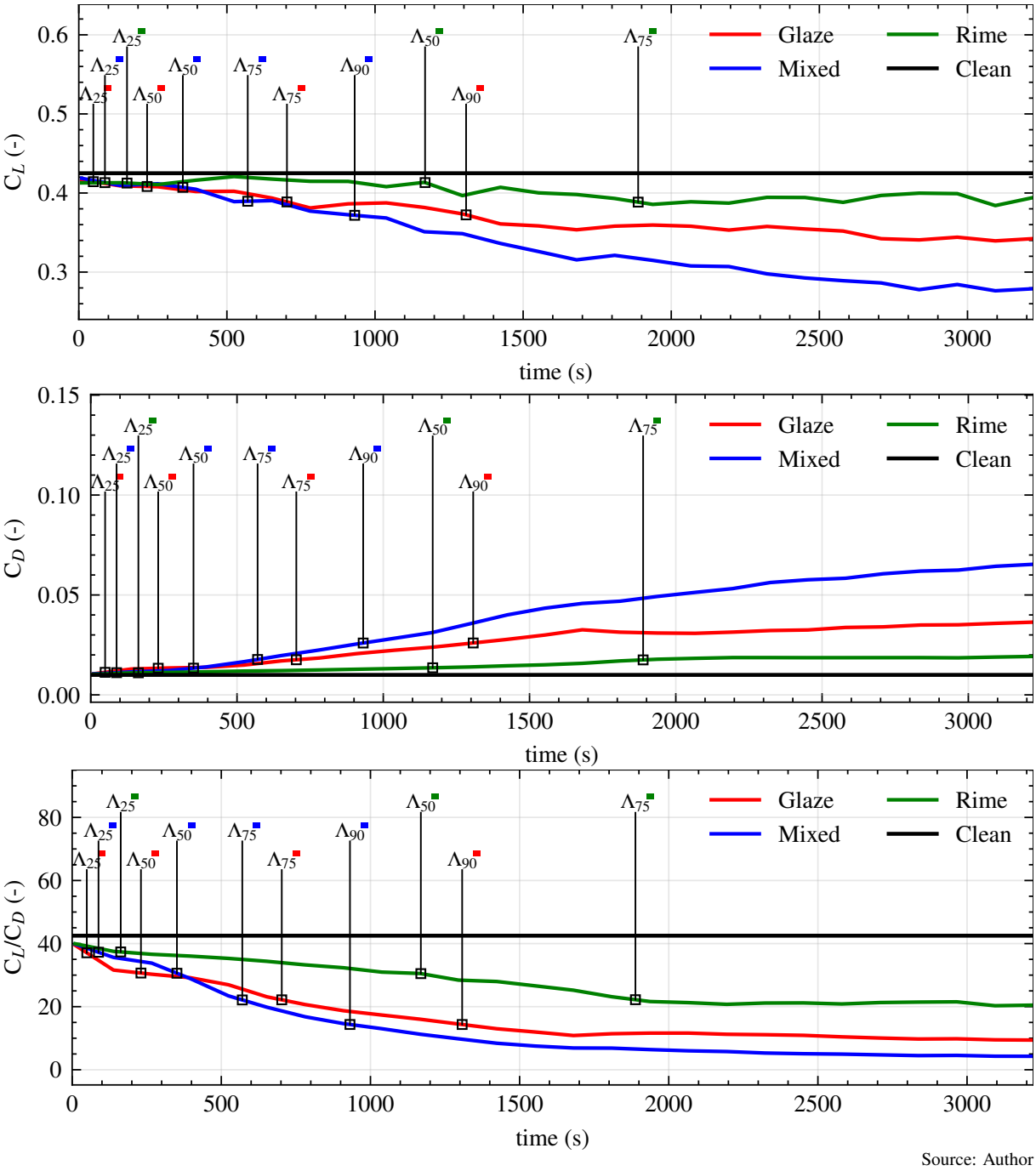

Source: Author

Figure 4.23.: Time histories of lift and drag coefficients $C_L(t)$ and $C_D(t)$ for glaze, mixed and rime ice and the clean reference at $\alpha = 0°$.

The corresponding Loyd factor $\Lambda(t)$ follows the same trend. In the first time step, all three cases reach peak values of $\Lambda \approx 650$. Towards the end of the simulation, the values differ clearly between the icing regimes. Glaze ice reduces Λ to about 30, mixed ice reaches only $\Lambda \approx 5$, whereas rime ice ends at $\Lambda \approx 165$. The main differences between the cases therefore result from the long-term drag increase, while the lift remains comparatively stable.

To relate these curves directly to the clean crosswind potential from equation (2.9), figure 4.24 also shows the normalized quantity $\Lambda_{\text{iced}}/\Lambda_{\text{clean}}$. At the beginning of the iced sequences, the three cases start at a common level of approximately 0.19, i.e. at about 19 % of the clean Loyd factor at the chosen operating

point. Within the first 10 s, the normalized performance increases to peak values between 0.84 and 0.86 for all three icing regimes. After this initial improvement, the ratios decrease again as ice accumulates.

The subsequent degradation takes place on different time scales. For glaze ice, the normalized Loyd factor drops below 0.50 after about $t \approx 270$ s (around 4.5 min) and falls below 0.25 at $t \approx 780$ s (about 13 min). The level of 0.10 is crossed at $t \approx 1420$ s (24 min), and at the end of the simulation the remaining value is $\Lambda_{\text{iced}}/\Lambda_{\text{clean}} \approx 0.04$, i.e. about 4 % of the clean section performance. Mixed ice shows an even stronger reduction. The thresholds of 0.50, 0.25 and 0.10 are first crossed at approximately $t \approx 400$ s (6.6 min), $t \approx 650$ s (10.9 min) and $t \approx 1040$ s (17.3 min). At $t = 3222.5$ s, the normalized Loyd factor has decreased to $\Lambda_{\text{iced}}/\Lambda_{\text{clean}} \approx 0.007$, i.e. to less than 1 % of the clean reference. The rime case degrades more slowly. After the peak, the ratio falls below 0.50 at about $t \approx 1295$ s (21.6 min) and below 0.25 at $t \approx 1938$ s (32.3 min). It does not reach the 0.10 level within the simulated exposure and ends at $\Lambda_{\text{iced}}/\Lambda_{\text{clean}} \approx 0.22$, corresponding to approximately 22 % of the clean section performance.

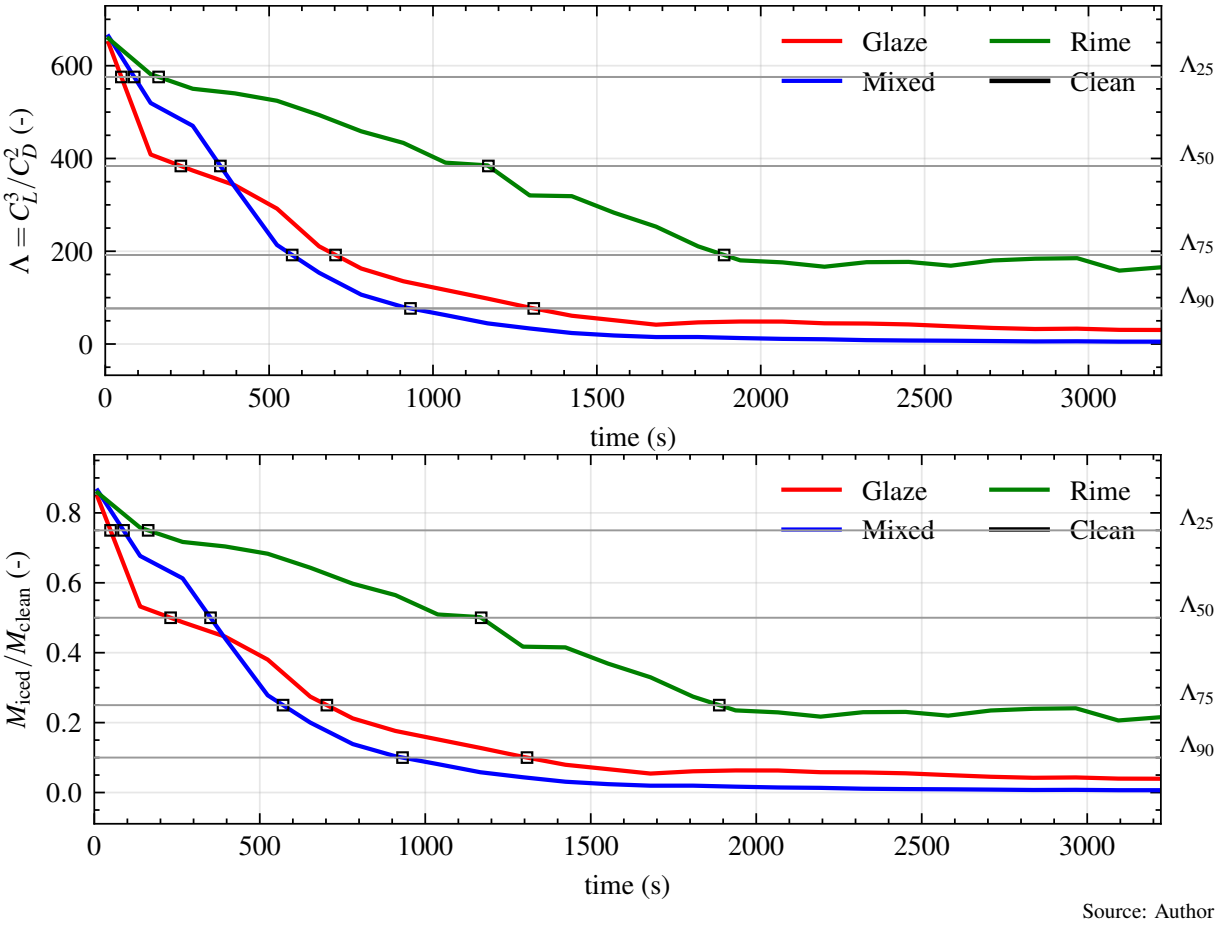

Source: Author

Figure 4.24.: Time histories of lift-to-drag ratio $(C_L/C_D)(t)$, Loyd factor $\Lambda(t)$ and normalized Loyd factor $\Lambda_{\text{iced}}/\Lambda_{\text{clean}}$ for glaze, mixed and rime ice.

The temporal curves of C_L, C_D, C_L/C_D, Λ and $\Lambda_{\text{iced}}/\Lambda_{\text{clean}}$ therefore give a direct view of how the aerodynamic power potential defined in the background chapter changes under continuous ice accretion for the three Appendix C conditions considered here. These results form the basis for the airborne-wind-energy-specific discussion in chapter 5.

5. Discussion

This chapter discusses the main findings of the simulation campaign with focus on the aerodynamic and system-level implications for AWESs. It evaluates the reliability and scope of the obtained results and places them in context with previous research. The discussion is structured into three parts. The first part interprets the aerodynamic results in terms of their implications for crosswind operation and power generation. The second part addresses the main limitations of the study and their expected influence on the results. The third part outlines possible extensions of the developed framework and future research directions for icing on AWESs.

5.1. Implications for AWES

The results show that in-flight icing strongly reduces the aerodynamic power potential of the rigid-wing, GG, crosswind AWE configuration defined in section 4.1 and the aerodynamic results in section 4.5. The discussion focuses on lift-to-drag ratio, the Loyd factor Λ and the usable AOA range.

For the clean airfoil, the maximum lift coefficient is $C_{L,\max} \approx 1.27$ at $\alpha \approx 11.5°$ with a small minimum drag of $C_{D,\min} \approx 5.4 \times 10^{-3}$. The peak of C_L/C_D and of the Loyd metric Λ, with $\Lambda = C_L^3/C_D^2$, lies at low AOA and defines a broad and efficient operating window. Under icing, $C_{L,\max}$ decreases to about 1.02 (rime), 0.61 (glaze) and 0.45 (mixed), and stall moves to smaller α. At the same time, $C_{D,\min}$ rises by more than a factor of three for rime and by more than one order of magnitude for mixed ice. As a result, both C_L/C_D and Λ are reduced over the entire relevant range, and the optimum shifts to lower angles. Clean settings near the stall angle are no longer usable once glaze or mixed ice has formed. These trends are visible in the suction curves and polars in figures 4.18, 4.21 and 4.22 and are summarised by the peak values in table 5.1.

The Loyd factor summarizes these effects. The maximum Λ of the clean airfoil drops by roughly a factor three in the rime case and by almost an order of magnitude for glaze and mixed ice. In the time-resolved multishot simulations within the CM Appendix C cloud (see figures 4.23 and 4.24), the normalized ratio $\Lambda_{\text{iced}}/\Lambda_{\text{clean}}$ remains around 0.2 for rime towards the end of the exposure, but falls below 0.1 for glaze and mixed. With fixed reeling factor and efficiency, the extracted mechanical power scales with Λ, so these reductions translate into similar losses in cycle-averaged power.

For the reference AWE system this means that operation in icing conditions requires more restrictive settings. The reduced stall margin and the left shift of the optimal AOA favour flatter loop geometries and tighter AOA limits, especially for glaze and mixed ice. Rime ice allows continued but de-rated operation, while glaze and mixed ice quickly constrain the viable operating window to a point where efficient power production is no longer realistic without mitigation. Cold, low-LWC rime conditions can be addressed with operational measures (adapted loop shape, reduced reeling speed, temporary de-rating). Warm, high-LWC glaze and mixed conditions instead point towards the need for active or hybrid Icing Protection Systems (IPSs) focused on the LE, where the horn forms and Λ is most sensitive to local shape changes. Icing thus acts as a primary driver of energy yield and must be included in AWE design and control through iced polars and time-dependent Λ, consistent with the temporal degradation shown in figure 4.24.

Table 5.1.: Absolute aerodynamic peaks as value–angle pairs (value, angle in degrees)

Case	$C_{L,\max}$	α [°]	$C_{D,\min}$	α [°]	$(C_L/C_D)_{\max}$	α [°]	$\Lambda_{\max}$	α [°]
Clean	1.275	11.5	0.004 89	−1.5	107.6	3.0	10 190.80	4.5
Glaze	0.613	4.5	0.034 86	1.0	14.4	2.5	115.74	3.0
Mixed	0.450	3.0	0.064 99	0.5	6.1	2.5	16.50	3.0
Rime	1.018	10.0	0.017 59	0.5	32.2	3.5	850.19	5.0

5.2. Limitations

The work addresses the main goal of quantifying icing penalties for a rigid-wing AWE section, but it does not cover all items of the original assignment. In particular, the analysis is restricted to a single 2D/2.5D wing section and does not include rotors, tether or a full 3D airframe simulation. The chosen scope was a compromise between numerical detail and the time and resources available for a master thesis.

Only one airfoil has been investigated. The profile is specific to the reference system and is not a standard database airfoil. This choice reduces the range of configurations covered and limits direct comparison with other studies. At the same time, it allowed a consistent treatment of geometry, meshing and icing within the developed framework. The results should therefore be seen as representative for this particular section, not as a universal description of all AWESs.

No direct validation against experimental data was carried out. Neither wind-tunnel measurements nor dedicated in-flight data were available for the airfoil. A separate validation step with a more generic airfoil and measured polars, as originally planned, could not be completed. The present setup was instead checked internally by grid and time-step studies (sections 4.2 and 4.3) and by comparing trends to published icing literature. This reduces confidence in absolute values but still supports the ordering of the cases and the relative changes in the Loyd factor.

Rotors, tether and the 3D airframe were not simulated. Their inclusion would require separate meshing strategies, moving geometries and significantly higher computational cost. For this thesis, the effort was focused on building a robust 2D/2.5D pipeline with CFD and icing, as used in the simulation campaign (sections 4.4 and 4.5), and on analyzing the aerodynamics of the most critical lifting surface. As a consequence, effects such as spanwise variation of ice and icing behaviour of the tether are outside the present scope.

The icing parameter space is also limited. Only three Appendix C conditions with fixed MVD and LWC were considered at one Reynolds number, as summarised in table 4.1. Other meteorological regimes, such as SLD icing or intermittent exposure, are not addressed. Different choices here might change the relative severity of the cases.

Within these boundaries, the results in chapter 4 should be read as a first, but consistent, step towards understanding icing effects on AWESs. They provide a basis that can be extended towards more generic airfoils, 3D geometries and validated setups in future work.

5.2.1. Outlook

The present framework provides a first step towards icing analysis of rigid-wing AWESs.A direct next step is to apply the pipeline to a small set of additional airfoils that are more common in the literature. This would improve comparability to existing data and help separate effects of geometry from effects of meteorology. In parallel, the icing parameter space could be enlarged by varying LWC, MVD and exposure time and by including representative SLD conditions.

A second direction is the move from 2D/2.5D to 3D. Simulations of the full wing with spanwise variation in angle of attack and local flow would allow the study of icing patterns along the span. Adding simplified versions of the tether and the static parts of the airframe would close the gap between the section-level analysis and the complete AWE device. Due to the higher numerical cost, such studies will likely focus on shorter icing times or on smaller simulated segments.

Experimental validation remains an important open point. An approach is to choose a standard airfoil such as RG15 [20] with available wind-tunnel data for clean and iced conditions and to repeat the present workflow for the published test matrix. This would help to estimate model and setup errors and to calibrate selected icing parameters. Smaller-scale measurements, for example of local ice thickness or pressure distributions, could also be used to check individual parts of the simulation chain.

Finally, the aerodynamic and icing results should be coupled more tightly to system-level models. Using time-dependent Λ in crosswind power calculations (based on the time histories in figure 4.24), simple flight mechanics and control models would link the section-level degradation directly to loss of annual energy production and Levelized Cost of Energy (LCoE). On this basis, different IPSs and operational strategies could be assessed quantitatively and compared with purely aerodynamic design changes. This would support the design of AWESs that remain operational and economically viable in cold and icing-prone environments.

5.3. Conclusion

This thesis investigated icing-induced performance losses for rigid-wing AWESs and developed a numerical framework to generate iced aerodynamic polars for use in scaling and dimensioning studies. A modular FENSAP-based pipeline was assembled, from geometry and mesh generation to droplet tracking, ice accretion and aerodynamic post-processing. The workflow was applied to a KM1-inspired airfoil section under three CM icing cases (glaze, mixed and rime) and the results were condensed into lift, drag, pitching moment and the Λ metric to link section aerodynamics to crosswind power.

The simulations show that icing on a AWE-relevant section produces distinct and persistent morphologies. Glaze and mixed ice form pronounced horns on the suction side and locally sharp features near the LE, while rime ice remains smoother and more conformal to the clean profile. These differences arise from the droplet collection and freezing behaviour and lead to different long-term drag growth and surface pressure distributions.

At the chosen operating point, the clean configuration reaches a Λ value of about $\Lambda \approx 650$. All three icing regimes exhibit a short initial phase in which Λ increases, driven by locally higher suction at the modified LE. This phase lasts only a few seconds. With continued accretion, Λ decreases strongly. For glaze ice, the normalized metric drops to $\Lambda_{\text{iced}}/\Lambda_{\text{clean}} \approx 0.04$. Mixed ice is even more penalizing and reaches about 0.007. Rime ice remains less severe but still reduces the metric to roughly 0.22 at the end of the simulated exposure. In all cases, the dominant penalty stems from drag growth; lift stays comparatively stable and stall onset shifts only moderately. The usable operating range in terms of angle of attack and Λ therefore contracts, even before classical stall.

For rigid-wing AWESs, these findings imply that sustained operation in mixed or glaze conditions would almost remove the crosswind power potential within tens of minutes, while even rime ice leads to marked reductions in Λ and reduced aerodynamic margins. Icing cannot be treated as a secondary effect in system design and operation. The presented framework provides a reusable tool to quantify these penalties for arbitrary Selig-format airfoils and representative icing cases. It closes a gap between clean-aerodynamic sizing studies and the need for iced polars and time-resolved Λ histories. Although the current study is limited to a single section, a simplified 2.5D representation and unvalidated aerodynamic data, it establishes realistic magnitudes and time scales of icing losses for AWE applications. This forms a basis for future work on 3D wings, system-level integration and the assessment of IPSs and operational strategies for AWESs in cold and icing-prone environments.

A. Appendix

A.1. Glaze Ice

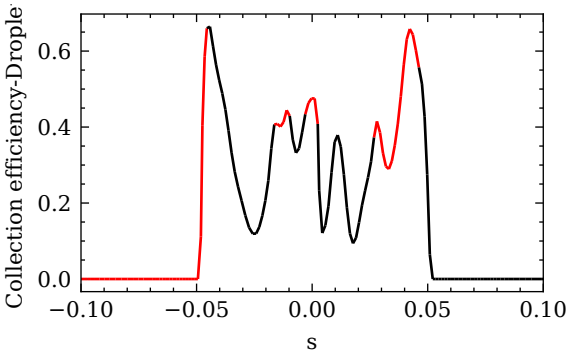

Figure A.1.: Glaze ice — collection efficiency β

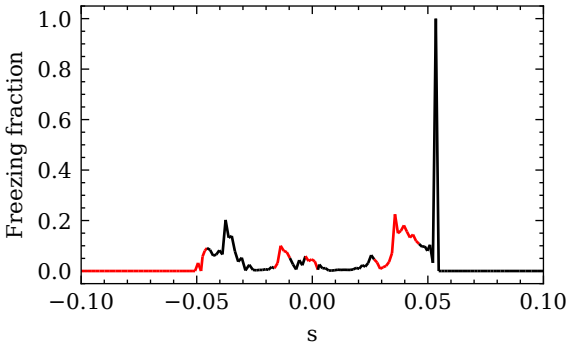

Figure A.2.: Glaze ice — freezing fraction η

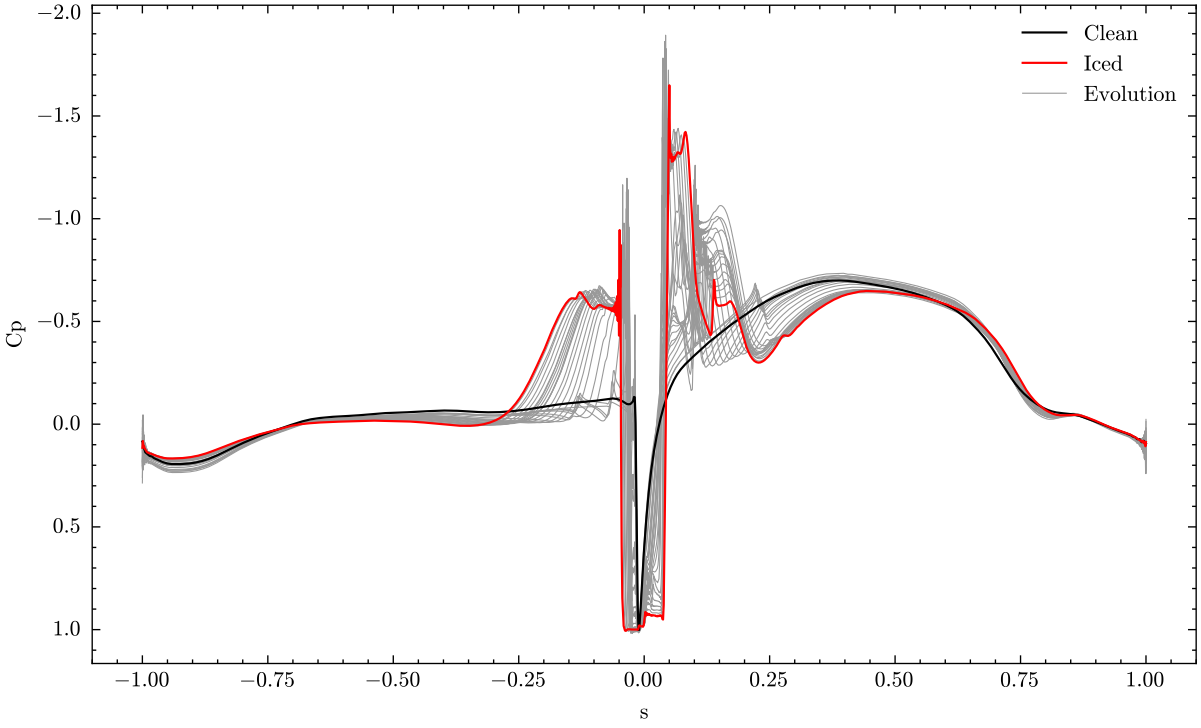

Figure A.3.: Glaze ice — pressure coefficient over arc length s

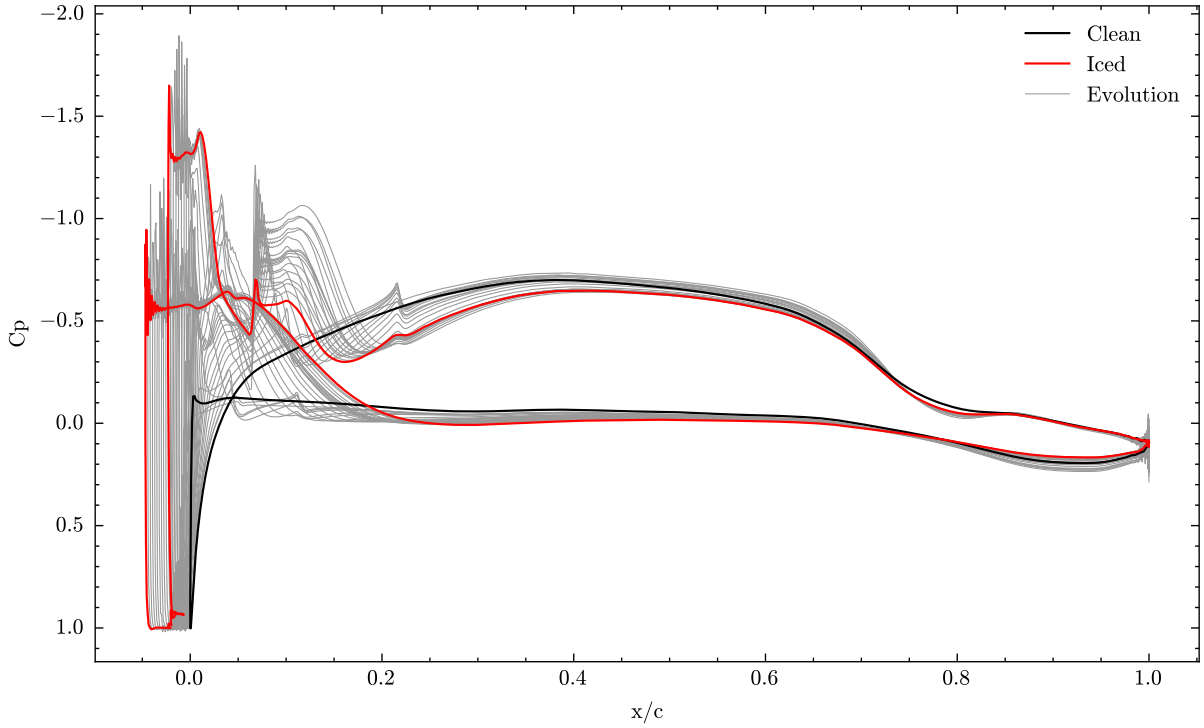

Figure A.4.: Glaze ice — pressure coefficient over dimensionless chord x/c

A.2. Mixed Ice

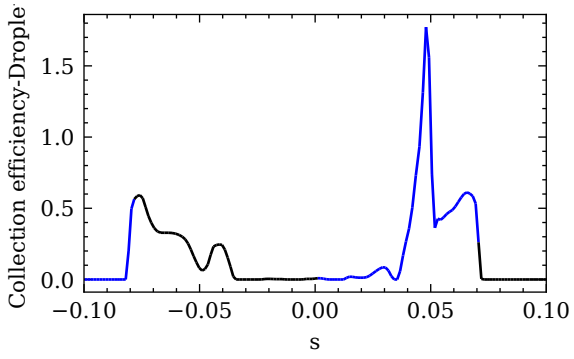

Figure A.5.: Mixed ice — collection efficiency β

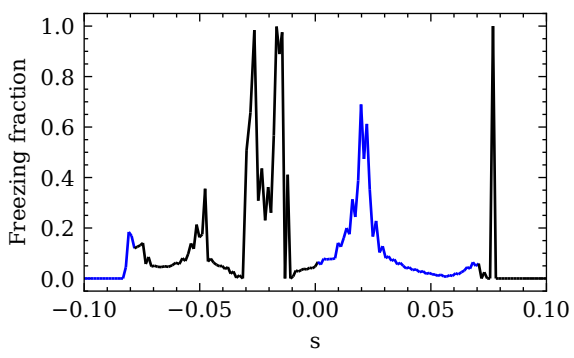

Figure A.6.: Mixed ice — freezing fraction η

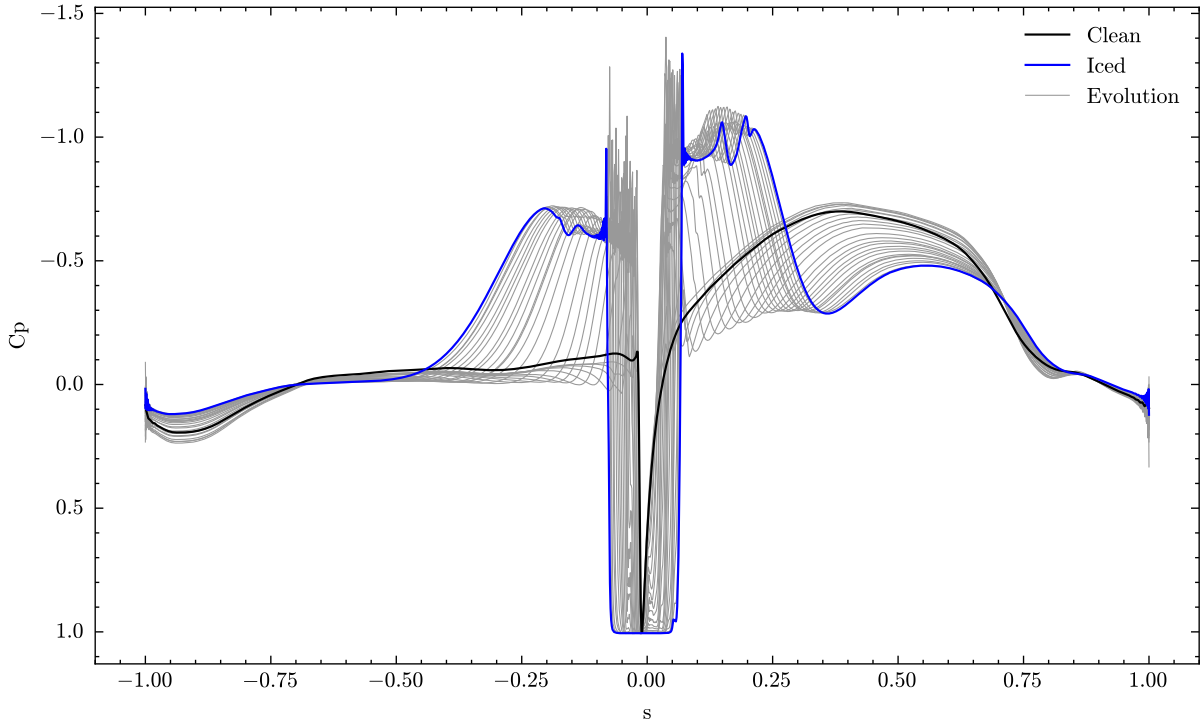

Figure A.7.: Mixed ice — pressure coefficient over arc length s

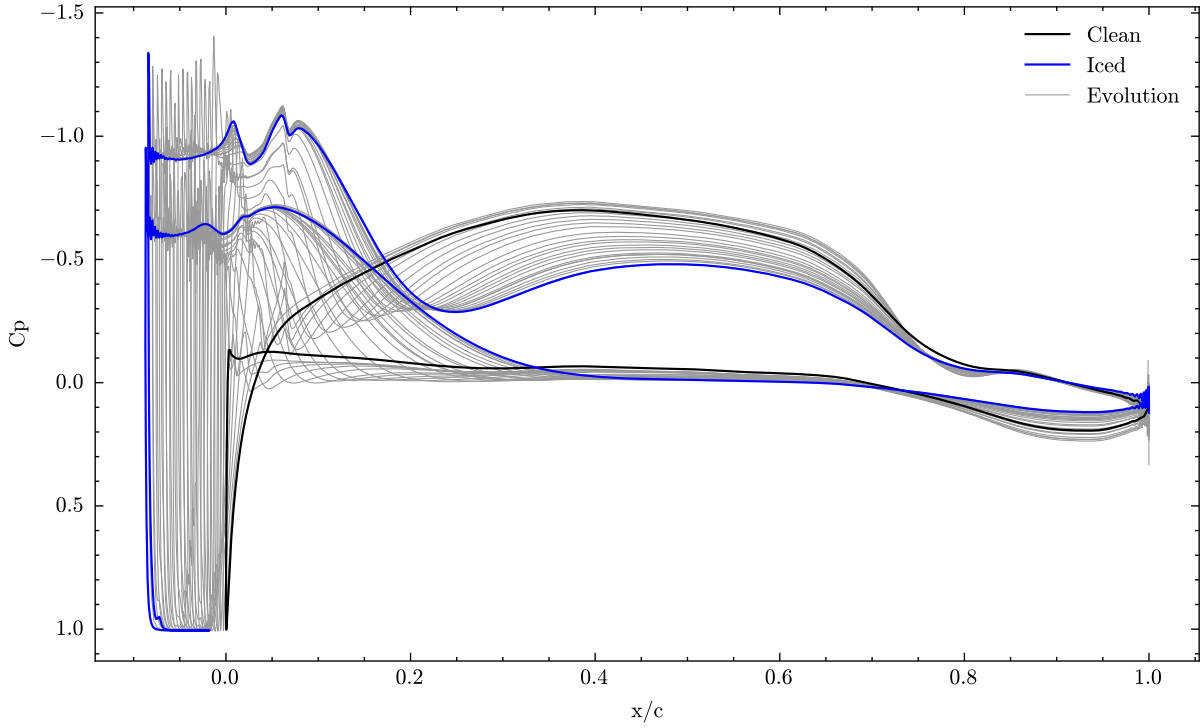

Figure A.8.: Mixed ice — pressure coefficient over dimensionless chord x/c

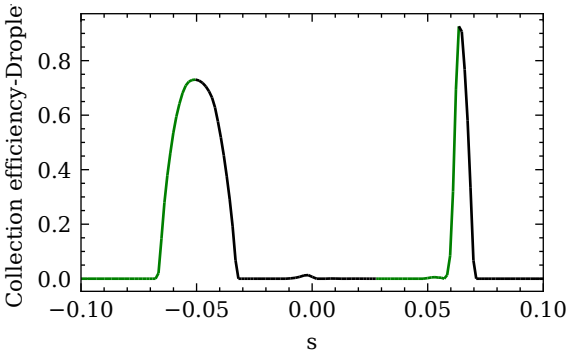

Figure A.9.: Rime ice — collection efficiency β

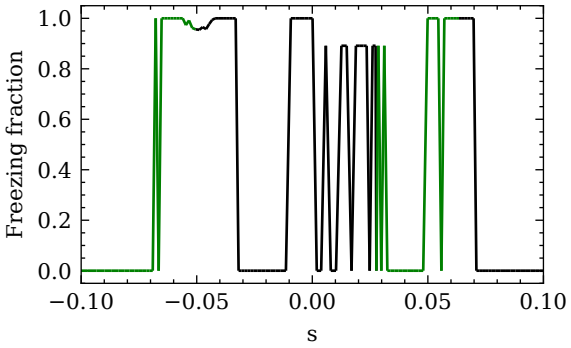

Figure A.10.: Rime ice — freezing fraction η

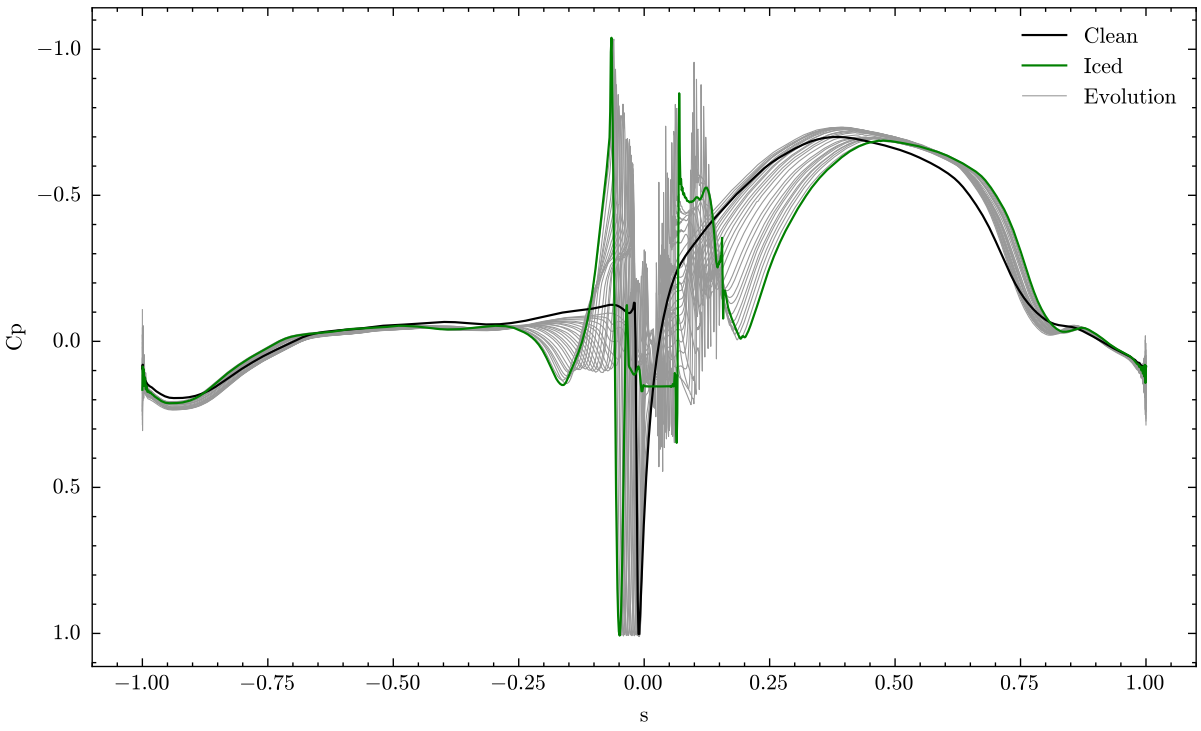

Figure A.11.: Rime ice — pressure coefficient over arc length s

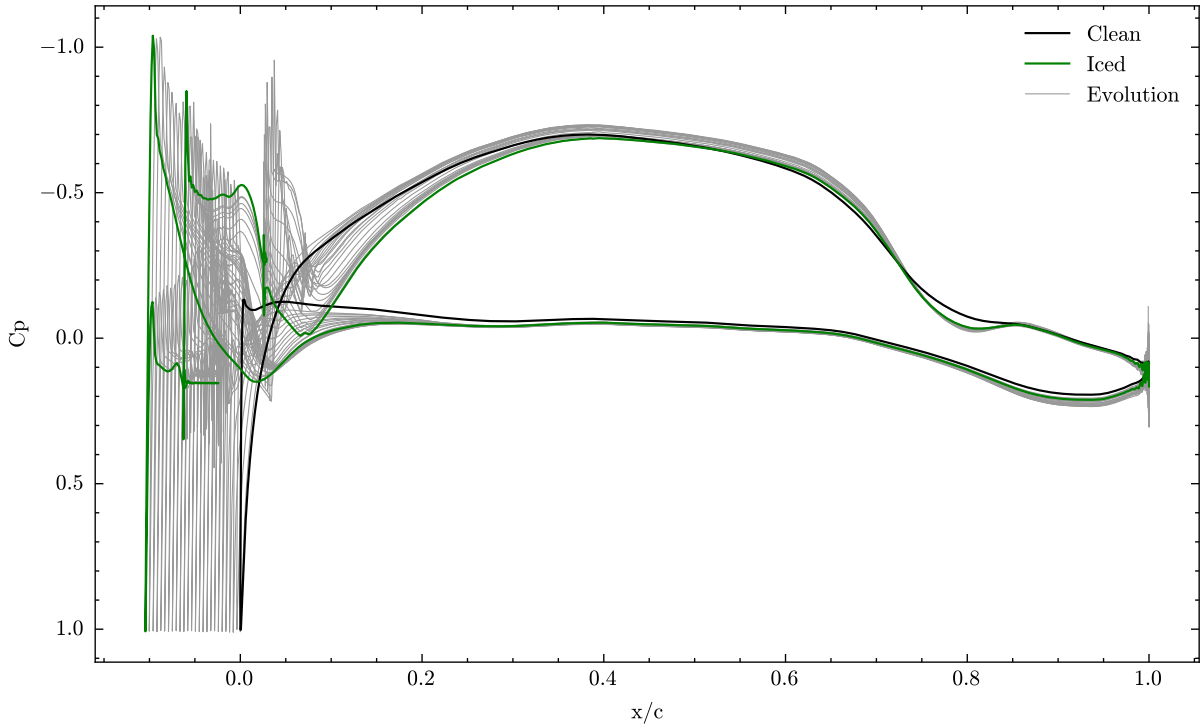

Figure A.12.: Rime ice — pressure coefficient over dimensionless chord x/c

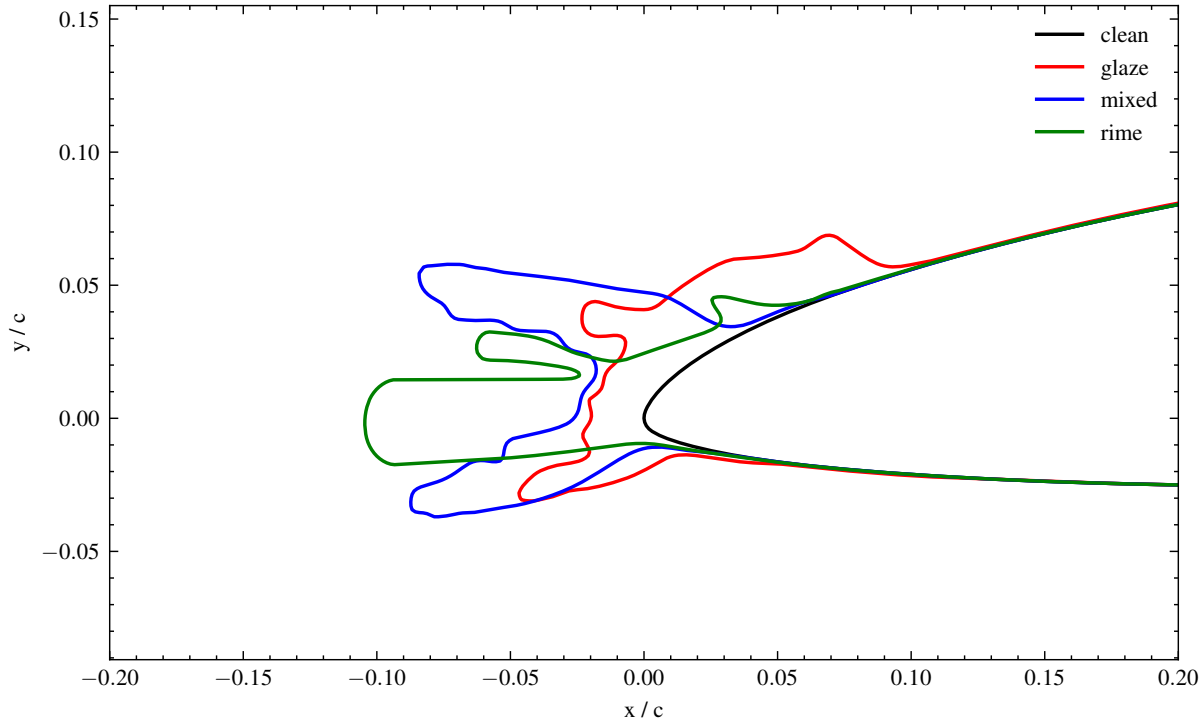

Figure A.13.: Ice shape evolution for SC10+MS25x128.5 for glaze, mixed and rime ice

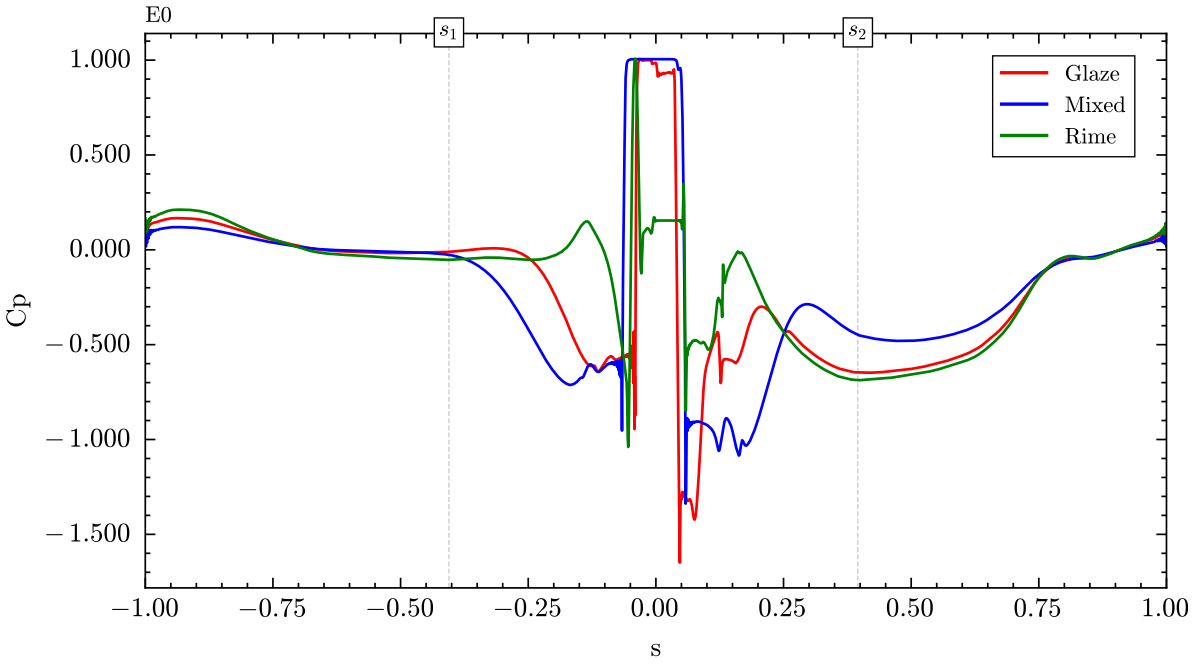

Figure A.14.: Suction coefficient for glaze, mixed, rime over dimensionless arc-length s/S

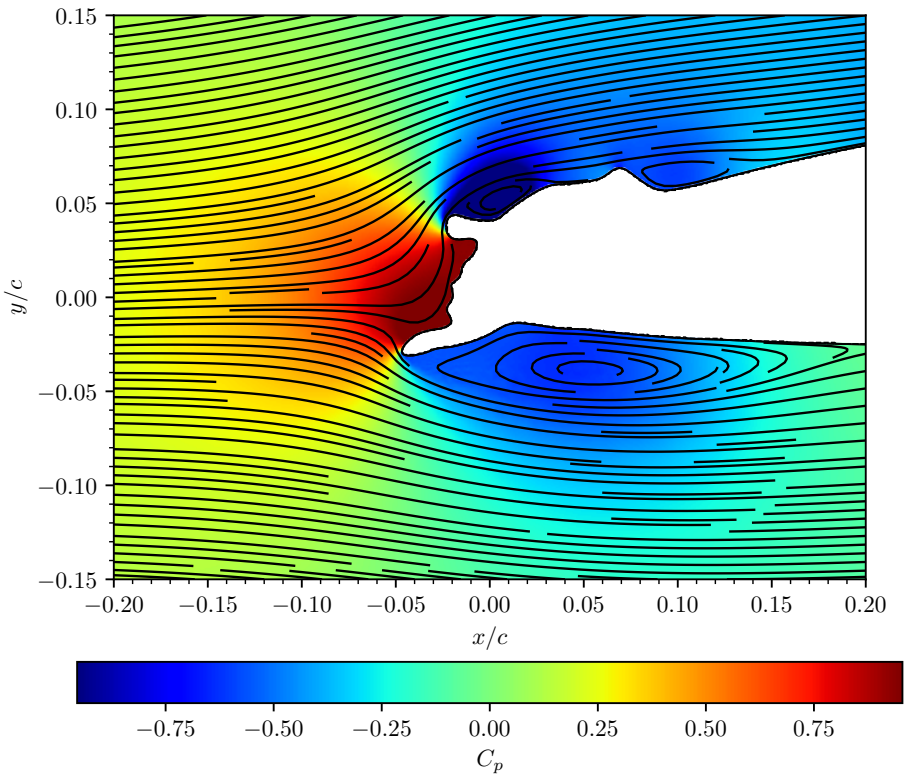

Figure A.15.: Glaze ice — pressure coefficient over dimensionless chord x/c

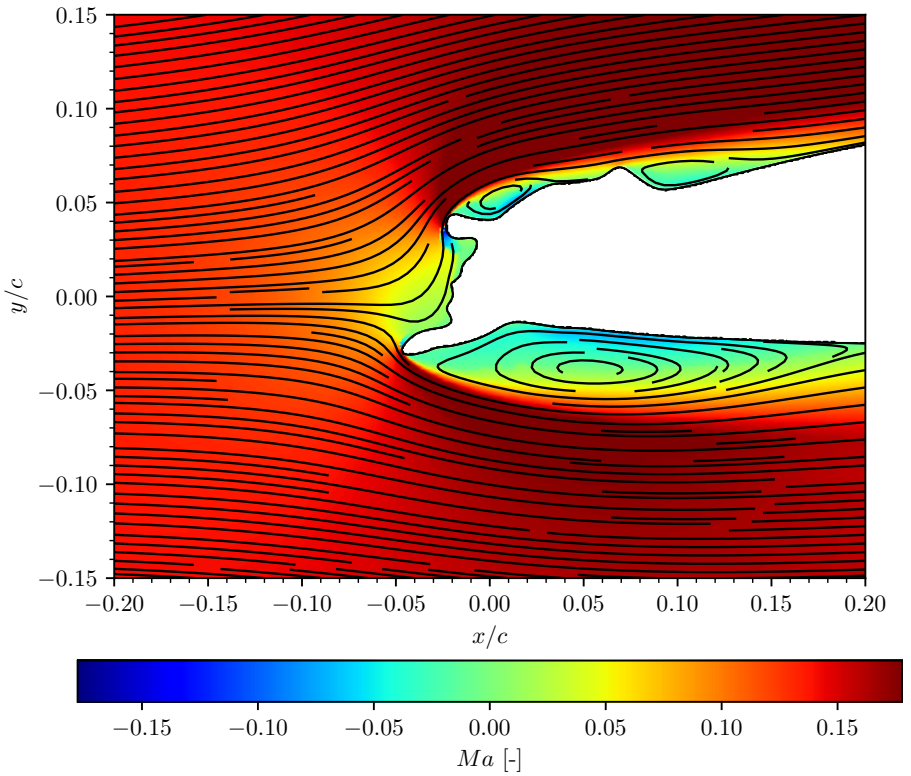

Figure A.16.: Glaze ice — Mach Field

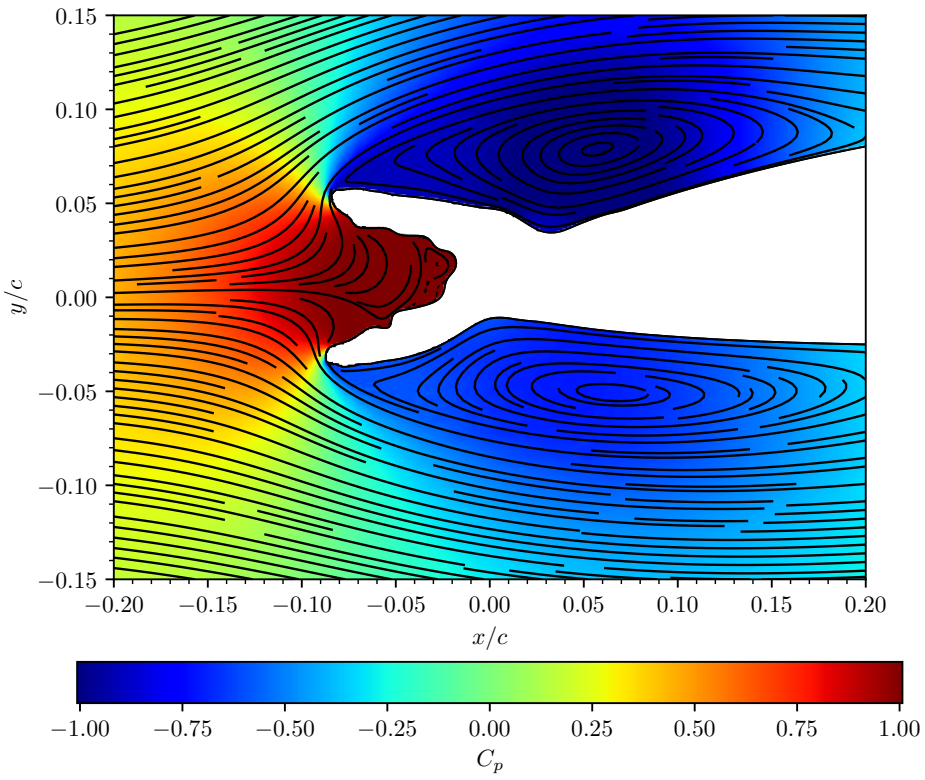

Figure A.17.: Glaze ice — Pressure Field

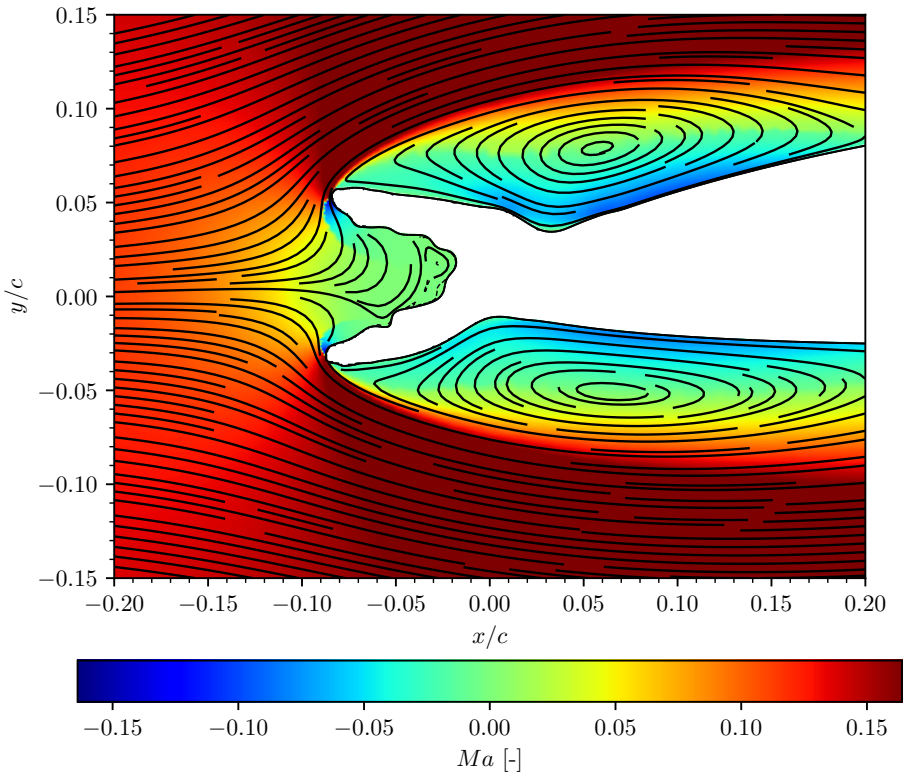

Figure A.18.: Mixed ice — Mach Field

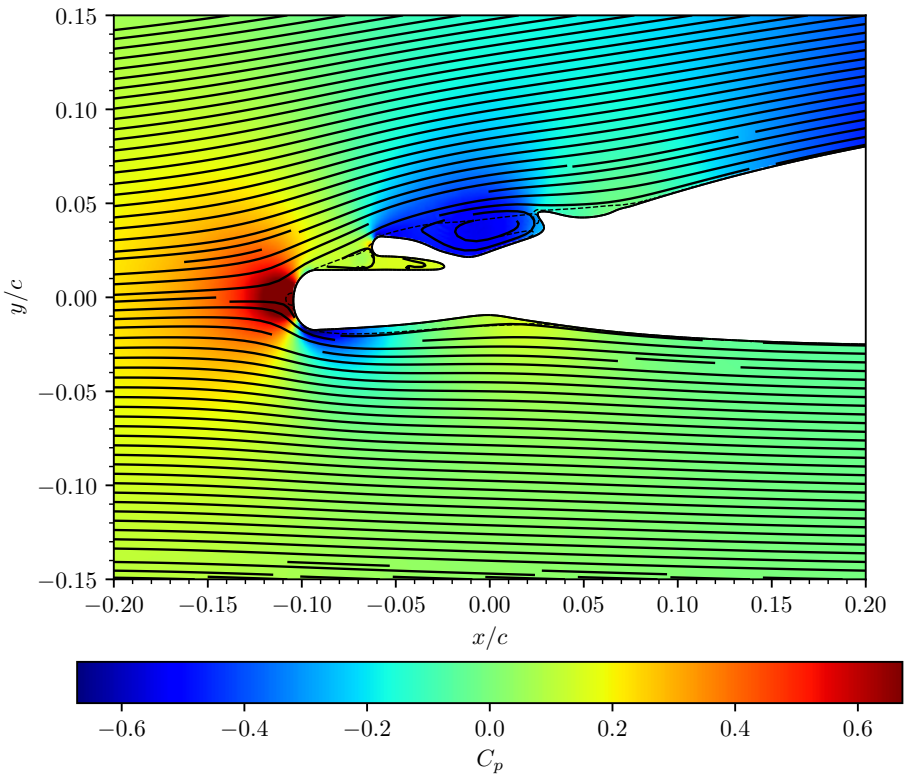

Figure A.19.: Rime ice — Pressure Field

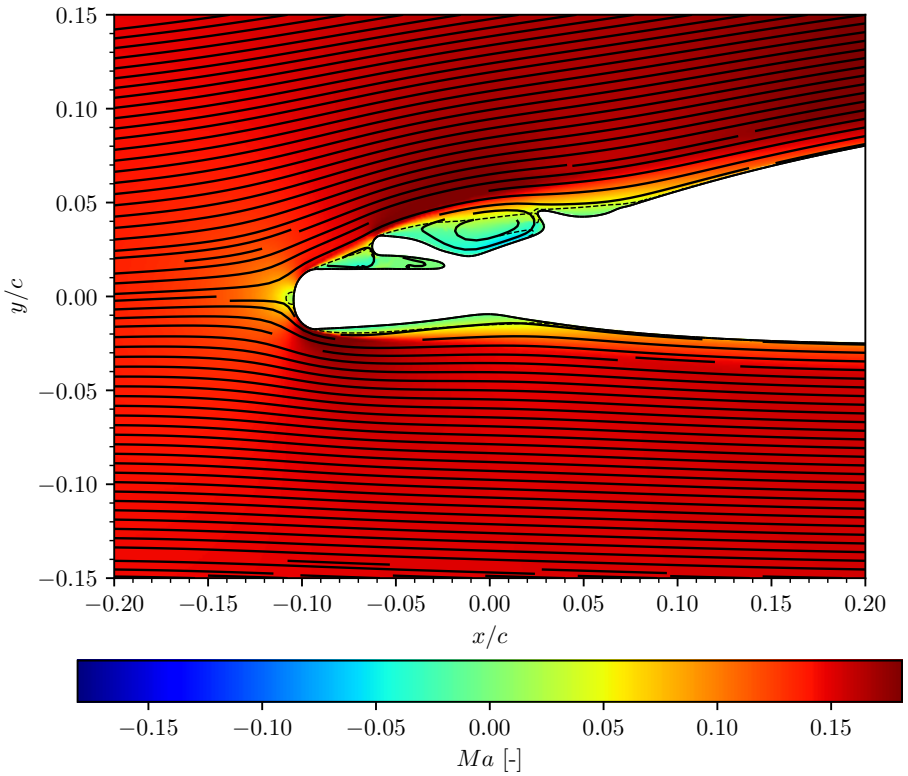

Figure A.20.: Rime ice — Mach field

Table A.1.: Milestones: time to reach selected fractions of normalized ice thickness $\tilde{h}_{\text{ice}}$ per case.

Case	$\tilde{h}_{\text{ice}}$	t at threshold [s]	Λ at threshold	$\bar{h}_{\text{ice}}$ [m]
glaze	0.100	642.500	2.919×10^{2}	0.001
glaze	0.250	1156.500	1.166×10^{2}	0.002
glaze	0.500	2056.000	4.850×10^{1}	0.004
glaze	0.750	2827.000	3.460×10^{1}	0.005
glaze	0.900	3084.000	3.313×10^{1}	0.006
mixed	0.100	771.000	1.536×10^{2}	0.002
mixed	0.250	1413.500	3.354×10^{1}	0.004
mixed	0.500	2184.500	1.109×10^{1}	0.007
mixed	0.750	2698.500	7.094	0.010
mixed	0.900	3212.500	5.096	0.013
rime	0.100	642.500	5.244×10^{2}	0.001
rime	0.250	1413.500	3.203×10^{2}	0.003
rime	0.500	2184.500	1.760×10^{2}	0.006
rime	0.750	2698.500	1.688×10^{2}	0.008
rime	0.900	3212.500	1.582×10^{2}	0.011

Table A.2.: Full aerodynamic polar for **clean**. Angle of attack α in degrees, glide ratio C_L/C_D, and Loyd number $\Lambda = C_L^3/C_D^2$.

α [°]	C_L	C_D	C_M	C_L/C_D	Λ
−4.0	0.027	0.009 76	−0.098	2.8	0.21
−3.5	0.081	0.008 54	−0.099	9.5	7.22
−3.0	0.136	0.007 86	−0.100	17.3	40.63
−2.5	0.192	0.007 46	−0.100	25.7	126.39
−2.0	0.248	0.007 24	−0.101	34.3	291.09
−1.5	0.299	0.004 89	−0.103	61.1	1113.82
−1.0	0.356	0.005 00	−0.104	71.2	1801.76
−0.5	0.413	0.005 16	−0.105	80.1	2650.15
0.0	0.470	0.005 36	−0.105	87.7	3618.81
0.5	0.527	0.005 60	−0.106	94.1	4663.86
1.0	0.584	0.005 89	−0.107	99.1	5728.50
1.5	0.640	0.006 22	−0.107	103.0	6793.86
2.0	0.697	0.006 59	−0.108	105.7	7784.57
2.5	0.752	0.007 01	−0.108	107.4	8673.35
3.0	0.807	0.007 50	−0.108	107.6	9342.77
3.5	0.861	0.008 06	−0.109	106.8	9831.21
4.0	0.914	0.008 71	−0.108	105.0	10 077.18
4.5	0.967	0.009 42	−0.108	102.7	10 190.80
5.0	1.018	0.010 21	−0.108	99.7	10 120.26
5.5	1.069	0.011 05	−0.107	96.7	10 004.80
6.0	1.118	0.011 99	−0.107	93.2	9720.47
6.5	1.116	0.016 06	−0.098	69.5	5384.91
7.0	1.139	0.018 33	−0.095	62.1	4397.91
7.5	1.158	0.021 16	−0.091	54.7	3468.56
8.0	1.187	0.023 19	−0.089	51.2	3110.65
8.5	1.212	0.025 40	−0.086	47.7	2759.56
9.0	1.231	0.027 98	−0.083	44.0	2382.75
9.5	1.245	0.030 83	−0.080	40.4	2030.30
10.0	1.258	0.033 87	−0.077	37.1	1735.45
10.5	1.268	0.037 15	−0.073	34.1	1477.20
11.0	1.272	0.040 67	−0.069	31.3	1244.55
11.5	1.275	0.044 80	−0.066	28.5	1032.70
12.0	1.274	0.049 37	−0.063	25.8	848.36

Table A.3.: Full aerodynamic polar for **glaze**. Angle of attack α in degrees, glide ratio C_L/C_D, and Loyd number $\Lambda = C_L^3/C_D^2$.

α [°]	C_L	C_D	C_M	C_L/C_D	Λ
−4.0	0.021	0.067 45	−0.064	0.3	0.00
−3.5	0.029	0.062 20	−0.073	0.5	0.01
−3.0	0.055	0.056 64	−0.080	1.0	0.05
−2.5	0.092	0.051 52	−0.085	1.8	0.29
−2.0	0.132	0.047 19	−0.087	2.8	1.03
−1.5	0.176	0.043 52	−0.088	4.1	2.90
−1.0	0.223	0.040 54	−0.088	5.5	6.72
−0.5	0.270	0.038 19	−0.087	7.1	13.53
0.0	0.318	0.036 48	−0.086	8.7	24.10
0.5	0.366	0.035 36	−0.084	10.3	39.12
1.0	0.412	0.034 86	−0.082	11.8	57.61
1.5	0.457	0.034 96	−0.079	13.1	77.89
2.0	0.498	0.035 72	−0.077	13.9	96.74
2.5	0.535	0.037 25	−0.073	14.4	110.48
3.0	0.566	0.039 56	−0.070	14.3	115.74
3.5	0.589	0.042 66	−0.065	13.8	112.11
4.0	0.606	0.046 51	−0.061	13.0	102.98
4.5	0.613	0.050 86	−0.057	12.0	88.92
5.0	0.612	0.055 53	−0.053	11.0	74.26

Table A.4.: Full aerodynamic polar for **mixed**. Angle of attack α in degrees, glide ratio C_L/C_D, and Loyd number $\Lambda = C_L^3/C_D^2$.

α [°]	C_L	C_D	C_M	C_L/C_D	Λ
−3.0	0.088	0.081 29	−0.040	1.1	0.10
−2.5	0.090	0.077 40	−0.047	1.2	0.12
−2.0	0.109	0.073 57	−0.052	1.5	0.24
−1.5	0.141	0.070 29	−0.055	2.0	0.57
−1.0	0.178	0.067 83	−0.056	2.6	1.23
−0.5	0.218	0.066 17	−0.056	3.3	2.37
0.5	0.300	0.064 99	−0.054	4.6	6.41
1.0	0.340	0.065 48	−0.052	5.2	9.18
1.5	0.377	0.066 65	−0.049	5.7	12.04
2.0	0.409	0.068 52	−0.047	6.0	14.63
2.5	0.436	0.071 06	−0.044	6.1	16.43
3.0	0.450	0.074 20	−0.041	6.1	16.50
3.5	0.442	0.077 98	−0.038	5.7	14.23

Table A.5.: Full aerodynamic polar for **rime**. Angle of attack α in degrees, glide ratio C_L/C_D, and Loyd number $\Lambda = C_L^3/C_D^2$.

α [°]	C_L	C_D	C_M	C_L/C_D	Λ
−4.0	−0.031	0.034 00	−0.097	−0.9	−0.03
−3.5	0.014	0.030 67	−0.096	0.4	0.00
−3.0	0.060	0.027 90	−0.095	2.2	0.28
−2.5	0.108	0.025 65	−0.094	4.2	1.94
−2.0	0.159	0.023 79	−0.093	6.7	7.13
−1.5	0.212	0.022 29	−0.092	9.5	19.07
−1.0	0.265	0.021 08	−0.091	12.6	41.83
−0.5	0.319	0.020 02	−0.090	15.9	80.61
0.0	0.373	0.018 73	−0.089	19.9	147.69
0.5	0.427	0.017 59	−0.088	24.3	251.23
1.0	0.480	0.017 81	−0.087	27.0	348.65
1.5	0.532	0.018 43	−0.087	28.9	443.26
2.0	0.583	0.019 25	−0.086	30.3	534.47
2.5	0.633	0.020 25	−0.085	31.3	619.70
3.0	0.684	0.021 38	−0.084	32.0	698.86
3.5	0.731	0.022 68	−0.082	32.2	760.64
4.0	0.777	0.024 11	−0.081	32.2	808.03
4.5	0.821	0.025 71	−0.079	31.9	837.19
5.0	0.863	0.027 50	−0.077	31.4	850.19
5.5	0.902	0.029 51	−0.075	30.6	844.31
6.0	0.935	0.031 73	−0.073	29.5	811.71
6.5	0.960	0.034 23	−0.069	28.0	754.15
7.0	0.970	0.037 17	−0.064	26.1	660.86
7.5	0.978	0.040 10	−0.060	24.4	581.81
8.0	0.989	0.043 24	−0.056	22.9	516.85
8.5	1.004	0.046 93	−0.052	21.4	459.58
9.0	1.009	0.050 47	−0.048	20.0	403.21
9.5	1.015	0.054 75	−0.044	18.5	348.84
10.0	1.018	0.059 72	−0.041	17.0	295.80
10.5	1.017	0.065 76	−0.038	15.5	243.24

Bibliography

[1] Antonello Cherubini et al. „Airborne Wind Energy Systems: A Review of the Technologies“. In: *Renewable and Sustainable Energy Reviews* 51 (Nov. 2015), pp. 1461–1476. ISSN: 13640321. DOI: 10.1016/j.rser.2015.07.053. (Visited on 10/23/2025).

[2] Uwe Ahrens, Moritz Diehl, and Roland Schmehl, eds. *Airborne Wind Energy*. Green Energy and Technology. Berlin, Heidelberg: Springer Berlin Heidelberg, 2013. ISBN: 978-3-642-39964-0 978-3-642-39965-7. DOI: 10.1007/978-3-642-39965-7. (Visited on 05/21/2025).

[3] Stephanie Mann. „An Introduction to Airborne Wind: Technology and Cost Reduction Trends“. In: *Offshore Renewable Energy Catapult* (Feb. 2019), pp. 1–10. URL: https://ore.catapult.org.uk/analysisinsight/an-introduction-to-airborne-wind (visited on 11/06/2025).

[4] Norwegian University of Science and Technology, Richard Hann, and Tor Johansen. *Unsettled Topics in Unmanned Aerial Vehicle Icing*. Tech. rep. SAE International, Apr. 2020. DOI: 10.4271/epr2020008. (Visited on 04/14/2025).

[5] Richard K Jeck. „Icing Design Envelopes (14 CFR Parts 25 and 29, Appendix C) Converted to a Distance-Based Format“. In: DOT/FAA/AR-00/30 (2002). URL: https://www.faa.gov/sites/faa.gov/files/aircraft/air_cert/design_approvals/small_airplanes/aceReportAR-00-30.pdf.

[6] International Energy Agency (IEA). „Global Energy Review 2025“. In: (2025).

[7] IEA. *Electricity2025*. 2025.

[8] Gabriel Lopez, Yousef Pourjamal, and Christian Breyer. „Paving the Way towards a Sustainable Future or Lagging behind? An Ex-Post Analysis of the International Energy Agency's World Energy Outlook“. In: *Renewable and Sustainable Energy Reviews* 212 (Apr. 2025), p. 115371. ISSN: 13640321. DOI: 10.1016/j.rser.2025.115371. (Visited on 11/02/2025).

[9] Volker Quaschning. *Understanding Renewable Energy Systems*. Online-Ausg. EBL-Schweitzer. Hoboken: Taylor and Francis, 2014. ISBN: 978-1-84407-136-4 978-1-317-76271-3.

[10] Energy Transitions Comission. *ETC-Offshore-Wind-Insights-Briefing*. 2024.

[11] Tony Burton, ed. *Wind Energy: Handbook*. Repr. Chichester: Wiley, 2009. ISBN: 978-0-471-48997-9.

[12] Miles L Loyd. „Crosswind Kite Power“. In: *Journal of Energy* 4.3 (1980), pp. 106–111. DOI: 10.2514/3.48021. URL: https://arc.aiaa.org/doi/10.2514/3.48021.

[13] Roland Schmehl, ed. *Airborne Wind Energy: Advances in Technology Development and Research*.

[14] Mazen Alhamalawi. „Offshore Wind Power Foundations' Corrosion Protection Strategy“. In: (2021).

[15] Lorenzo Fagiano et al. „Autonomous Airborne Wind Energy Systems: Accomplishments and Challenges“. In: *Annual Review of Control, Robotics, and Autonomous Systems* 5.1 (May 2022), pp. 603–631. ISSN: 2573-5144, 2573-5144. DOI: 10.1146/annurev-control-042820-124658. (Visited on 11/02/2025).

[16] Kitemill. https://www.kitemill.com/news/introducing-the-km2-system. 2025.

[17] Rishikesh Joshi, Dominic Von Terzi, and Roland Schmehl. „System Design and Scaling Trends in Airborne Wind Energy Demonstrated for a Ground-Generation Concept“. In: *Wind Energy Science* 10.4 (Apr. 2025), pp. 695–718. ISSN: 2366-7451. DOI: 10.5194/wes-10-695-2025. (Visited on 11/02/2025).

[18] Luuk Van Hagen et al. „Life-Cycle Assessment of a Multi-Megawatt Airborne Wind Energy System“. In: *Energies* 16.4 (Feb. 2023), p. 1750. ISSN: 1996-1073. DOI: 10.3390/en16041750. (Visited on 04/14/2025).

[19] irena. *IRENA_TEC_RPGC_in_2024_Summary_2025*. 2024.

[20] Richard Hann. „Richard Hann_PhD“. PhD thesis. Trondheim: NTNU, 2020. HDL: 11250/2657638.

[21] Rishikesh Joshi, Dominic Von Terzi, and Roland Schmehl. *System Design and Scaling Trends for Airborne Wind Energy*. Nov. 2024. DOI: 10.5194/wes-2024-161. (Visited on 04/14/2025).

[22] Johannes Oehler and Roland Schmehl. „Aerodynamic Characterization of a Soft Kite by in Situ Flow Measurement“. In: *Wind Energy Science* 4.1 (Jan. 2019), pp. 1–21. ISSN: 2366-7451. DOI: 10.5194/wes-4-1-2019. (Visited on 11/03/2025).

[23] John David Anderson. *Fundamentals of Aerodynamics*. Sixth edition. McGraw-Hill Series in Aeronautical and Aerospace Engineering. New York, NY: McGraw-Hill Education, 2017. ISBN: 978-1-259-12991-9. URL: https://books.google.com/books?id=_7VLjwEACAAJ.

[24] Aldo U. Zgraggen, Lorenzo Fagiano, and Manfred Morari. „On Modeling and Control of the Retraction Phase for Airborne Wind Energy Systems“. In: *53rd IEEE Conference on Decision and Control*. Los Angeles, CA, USA: IEEE, Dec. 2014, pp. 5686–5691. ISBN: 978-1-4673-6090-6 978-1-4799-7746-8 978-1-4799-7745-1. DOI: 10.1109/CDC.2014.7040279. (Visited on 11/03/2025).

[25] Filippo Trevisi, Mac Gaunaa, and Michael Mcwilliam. „The Influence of Tether Sag on Airborne Wind Energy Generation“. In: *Journal of Physics: Conference Series* 1618.3 (Sept. 2020), p. 032006. ISSN: 1742-6588, 1742-6596. DOI: 10.1088/1742-6596/1618/3/032006. (Visited on 11/03/2025).

[26] Milan Milutinović, Nenad Kranjčević, and Joško Deur. „Multi-Mass Dynamic Model of a Variable-Length Tether Used in a High Altitude Wind Energy System“. In: *Energy Conversion and Management* 87 (Nov. 2014), pp. 1141–1150. ISSN: 01968904. DOI: 10.1016/j.enconman.2014.04.013. (Visited on 11/03/2025).

[27] Lorenzo Fagiano et al. „Autonomous Airborne Wind Energy Systems: Accomplishments and Challenges“. In: *Annual Review of Control, Robotics, and Autonomous Systems* 5.1 (May 2022), pp. 603–631. ISSN: 2573-5144, 2573-5144. DOI: 10.1146/annurev-control-042820-124658. (Visited on 04/14/2025).

[28] Davide Todeschini et al. „Control of a Rigid Wing Pumping Airborne Wind Energy System in All Operational Phases“. In: *Control Engineering Practice* 111 (June 2021), p. 104794. ISSN: 09670661. DOI: 10.1016/j.conengprac.2021.104794. (Visited on 11/03/2025).

[29] Jason Jonkman. „Google / Makani Energy Kite Modeling: Cooperative Research and Development Final Report, CRADA Number CRD-17-00569“. In: *Renewable Energy* (2021).

[30] Markus Lindner and Richard Hann. „UAV Icing: Comparison of Simulated 3D and 2D Ice Accretion on Wings“. In: *AIAA AVIATION FORUM AND ASCEND 2024*. Las Vegas, Nevada: American Institute of Aeronautics and Astronautics, July 2024. ISBN: 978-1-62410-716-0. DOI: 10.2514/6.2024-4451. (Visited on 04/14/2025).

[31] M.B. Bragg, A.P. Broeren, and L.A. Blumenthal. „Iced-Airfoil Aerodynamics“. In: *Progress in Aerospace Sciences* 41.5 (July 2005), pp. 323–362. ISSN: 03760421. DOI: 10.1016/j.paerosci.2005.07.001. (Visited on 11/03/2025).

[32] Nicolas Fajt. „The Influence of Meteorological Conditions on the Icing Performance Penalties on a UAV Airfoil“. MA thesis. 2019.

[33] Michael Henzler. „CFD- Simulation of Icing on a Flying- Wing UAV“. MA thesis. Trondheim: University of Stuttgart, Apr. 2024.

[34] *Ansys_FENSAP-ICE_User_Manual*. 2023.

[35] David C. Wilcox. *Turbulence Modeling for CFD*. 3rd ed. La Canada, California: DCW Industries, 2006.

[36] Philippe R. Spalart and Steven R. Allmaras. „A One-Equation Turbulence Model for Aerodynamic Flows“. In: *30th AIAA Aerospace Sciences Meeting and Exhibit*. AIAA Paper 92-0439. Reno, Nevada: AIAA, 1992.

[37] B. E. Launder and D. B. Spalding. „The Numerical Computation of Turbulent Flows“. In: *Computer Methods in Applied Mechanics and Engineering* 3.2 (1974), pp. 269–289. DOI: 10.1016/0045-7825(74)90029-2.

[38] David C. Wilcox. „Reassessment of the Scale-Determining Equation for Advanced Turbulence Models“. In: *AIAA Journal* 26.11 (1988), pp. 1299–1310. DOI: 10.2514/3.10041.

[39] Florian R. Menter. „Two-Equation Eddy-Viscosity Turbulence Models for Engineering Applications“. In: *AIAA Journal* 32.8 (1994), pp. 1598–1605. DOI: 10.2514/3.12149.

[40] Florian R. Menter, Martin Kuntz, and Robin Langtry. „Ten Years of Industrial Experience with the SST Turbulence Model“. In: *Turbulence, Heat and Mass Transfer 4*. Begell House, 2003, pp. 625–632.

[41] Hermann Schlichting and Klaus Gersten. *Boundary-Layer Theory*. 9th ed. Berlin: Springer, 2017.

[42] Frank M. White. *Viscous Fluid Flow*. 3rd ed. New York: McGraw-Hill, 2011.

[43] Bernard L. Messinger. „Equilibrium Temperature of an Unheated Icing Surface as a Function of Air Speed“. In: *Journal of the Aeronautical Sciences* 20.1 (Jan. 1953), pp. 29–42. ISSN: 1936-9956. DOI: 10.2514/8.2520. (Visited on 11/05/2025).

[44] M. Drela and H. Youngren. *XFOIL 6.9 User Primer*. http://web.mit.edu/aeroutil_v1.0/xfoil_doc.txt. MIT Dept. of Aeronautics & Astronautics. 2001.

[45] François Morency et al. „FENSAP-ICE – A comprehensive 3D simulation system for in-flight icing“. In: *15th AIAA Computational Fluid Dynamics Conference*. AIAA Paper 2001-2566. Anaheim, California: AIAA, June 2001. DOI: 10.2514/6.2001-2566.

[46] Patrick J. Roache. *Verification and Validation in Computational Science and Engineering*. Albuquerque, NM: Hermosa Publishers, 1998. ISBN: 9780913478080.

[47] Ismail B. Celik et al. „Procedure for Estimation and Reporting of Uncertainty Due to Discretization in CFD Applications“. In: *Journal of Fluids Engineering* 130.7 (2008), pp. 078001–1–078001–4. ISSN: 0098-2202. DOI: 10.1115/1.2960953.